TECH LIBRARY KAFB, NM
0060983

NASA CONTRACTOR REPORT

NASA CR-19

NASA CR-1913

LOAN COPY: RETURN TO
AFWL (DOUL)
KIRTLAND AFB, N. M.

ANALYSIS OF FLIGHT DATA ON BOUNDARY LAYER TRANSITION AT HIGH ANGLES-OF-ATTACK

RECEIVED
3 MAY 1972
Technical Library
AF Weapons Laboratory

by Wayne W. Haigh, Bruce M. Lake, and Denny R. S. Ko

Prepared by
TRW SYSTEMS GROUP
Redondo Beach, Calif.
for Langley Research Center

NATIONAL AERONAUTICS AND SPACE ADMINISTRATION • WASHINGTON, D. C. • APRIL 1972

TECH LIBRARY KAFB, NM

0060983

1. Report No.	2. Government Accession No.	3. Recipient's Catalog No.
NASA CR-1913		

4. Title and Subtitle	5. Report Date
ANALYSIS OF FLIGHT DATA ON BOUNDARY LAYER TRANSITION AT HIGH ANGLES OF ATTACK	April 1972
	6. Performing Organization Code
7. Author(s)	8. Performing Organization Report No.
Wayne W. Haigh, Bruce M. Lake, and Denny R. S. Ko	17,181 - 6002-R0-00
	10. Work Unit No.
9. Performing Organization Name and Address	
TRW, Inc. TRW Systems Group Redondo Beach, CA 90278	11. Contract or Grant No. NAS1-10078
	13. Type of Report and Period Covered Contractor Report
12. Sponsoring Agency Name and Address	
National Aeronautics and Space Administration Washington, DC 20546	14. Sponsoring Agency Code

15. Supplementary Notes

16. Abstract

Boundary layer transition data were obtained on the flight of two cones which reentered at velocities of about 7.0 km/sec. One cone reentered at a nominal zero degree angle of attack and the other, due to an anomaly above the earth atmosphere, reentered at local angles of attack up to 7.0 km/sec. The transition data were obtained from on-board acoustic and electrostatic sensors. A description of the design, calibration, and method used to detect transition from the sensors is included. The flow field calculation used to obtain the local flow properties on the cones is described. Finally, the transition data found from both cone flights is correlated.

17. Key Words (Suggested by Author(s))	18. Distribution Statement
Boundary layer transition data Cone flight reentry Boundary layer transition correlations Acoustic and electrostatic sensors	Unclassified - Unlimited

19. Security Classif. (of this report)	20. Security Classif. (of this page)	21. No. of Pages	22. Price*
Unclassified	Unclassified	164	$3.00

*For sale by the National Technical Information Service, Springfield, Virginia 22151

CONTENTS

		Page
I.	INTRODUCTION	1
II.	REENTRY VEHICLES AND FLIGHT CONDITIONS	3
	2.1 Reentry Vehicles	3
	2.2 Vehicle Flight Conditions	3
III.	DESCRIPTION OF SENSORS	5
	3.1 Acoustic Sensors	5
	3.1.1 Acoustic Sensor Design	5
	3.1.2 Acoustic Sensor Electronics	6
	3.1.3 Acoustic Sensor Testing and Calibration Procedures	7
	3.1.4 Acoustic Sensor Characteristics	8
	3.1.5 Acoustic Sensor Locations	8
	3.2 Base Pressure Gauge	9
	3.2.1 Pressure Gauge Design	9
	3.2.2 Pressure Gauge Electronics	9
	3.2.3 Pressure Gauge Location	9
	3.3 Electrostatic Probes	10
	3.3.1 Electrostatic Probe Design	10
	3.3.1.1 Basic Measurement	10
	3.3.1.2 Transition Detection	11
	3.3.1.3 Probe Design	11
	3.3.2 Electrostatic Probe Electronics	12
	3.3.3 Electrostatic Probe Calibration Procedures	13
	3.3.4 Electrostatic Probe Locations	13
	3.4 Vehicle Thermocouples	14
	3.4.1 Thermocouple Installation	14
	3.4.2 Thermocouple Locations	14
IV.	FLIGHT TEST DATA	15
	4.1 Vehicle Dynamics Analysis	15
	4.1.1 Total Angle-of-Attack	15
	4.1.2 Angle Between the Sensor and the Windward Meridian	16
	4.1.3 Local Angle-of-Attack	17
	4.1.4 Reduced Vehicle Dynamics Data	18
	4.2 Zero Angle-of-Attack Boundary Layer Transition Data	18

Page

4.2.1 Zero Angle-of-Attack Acoustic Sensor Data 18
4.2.2 Zero Angle-of-Attack Base Pressure Data . . . 20
4.2.3 Zero Angle-of-Attack Electrostatic Probe Data. 21
4.2.4 Zero Angle-of-Attack Thermocouple Data. . . . 23
4.2.5 Comparison of Zero Angle-of-Attack Transition Data 24
4.2.6 Correlation of Flight 2 Acoustic Sensor Data. 25
4.2.7 Correlation of Flight 2 Electrostatic Probe Data. 27

4.3 High Angle-of-Attack Boundary Layer Transition Data 29

4.3.1 High Angle-of-Attack Acoustic Sensor Data . . 29
4.3.2 High Angle-of-Attack Base Pressure Data . . . 33
4.3.3 High Angle-of-Attack Electrostatic Probe Data. 34

4.3.3.1 Measurements on Windward Ray 35
4.3.3.2 Measurements Off Windward Ray. . . . 36

4.3.4 High Angle-of-Attack Thermocouple Data. . . . 37

V. FLOW FIELD ANALYSIS

5.1 General Approach 40

5.2 Analysis 40

5.2.1 Governing Equations 40

5.2.1.1 Inviscid Field 41
5.2.1.2 Boundary Layer 43

5.2.2 Inviscid Pressure Field 46
5.2.3 Method of Solution. 47
5.2.4 Initial Conditions. 50

5.3 Results and Discussions. 51

5.3.1 General Flow Field Results. 51
5.3.2 Flow Field Results for Flight 1 Transition Analysis 53

VI. CORRELATION OF BOUNDARY LAYER TRANSITION DATA 55

6.1 Correlation of Zero Angle-of-Attack Data 55

6.2 Correlation of Acoustic Sensor Data. 57

6.3 Electrostatic Probe Transition Results 59

6.4 Correlation of Acoustic Sensor and Electrostatic Probe Data 62

Page

VII. CONCLUSIONS AND RECOMMENDATIONS 64

REFERENCES 67

APPENDIX 137

Page

VII. CONCLUSIONS AND RECOMMENDATIONS 64

REFERENCES 67

APPENDIX 137

ANALYSIS OF FLIGHT DATA ON BOUNDARY LAYER TRANSITION AT HIGH ANGLES-OF-ATTACK

By Wayne W. Haigh, Bruce M. Lake and Denny R. S. Ko
TRW Systems Group

I. INTRODUCTION

The effect of vehicle angle-of-attack on boundary layer transition has received considerable attention in recent years. Particular interest is now focused on the space shuttle program in which angles-of-attack as high as 60 degrees are envisioned for the vehicle reentry attitude. Aerodynamic heating considerations, which are directly affected by the altitude at which the boundary layer becomes turbulent, are of major importance in the design of these shuttle vehicles. As a result, boundary layer transition criteria which must be developed for this application will play an important role in determining the requirements and the type of heatshield materials (either heat sink or ablative).

In spite of the effort expended to date on this phenomenon, the laminar boundary layer transition process has defied the development of a successful theoretical analysis. Consequently, the bulk of the knowledge accumulated on boundary layer transition has relied almost entirely on experimental data. Unfortunately, the majority of these data are not directly applicable to the design of space shuttle vehicles because of inadequate simulation of vehicle attitude and flight conditions.

Boundary layer transition data which are applicable to this problem were recently obtained from onboard instruments during the flights of two similar reentry vehicles. One vehicle entered the atmosphere at a small angle-of-attack, while the other entered at high angle-of-attack. The analysis of acoustic sensor, electrostatic probe, and base pressure data from these two flights forms the primary basis for the present study. The first phase of this study, performed in the period from June 1970 to November 1970, was based on the analysis of acoustic sensor and base pressure data. The study program was then extended to include the analysis of electrostatic probe data and the presentation of thermocouple data. This second phase of the study was performed during the period from November 1970 to

February 1971.

Several aspects of the flight test program from which these data were obtained are classified. Consequently, a number of the references and some other information which is necessary for the documentation of this study are contained in Reference 3, a classified addendum to this report.

II. REENTRY VEHICLES AND FLIGHT CONDITIONS

The boundary layer transition data which formed the basis for this study were obtained from onboard instruments during the flights of two similar reentry vehicles.

2.1 REENTRY VEHICLES

The reentry vehicles were both slender conical nonablating vehicles which had 0.1-inch radius graphite nose tips and 4-inch radius base shoulders. Special precautions were taken prior to each flight to ensure a clean and smooth vehicle surface. Flight 1 entered the atmosphere at a high angle-of-attack, while Flight 2 entered at a low angle-of-attack flight. A detailed description of these reentry vehicles, the launch system, and the performance of the vehicles is contained in References 1 and 2 for Flights 1 and 2, respectively.

Preflight predictions of nose shape change during reentry indicated that the vehicle nose radius would blunt from 0.1-inch to about 0.2-inch at an altitude of 30.5 km (100 kft). Additional information on both these predictions and the effects of nose bluntness on boundary layer transition are included in Reference 2.

2.2 VEHICLE FLIGHT CONDITIONS

The major part of this study was based on an analysis of the test data from Flight 1, while the data from Flight 2 were analyzed to provide a baseline for interpretation of the high angle-of-attack transition data. In addition to the boundary layer transition data from these nonablating heatshield vehicles, boundary layer transition altitudes are presented for Flight 3, a low angle-of-attack flight with an ablating heatshield.

The trajectories of the two nonablating reentry vehicles were very similar as shown by their velocity/altitude characteristics in Figure 1 of the addendum. Flight 1 vehicle velocity and altitude as a function of time after liftoff (TALO) are presented in Figure 2 of this addendum.

Flight 1 entered the atmosphere at a large angle-of-attack. The aerodynamic forces reduced the vehicle total angle-of-attack from 36 degrees at 61 km (200 kft) to about 9 degrees at 30.5 km (100 kft). The vehicle total angle-of-attack was as large as 67 degrees at an altitude of about 80 km (TALO of 1627.4 seconds) as shown in Figure 1. A polar angle-of-attack history (pitch angle-of-attack versus yaw angle-of-attack) is given in Figures 2a and 2b. This vehicle had a near constant roll rate of about 15 rpm during reentry as shown by the roll angle history in Figure 3. The vehicle attitude angles are defined in Figure 4.

Flight 2, the other flight with a nonablating vehicle, entered the atmosphere at an angle-of-attack of less than 1 degree. As a result, the boundary layer transition data from this flight were analyzed assuming that the vehicle was at zero angle-of-attack.

III. DESCRIPTION OF SENSORS

The boundary layer transition data which forms the primary basis for this study were obtained from acoustic sensors and electrostatic probes flush-mounted on the vehicle conical surface and pressure sensors mounted on the vehicle base. A description of the acoustic sensors, including the sensor locations and information on the calibration procedures, are presented below in Section 3.1 while equivalent descriptions of the base pressure sensors, electrostatic probes and thermocouple installations are presented in Sections 3.2, 3.3 and 3.4, respectively.

3.1 ACOUSTIC SENSORS

3.1.1 Acoustic Sensor Design

The purpose of the acoustic sensors was to provide a direct and accurate measurement of the boundary layer transition altitude and to monitor the sound pressure level during boundary layer transition to turbulence. In general, the use of an acoustic sensor for detecting transition has certain advantages over other well known methods. The sound pressure level in the boundary layer shows directly whether the boundary layer is laminar or turbulent. Also the measurement is local, i.e., the signal originates from a small region in the neighborhood of the sensing element. Furthermore, the instrument response is rapid, essentially the same as the frequency response of the transducer (typically, up to 200 kHz).

The sensor system was designed to minimize the signal losses and phase lags between the sensor and the boundary layer wall pressure fluctuations, while protecting the sensor itself from excessive heating and contamination. A heatshield coupled sensor system with the transducer located below a vibrating element comprised of heatshield material was found to provide the best acoustic sensor design. Additional background information on acoustic sensors and the rationale for selecting a heatshield coupled system instead of a heatshield cavity sensor is contained in Reference 4.

The design constaints required the sensors to be capable of monitoring a root-mean-square pressure fluctuation (more commonly termed sound pressure level - SPL) of at least 120 db referenced to 0.0002 dynes/cm^2, in a

frequency spectrum between 10 and 200 kHz.

For Flights 1 and 2 the entire acoustic transmission line was made of beryllium because its acoustic impedance was almost equal to that of the lead-zirconate-titanate piezoelectric transducer. The acoustic line was supported by a series of springs and was provided with a series of plate radiators, as shown in Figure 5, to dissipate the heat generated at the sensing tip by aerodynamic heating.

The tip of the sensing element was made of Teflon for the Flight 3 acoustic sensors. It was coupled to a magnesium impedance-matching line whose acoustic impedance was between that of Teflon and the piezoelectric transducer. The transmission line was horn-shaped to further improve the acoustic match. The piezoelectric element was back-loaded with a stainless steel plate whose mass was such that it did not resonate in the 10 to 200 kHz frequency band.

A surrounding plug housed the tip of the acoustic line on the vehicle and was therefore made of the same material as the vehicle heatshield. Isolation of the acoustic line from local heatshield vibrations was accomplished by allowing a radial clearance between the plug and the line. This allowed the exposed tip of the acoustic line to be the pickup area of the sensor. For all practical purposes, the transducer was sensitive only to frequencies in the 10 kHz to 200 kHz band and only to those signals that originated in a small region of the boundary layer in the neighborhood of the sensing tip.

The transducer assembly was a sealed, self-contained package, as shown in Figure 6, that was completely checked out and calibrated in the laboratory.

3.1.2 Acoustic Sensor Electronics

The acoustic sensor system converts the detected acoustic energy into an equivalent electrical energy which was then transmitted to the ground via a data link. The sensor was connected through a coaxial cable to a remote amplifier. The functions of the amplifier were to amplify, rectify, and average the signal. The amount of signal amplification was determined by the estimated magnitude of the sound pressure level to be measured. The frequency response characteristics of the amplifier were tailored to the sensor response characteristics.

Each sensor-amplifier channel contained a rectifier and filter to produce an averaged signal proportional to the sound pressure level detected in the 190 kHz bandwidth of the system. The output of the amplifier and filter system was zero for no signal, and the nominal full-scale signal value was +5 volts dc. The system calibration of a channel gave, as a function of frequency, this dc output voltage for a specified input sound pressure level at the surface of the vehicle. By use of the calibration as a function of frequency, the integrated system calibration could be determined for a random input having either an assumed flat spectrum or any other known spectrum.

3.1.3 Acoustic Sensor Testing and Calibration Procedures

Each sensor was subjected to a rigorous schedule of calibration and environmental tests. The calibration tests were performed first according to a schedule specified in Reference 5. A sequence of environmental tests (see References 6 and 7 for details) were then performed and were followed by a complete recheck of transducer calibration. Random vibration tests conducted on the acoustic sensors are described in Reference 8.

Sensor preflight calibration was carried out in three separate stages:

- Sensitivity of the sensor to acoustic stimulation was determined.
- Voltage gain at the amplifier was determined as a function of frequency over the frequency range of 10 kHz to 200 kHz.
- Calibrations were combined to provide an overall system calibration.

The transducers were calibrated in a small anechoic chamber equipped with loudspeakers that could generate sound pressure levels in excess of 120 db in the frequency band of 10 to 200 kHz. The standard of comparison was a calibrated BK-4135 capacitor microphone. The microphone housing was mechanically interchangeable with the flight transducer assembly, fitting into a plate made of the same material as the heatshield.

The output of the calibrated reference microphone was measured both before and after the transducer calibration measurement; before and after microphone readings had to agree to within 1.5 db for the calibration to be considered valid. The frequency response of the transducer was measured in the 10 kHz to 200 kHz band at a constant voltage input to the acoustic

driver corresponding to a sound pressure level of 120 db. The data was broken down into 19 bands of 10 kHz bandwidth, and the average sound pressure response in each band was determined by graphically integrating the data in the band. The resulting nineteen calibration points were then corrected for the response of the acoustic chamber and the calibration microphone to obtain the corrected transducer calibration.

The calibration of the acoustic sensor system was obtained by combining the corrected transducer calibration with the frequency response of the amplifier associated with the transducer. The overall full-scale transducer calibration was then obtained by combining the nineteen segments of data to determine the overall sound pressure level produced by a signal in the 10 to 200 kHz range.

A final response check was made on each acoustic sensor following installation in the flight vehicle. The check was based on recording the response of the transducers to stimulation by a piezoelectric driver disk bonded to the front face of the sensor. Although essentially qualitative in nature, this check indicated that all sensors on Flights 1, 2, and 3 were functioning properly following installation in the vehicles.

3.1.4 Acoustic Sensor Characteristics

Nominal specifications for the acoustic sensors on Flights 1 and 2 are presented in Table I. The maximum output levels or saturation levels vary between 145 and 160 db depending on the amplifier gain setting. Full-scale outputs for each sensor are given in Table II.

3.1.5 Acoustic Sensor Locations

The locations of the three acoustic sensors on Flight 2 were identical to those on Flight 1. Two of the three sensors were mounted on the conical surface of the reentry vehicle at station 166 which is near the base of the vehicle, while the third was mounted near the midpoint at station 88. One of the base sensors and the midcone sensor was mounted approximately along a single ray while the two base sensors were diametrically opposed. Exact sensor locations are given in Table II; the locations of the sensors are also shown in Figure 7.

3.2 BASE PRESSURE GAUGE

3.2.1 Pressure Gauge Design

The purpose of the pressure gauge was to measure the ambient pressure in the recirculation region of the reentry vehicle for a range of altitude during reentry from 65.5 km (215 kft) to 30.5 km (100 kft). The pressure gauge incorporated a dual range capability (0.01 psia and 0.05 psia full scale) through the use of two amplifiers. The pressure capsule consisted of a thin, stressed titanium diaphragm welded between two titanium alloy rings. On either side of the diaphragm was a quartz disk prepared with a concave surface. The concave surfaces were coated with a thin, evaporated coating of aluminum. Each aluminum surface formed a capacitor with the titanium diaphragm. When a pressure difference existed across the membrane, it bowed in the direction of the pressure gradient, increasing one capacitance and decreasing the other.

Integration of the gauge in the instrumentation package was accomplished without attachment of the unit to the aft cover. A short 1-inch length of stainless steel bellows with an inside diameter of 0.085 inch was used as the pressure inlet line. The bellows assembly was spring loaded against the vehicle aft cover in order to maintain the sensing aperture flush with the outside surface. To eliminate g-loading effects on the thin diaphragm of the gauge, the transducer was mounted so that the plane of the diaphragm was parallel to the longitudinal axis of the reentry vehicle.

3.2.2 Pressure Gauge Electronics

A transducer bridge was used to convert the capacitance difference (C_1-C_2) into an analog dc voltage proportional to the pressure. One amplifier provided a 5-vdc output at 0.01 psia and the other established a 5-vdc output for the 0.05 psia range. A block diagram of the pressure gauge is shown in Figure 8.

3.2.3 Pressure Gauge Location

The high altitude base pressure gauges were located at a radial position about 0.54 of a base radius from the vehicle centerlines. The exact locations of the pressure gauges on the vehicle bases for Flights 1 and 2 are presented in Table III.

3.3 ELECTROSTATIC PROBES

3.3.1 Electrostatic Probe Design

3.3.1.1 Basic Measurement

The electrostatic probes were designed primarily to obtain estimates of boundary layer charged particle number densities. Each electrostatic probe consisted of a ramp biased collector electrode and a return electrode grounded to the vehicle structure. The probe current-voltage characteristics (the variations of collected currents with changes in probe collector bias potential) provide a measure of the surface gradients of the boundary layer charged species concentrations. These measured probe characteristics, combined with an analysis of the boundary layer flow over a probe surface, can therefore be used to estimate the charged particle number densities and fluxes in a hypersonic boundary layer. A typical current-voltage characteristic, such as that shown in Figure 9, shows little variation of the collected current with increased probe bias potential at large bias potentials. The current levels measured when this occurs are referred to as saturation currents. The positive probe saturation currents are directly related to the surface gradients of the boundary layer charged species concentrations, as shown below:

$$j_{+sat} = \frac{2e\ \rho_\delta\ V_\delta\ z}{\left(\frac{2}{3}\ Re\right)^{1/2}\ m_+\ Sc}\ C_{+p}\left(\frac{\partial C_+^*}{\partial n}\right)_m$$

where

C_+ = positive ion mass fraction
D = diffusion coefficient
e = electron charge
j = current density
m = mass of atomic or ionic species
Re = Reynolds number = $\rho\ VX/\mu$
Sc = Schmidt number = $\mu/\rho D$
V = velocity component parallel to cone surface
X = axial distance to probe station
z = Chapman-Rubesin parameter (= $\rho\mu/\rho_\delta\mu_\delta$)

η = boundary layer normal distance parameter $= 1.225 \frac{(Re)^{1/2}}{X} \int_0^y \frac{\rho}{\rho_\delta} dy$

μ = viscosity

ρ = density

Superscripts

* = normalized with respect to maximum value

Subscripts

m = at the probe sheath outer edge

p = at the location of peak ion mass fraction

sat = at saturation conditions

δ = at the boundary layer outer edge

Details concerning this application of the electrostatic probes flown on these vehicles can be found in References 9 through 12.

In addition to providing a means of specification of boundary layer plasma charged particle number densities, it has been found that the probe data (individual current-voltage characteristics as well as saturation current density histories) can be used to investigate a variety of important phenomena, including boundary layer transition.

3.3.1.2 Transition Detection

The collected probe current is dependent upon ambipolar boundary layer properties, particularly gas densities, charged particle profile shapes, peak charged particle densities, and transport properties. With the onset of boundary layer transition these properties can be expected to fluctuate. Similar fluctuations can therefore be expected in the saturation currents collected by the probes (as can be seen from the above equation relating saturation currents to boundary layer properties). Fluctuations are evident in low altitude probe current-voltage characteristics (see Figure 10). Correlation of the onset of such fluctuations in the electrostatic probe data with transition indications from other onboard sensors shows that the electrostatic probes are indeed responding to boundary layer transition (see Section 4.2.7).

3.3.1.3 Probe Design

Figure 11 shows electrostatic probes of the type which were flush-mounted with the heatshields of Flight vehicles 1 and 2. Each probe was mounted

with its return electrode downstream of the collector electrode. The electrodes were made of tungsten with platinum plated outer surfaces. The purpose of the plating was to prevent oxidation of the tungsten surface and to reduce the electron emission from the probe by increasing the surface work function. Beryllium oxide was used as the probe insulator material because, although quite brittle, it maintains high electrical resistivity at high temperatures. To minimize thermal stresses and facilitate machining of the material, each probe insulator was actually a matrix of individual beryllium oxide slabs. Probes of this design, flush-mounted and made of these materials, could withstand the moderate heating rates which exist in thin hypersonic boundary layers prior to transition. After transition, the sharply increased heating rates quickly caused physical deterioration of the probes, although some valid data was obtained between transition and probe failure.

Two types of probes were flown on each flight vehicle. As shown in Figure 11, the two probe types differed only in collector electrode design. The collector and return electrodes of both types were rectangular and had a common dimension (0.50 inch) perpendicular to the flow direction. Collector electrodes of two sizes were used. The large electrodes (0.50 x 0.50 inch) were designed to be sufficiently large that probe edge effects could be neglected, but may have been large enough to cause local depletion of the plasma. The small electrodes (0.50 x 0.06 inch, the same size as all return electrodes) were intended to be sufficiently small that plasma depletion effects could be neglected, although probe edge effects may have been important. Measurements made by these two probe types under equivalent flow conditions were used to estimate possible distortions of the probe currents by these effects.

3.3.2 Electrostatic Probe Electronics

All probes were biased by synchronized linear ramp functions which varied from -10 to +10 volts in 0.1 second. The bias potential for each probe was applied between the collector electrode and the return electrode, the latter being grounded to the internal structure and metallic surface of the vehicle (which acted as an additional return electrode). Currents collected on the probe collector electrodes were amplified by logarithmic amplifiers sensitive in the micro-amp range. The amplifier output

signals (0 to 5 volts dc) were sampled at rates of 1000 sps or 4000 sps and were transmitted to the ground via the telemetry link, providing a full current-voltage characteristic from each probe during every probe bias cycle.

Automated computer processing was used for data reduction and display of the large amount of data received. Plots of single bias voltage sweeps (showing current density vs. applied potential as in Figures 9 and 10) and plots of saturation current density histories (showing saturation current density* vs. altitude as in Figure 12) were obtained from the data tapes by the computer using preflight amplifier calibrations. For both Flight 1 and Flight 2, electrostatic probe data were received from above 90 km to the altitude where physical failure of the probe circuits occurred. For each flight, the data-taking period lasted approximately thirty seconds so that approximately 300 sweeps (each a full current-voltage probe characteristic) of 0.1 seconds duration were obtained from each data channel. Eight probe data channels were used on each vehicle.

3.3.3 Electrostatic Probe Calibration Procedures

The electrostatic probe amplifiers were calibrated in the laboratory prior to flight by measuring the output voltages corresponding to selected input currents. These calibrations were checked during flight by periodically substituting resistors of known value for each probe. For each probe amplifier one calibration cycle, involving the substitution of five different resistors, was performed every sixteen seconds. The inflight calibration data were processed in the same way as the probe flight data, providing a check on the validity of the preflight amplifier calibrations.

3.3.4 Electrostatic Probe Locations

Eight electrostatic probes were located along the heatshield surface of each vehicle. The axial and azimuthal locations of the electrostatic probes on Flights 1 and 2 are given in Figures 13 and 14, respectively.

---

*Saturation current densities were defined as probe current densities measured at bias potentials five volts above and below the bias potential at zero current collection so that they could be evaluated automatically.

3.4 VEHICLE THERMOCOUPLES

3.4.1 Thermocouple Installation

The thermocouple installation details for the Flight 1 and 2 vehicles were identical to those shown in Figure 2 of Reference 13. The chromel-alumel (Type K) thermocouples with grounded junctions were enclosed in 0.020-inch diameter stainless steel sheaths. A spring-loaded thermocouple and a small pure tin slug between the thermocouple junction and the bottom of the heat-shield cavity was used to provide a good thermal contact. The thermocouple cavity was 0.023-inch diameter and resulted in a heatshield wall thickness of $0.005 \begin{smallmatrix} +.003 \\ -.000 \end{smallmatrix}$ inch at the thermocouple tip.

The tin slug remained solid during exit and exoatmospheric flight and melted during vehicle reentry when the heatshield temperature exceeded 450°F. After the tin melted, the spring forced the thermocouple tip against the bottom of the cavity. The flight deceleration and centrifugal forces kept the liquid tin at the end of the cavity surrounding the sheath and maintained the desired wetted metallic contact.

The tin slugs melted prior to boundary layer transition onset for the somewhat blunter conical vehicles described in Reference 13. However, as a result of lower aerodynamic heating rates, these tin slugs did not melt until after boundary layer transition onset for the slender vehicles in this study.

3.4.2 Thermocouple Locations

The eight thermocouples on the Flight 2 vehicle were located at four axial stations along two conical rays 90 degrees apart. The exact sensor locations on this vehicle are given in Table IV.

IV. FLIGHT TEST DATA

The analysis of the vehicle dynamics data from Flight 1, the high angle-of-attack flight, is presented in Section 4.1, while boundary layer transition data for the vehicles at low and high angles-of-attack are presented in Sections 4.2 and 4.3, respectively.

4.1 VEHICLE DYNAMICS ANALYSIS

Vehicle pitch, yaw, and roll attitude angles as a function of time after liftoff were calculated from data provided by the onboard accelerometers and rate gyros. These vehicle attitude angles for Flight 1, the high angle-of-attack flight, are presented as a function of time after liftoff in Figures 2 and 3. As discussed earlier in Section 2.2 only the vehicle dynamics data from Flight 1 required analysis for interpretation of the acoustic sensor data.

The equations used to calculate the vehicle axis angle-of-attack (total angle-of-attack), the location of each sensor with respect to the windward meridian, and the local angle-of-attack history at each sensor are presented below. These parameters were calculated from the vehicle pitch, yaw, and roll attitude angles and the sensor azimuthal angle. The vehicle attitude angles are defined in Figure 4, while the azimuthal angle of the sensor, ϕ_S, is the sensor location in degrees measured clockwise from the vehicle -Z axis looking forward (see Figure 4).

4.1.1 Total Angle-of-Attack

The vehicle total angle-of-attack, α_T, was calculated from the pitch and yaw angles-of-attack using the following equation:

$$\alpha_T = \tan^{-1} \left[\sqrt{\tan^2\alpha + \tan^2\beta} \right] \tag{4.1}$$

4.1.2 Angle Between the Sensor and the Windward Meridian

The sensor/windward angle or location of each sensor with respect to the windward meridian, ψ (measured positive clockwise from sensor to the windward meridian looking forward) was calculated as shown below. Care had to be exercised to ensure that calculated sensor/windward angles were in the proper quadrants since use of trigonometric functions for angles through 360 degrees without quadrant checks would not yield a unique solution. Both the equations for determining the sensor/windward angle and the quadrant check requirements are presented in the following steps.

1) Compute the angle ϕ' using:

$$\phi' = \tan^{-1} \left\{ \cos \alpha_T \left[\frac{\tan \beta - \tan \phi_r \tan \alpha}{\tan \alpha + \tan \phi_r \tan \beta} \right] \right\} \tag{4.2}$$

2) Calculate the angle θ where:

$$\theta = \tan^{-1} \left[\frac{\tan \alpha}{\tan \beta} \right] \quad \text{if } \alpha \geq 0 \text{ and } \beta \geq 0$$

$$\theta = 180° + \tan^{-1} \left[\frac{\tan \alpha}{\tan \beta} \right] \quad \text{if } \alpha \geq 0 \text{ and } \beta < 0 \text{ or } \alpha < 0 \text{ and } \beta < 0 \tag{4.3}$$

$$\theta = 360° + \tan^{-1} \left[\frac{\tan \alpha}{\tan \beta} \right] \quad \text{if } \alpha < 0 \text{ and } \beta \geq 0$$

3) Determine angle γ' using:

$$\gamma' = 270° - \theta - \phi_r \tag{4.4}$$

4) Determine angle γ where:

$$\gamma = \gamma' \qquad \text{if } 0 \leq \gamma' \leq 360°$$
$$\gamma = 360° + \gamma' \qquad \text{if } \gamma' < 0 \tag{4.5}$$
$$\gamma = \gamma' - 360° \qquad \text{if } \gamma' > 360°$$

5) Calculate angle ϕ where:

$$\phi = \phi' \qquad \text{if } 0° \leq \gamma \leq 90° \text{ or } 270° < \gamma \leq 360°$$
$$\phi = 180° + \phi' \qquad \text{if } 90° < \gamma \leq 180° \tag{4.6}$$
$$\phi = \phi' - 180° \qquad \text{if } 180° < \gamma \leq 270°$$

6) Compute angle ψ' using:

$$\psi' = \phi - \phi_S - 180° \tag{4.7}$$

7) Now the sensor/windward angle, ψ is given by:

$$\psi = \psi' \qquad \text{if } -180° \leq \psi' \leq 180°$$
$$\psi = \psi' - 360° \qquad \text{if } \psi' > 180° \tag{4.8}$$
$$\psi = \psi' + 360° \qquad \text{if } \psi' < -180°$$

4.1.3 Local Angle-of-Attack

The local angle-of-attack, θ_L, at each sensor is now calculated from the total angle-of-attack and the sensor/windward angle by

$$\theta_L = \sin^{-1} \left[\cos \alpha_T \sin \theta_c + \cos \theta_c \sin \alpha_T \cos \psi\right] \tag{4.9}$$

where θ_c is the cone half-angle (θ_c = 8 degrees for the vehicles considered in this study).

4.1.4 Reduced Vehicle Dynamics Data

Equations (4.1) through (4.9) were used to calculate local angle-of-attack and sensor/windward angle histories for the three acoustic sensors on Flight 1. Typical calculated local angles-of-attack and sensor angles relative to the windward meridian are presented in Figure 15. The irregular oscillatory nature of the local angle-of-attack is caused by the combined effects of the vehicle pitch, yaw, and roll motions. The sensor angle relative to the windward meridian is normalized between -180 degrees and +180 degrees. In Section 4.3 the local angles-of-attack are presented with the acoustic sensor data, and the times are indicated when the sensors are on both the vehicle windward and leeward meridians.

4.2 ZERO ANGLE-OF-ATTACK BOUNDARY LAYER TRANSITION DATA

Boundary layer transition data from Flights 2 and 3 are presented and analyzed in this section. The acoustic sensor, base pressure and electrostatic probe data have been analyzed and the transition altitude results compared to those obtained from other onboard instruments. In addition, the acoustic sensor and electrostatic probe data from Flight 2 have been correlated to provide an improved basis for interpretation of the high angle-of-attack data from these sensors.

4.2.1 Zero Angle-of-Attack Acoustic Sensor Data

The acoustic sensor data from Flight 2 were analyzed to provide a baseline for interpretation of the high angle-of-attack flight data. Computer processing was used to reduce the acoustic sensor data to sound pressure levels and to generate microfilm data plots with merged support data such as altitude and local angles-of-attack at the sensors.

The rms sound pressure level (SPL) data from the three Flight 2 sensors are shown in Figures 16 through 18; the identification and location of the sensors are noted at the top of each figure. The left hand scale is the SPL in db referenced to 2×10^{-4} dynes/cm^2. The horizontal scale is vehicle altitude, extending from 30 to 50 km. Above the plot of acoustic sensor data is the vehicle centerline angle-of-attack history, α_T (for

small angles-of-attack the local angle-of-attack of the sensor face, θ_L, is α_T plus 8 degrees).

The maximum SPL that can be plotted for any given sensor corresponds to the maximum sensor output (sensor saturation level) as specified in Table III. It can be seen from the figures that all three of the sensors reached saturation.

The data from all three sensors are characterized by a sudden rise to a high plateau region, a sudden drop to a low level, and finally a gradual increase until the sensor reached saturation. The first period of high level data corresponds to a period during which a boundary layer injection experiment was conducted. The effect of this experiment was to "trip" the boundary layer for an altitude range from about 44 to 47 km. Consequently, the following discussion of the transition phenomena is restricted to the period where the injection experiment no longer affected the data.

The altitude of transition onset established by the acoustic sensor data has been defined as the altitude where the SPL data rises suddenly above the 120 db level. This transition onset altitude is designated as h_{t_1} in the figures.

Primarily as a result of the Channel 4 data in Figure 17, the following approach was adopted for selecting the altitude where the boundary layer at each sensor was defined as "fully turbulent". A straight line with a slope proportional to the variation in freestream pressure (equivalent to the variation in local cone pressure because of the near constant freestream Mach number) was matched to the SPL data just prior to sensor saturation. The intersection of the increasing SPL data with this line was selected as the fully turbulent altitude, h_{t_2}, as shown in Figures 16 through 18. Additional justification for using this method was provided by Reference 14 in which acoustic sensor data for an ablating vehicle were analyzed. Reference 14 concluded that "the intensity of the boundary layer pressure fluctuations in the frequency range of the measurement (5 to 200 kHz) was proportional to the static pressure."

The presentation and analysis of data from eight acoustic sensors is included in Reference 14 for an ablating vehicle and will not be repeated

in this report. These SPL data of Reference 14 were characterized by an almost instantaneous rise of an order of magnitude at the onset of transition. The phenomenon of boundary layer transition on the Flight 2 vehicle considered in this study is by comparison much more gradual. This difference is, at least in part, attributed to the high blowing rates at transition onset associated with an ablating heatshield.

The SPL data in Figures 16 through 18 show an error bar of ±2.5 db. Only errors incurred in the processing and handling of the data and the calibration of the sensor system are considered. The power spectrum of the surface pressure fluctuations is assumed to be flat, the finite size of the transducer is neglected, and the plane wave laboratory calibration is used directly. Questions regarding the precise meaning of the processing, the validity of the plane wave calibration, the effects of the finite size of the transducer, or effects of a nonflat spectrum are not considered in this error analysis. The errors are summarized in Table V. A more detailed error analysis is contained in Reference 15.

4.2.2 Zero Angle-of-Attack Base Pressure Data

Base pressure data normalized with the freestream pressure are presented in Figure 19 for similar vehicles with three different heatshield materials. The Flight 2 (nonablating heatshield) data are compared to both Flight 3 (ablating heatshield with strong blowing) data and data obtained from a vehicle with an ablating heatshield for which blowing was weak. A sharp change in base pressure is evident at the transition altitude because of a thickening of the shoulder boundary layer associated with changes in the boundary layer profiles. The increase in base pressure is more pronounced for the vehicle with the strongly blowing heatshield, again because of the greater ablation rate at boundary layer transition. The data from this vehicle indicate boundary layer transition at the vehicle base shoulder at an altitude of 38 km. The data for the nonablating and weakly ablating heatshields indicate a lower boundary layer transition altitude of 36 km ± 1 km.

Transition altitudes established by base pressure measurements have a tendency to be low by comparison to those determined from other flight data because the base pressure responds to changes that occur in the boundary layer somewhat forward of the base. This is demonstrated in the

next section where the data from the different instruments are compared.

The two primary causes of uncertainty in the base pressure measurements are the accuracy limits of the gauge calibration data and response time effects. Both of these sources of error have been examined in Reference 16, and the results of this study are presented in Table VI. Because of low-range data limitations arising from the noted total errors, only data greater than 4 percent of full scale are presented in Figure 19.

4.2.3 Zero Angle-of-Attack Electrostatic Probe Data

Analysis of zero angle-of-attack flight data has shown that electrostatic probe measurements provide a useful indication of the onset of local boundary layer transition at probe locations along vehicle heatshield surfaces. Transition detection using the zero angle-of-attack Flight 2 electrostatic probe data is presented in this report in order to provide a baseline for interpretation of the high angle-of-attack flight data.*

The individual sweep plots and the saturation current density histories for each Flight 2 channel were examined with reference to all available preflight and inflight information relating to the operation of the probe systems, and all invalid data were identified. The primary considerations in this process were found to be leakage currents through the heated beryllium oxide insulators between electrodes, and the available range of the amplifiers (see Reference 11). Valid electrostatic probe data were obtained over an altitude range from approximately 70 km to 25 km.

In general, the zero angle-of-attack data sweeps are smooth and well saturated as shown in Figure 9. The saturation current densities measured at any given probe location (an example is shown in Figure 12) increase continually from amplifier threshold levels at high altitudes to amplifier overflow levels at the lowest altitudes, the only exceptions being measurements made during two boundary layer injection experiments and calibration sweep periods. The saturation current density measurements have been used primarily in the calculation of boundary layer charged

*Transition detection using electrostatic probes mounted along the Flight 3 (strongly ablating) heatshield is discussed in Reference 14.

particle number densities (as in Reference 12 for Flight 2 data). Although the saturation current densities are subject to abrupt increases in magnitude and, to a lesser degree, to increases in scatter when local boundary layer transition occurs, the effects of transition on the electrostatic probe data can be most directly and accurately observed in the individual data sweeps. Only examples of such data are shown in this report (Figures 9 and 10). Complete sets of electrostatic probe data sweeps can be found in References 11 and 17.

It has been found that fluctuations appear in the electrostatic probe sweep data which can be related to the onset of boundary layer transition at each probe station. This was not unexpected since the collected probe currents are dependent upon ambipolar boundary layer properties (see Section 3.3.1), which can be expected to fluctuate with the onset of boundary layer transition. Prior to the onset of such fluctuations, the measured probe currents do not contain fluctuations resolvable above the step size of the sampled data. An example of such measurements is shown in the sweep of Figure 9, where the only changes in measured currents are the continuous changes in level which are due to the ramp function variations in the applied probe potential.

Specific transition onset altitudes have been obtained from the zero angle-of-attack electrostatic probe data by identifying the times at which fluctuations having amplitudes greater than plus or minus one pcm step size* appear in the data. This criterion is not difficult to apply to the Flight 2 data. Those data indicate that such fluctuations do not occur in measurements made while the heatshield boundary layer over the

---

*Currents collected by the probe collector electrodes are amplified by four-decade logarithmic amplifiers. The amplifier output signals (0 to 5 volts dc) are sampled at rates of 1000 sps or 4000 sps and are transmitted to the ground via the telemetry link. The 0 to 5 volt signal range is resolved into 256 pcm (pulse code modulated) steps. On the ground, currents (or current densities) are calculated from the received voltages using preflight amplifier calibrations. The currents are then plotted on a logarithmic scale versus applied probe potential and time to produce the probe "sweeps". On such a plot, one pcm step size then corresponds to 1/128th of the full scale four decade range of either the positive or negative probe currents.

probe is laminar. Furthermore, when fluctuations do appear, the amplitudes tend to be considerably larger than plus or minus one pcm step size. The Flight 2 data show, however, that fluctuations do not necessarily appear continuously in all data measured by a given probe after the first onset of fluctuations at the probe station. For this reason, two types of regions of fluctuating data were identified for Flight 2:

1) A range over which sweeps contain fluctuations in bursts of "short" (or order 1/10 sweep period, or .01 sec*) duration during measurement of data sweeps which are more than 50 percent composed of smooth laminar-type data having no fluctuations (see Figure 20).

2) A range over which sweeps contain continuously fluctuating data (with at most occasional periods of order 1/10 sweep period during which fluctuations are not measured, see Figures 10 and 21).

The resultant zero angle-of-attack transition altitudes as determined from electrostatic probe data are shown in Figure 22. The application of this transition detection criterion to the high angle-of-attack Flight 1 electrostatic probe data is discussed in Section 4.2.7.

4.2.4 Zero Angle-of-Attack Thermocouple Data

Temperature histories of the eight thermocouples on the Flight 2 vehicle are tabulated in Table AI of Appendix A. These data are presented as a function of time after liftoff, TALO, at 0.1 second time increments. Trajectory support data including the time, altitude, vehicle centerline angle-of-attack, and freestream Mach number, velocity, density, temperature and pressure are presented in Tables I and II of the secret addendum to this report, Reference 3. The atmospheric parameters have been obtained as a function of altitude from the 15 degrees North annual atmosphere of Reference 18.

It was beyond the scope of the present study to reduce these temperature/time data to heat transfer rates and determine with the conventional

*The data sample rate is either 1000 sps or 4000 sps for these probes.

approach the onset of boundary layer transition and full turbulence. Instead, boundary layer transition altitudes were estimated for each thermocouple station by determining the altitude where the temperature/time slope departed significantly from the preflight laminar prediction. These transition altitude estimates are discussed in Section 4.2.5 and compared in Figure 22 with results established by other onboard instruments.

4.2.5 Comparison of Zero Angle-of-Attack Transition Data

In order to broaden the data base for boundary layer transition onset on vehicles at zero angle-of-attack, data from other instruments onboard Flights 2 and 3 were studied. These instruments included heatshield thermocouples, base electrostatic probes, base thermocouples and radiometers. The Flight 2 data from the heatshield thermocouples are presented in Reference 2, while the Flight 2 data from the other instruments are presented and validated in Reference 11.

Boundary layer transition altitudes based on these data are presented in Figure 22 as a function of vehicle axial station. Due to the larger number of instrument stations for the heatshield thermocouples and cone electrostatic probes, a mean curve was faired through the combined data from these instruments as shown in Figure 22. The transition altitudes established by the acoustic sensor data presented in Figures 16 through 18 are also presented in Figure 22 for comparison. The altitudes for onset of boundary layer transition established by the acoustic sensor data are about 4 kilometers higher than those determined from the electrostatic probe and vehicle temperature data. This result is consistent with earlier studies conducted on a similar vehicle with an ablating heatshield which showed that measurement of the pressure fluctuations at the vehicle surface with acoustic sensors was the most direct means of detecting boundary layer transition and involved the shortest measurement time constant.

As would be expected, the acoustic sensor "fully turbulent" altitudes are below the transition onset curve established by the other data, with the exception of the data point from the Channel 5 sensor. Considering the low saturation level for this channel (see Table II) and the trend of the sound pressure level data in Figure 18, it is likely that the sensor

saturation occurred prior to the boundary layer becoming fully turbulent at this station. As a result, this data point should be considered less credible than the others.

The altitude for boundary layer transition at the vehicle base station established by the base pressure data is significantly lower than those determined from the other data.

Transition altitudes as a function of vehicle station are presented in Figure 23 for the Flight 3 ablating vehicle. These altitudes are based upon acoustic sensor and base pressure data from Reference 14 and thermocouple and calorimeter data from Reference 19. Because of the good agreement between the acoustic sensor and thermocouple data, a solid curve was faired through these data. Again the base pressure transition altitude is about 1 km low, while the data points based on the calorimeter data are about 5 km low because of a large thermal lag (see Reference 19). For comparison purposes the curve faired through the Flight 2 electrostatic probe and thermocouple data from Figure 22 is shown in Figure 23 as a dashed line. As would be expected, the effects of mass addition to the boundary layer for Flight 3 caused boundary layer transition to occur at higher altitudes than for the nonablating vehicle. This increase in transition altitude ranged from slightly over 1 kilometer at the aft vehicle station to about 5 kilometers at a station at 20 percent of the vehicle length.

4.2.6 Correlation of Flight 2 Acoustic Sensor Data

The acoustic sensor data to this point have been presented and discussed in terms of sound pressure level (SPL). This representation was sufficient for a vehicle which entered the atmosphere near zero angle-of-attack. However, to provide a basis for interpretation of the high angle-of-attack data (Flight 1) it was necessary to relate the rms pressure fluctuation levels to a meaningful local flow condition or parameter at the sensor. A large number of investigators nondimensionalize the pressure fluctuation measurements with a measured or calculated shear stress at the wall, following the lead of Kistler and Chen in Reference 20. This approach can only be adopted when the shear stress levels are well known, which is certainly not the case in a boundary layer transition study such as the present. Other investigators have chosen to nondimensionalize the pressure

fluctuation level data with either the local static or dynamic pressure at the sensor. Preliminary studies were conducted in which the pressure fluctuation data were nondimensionalized with both of these pressures. It was found, however, that a better data correlation was obtained with the local dynamic pressure nondimensionalization and consequently this method was adopted for the present study.

This nondimensionalization of the pressure fluctuation data with the local dynamic pressure was performed using the following equations.

The sound pressure level in db is related to the rms pressure fluctuation level by

$$SPL(db) = 20 \log_{10} (\tilde{P}/P_{ref}) \tag{4.10}$$

where $\tilde{P}$ is the rms surface pressure fluctuation level and P_{ref} is the reference pressure and equals 2×10^{-4} dynes/cm^2.

Using Newtonian theory the cone pressure coefficient, C_p, is given by

$$C_p = \frac{P_c - P_\infty}{q_\infty} = 2 \sin^2 \theta_L \tag{4.11}$$

By rearranging Equation (4.11) the local cone static pressure, P_c, is given by

$$P_c = P_\infty + q_\infty (2 \sin^2 \theta_L) \tag{4.12}$$

where q_∞ is the freestream vehicle dynamic pressure

θ_L is the local angle-of-attack (see Equation 4.9 in Section 4.1.3)

P_∞ is the freestream static pressure. (The 15 degrees North annual atmosphere of Reference 18 was used throughout this study to define the required atmospheric parameters as a function of altitude.)

The local cone dynamic pressure, q_c, is related to the local cone static pressure by

$$q_c/P_c = \frac{1}{2} \gamma M_c^2 \tag{4.13}$$

where γ is the ratio of specific heats (γ = 1.4 was used in this study) and M_c is the local cone Mach number.

Again Newtonian theory is used to determine the local cone Mach number by

$$M_c = \frac{M_\infty \cos \theta_L}{\sqrt{1 + \frac{\gamma - 1}{2} (M_\infty \sin \theta_L)^2}} \tag{4.14}$$

where M_∞ is the freestream Mach number.

The ratio of rms pressure fluctuation level to dynamic pressure at the sensor can be calculated using Equations (4.10) and (4.12) through (4.14) and the instantaneous values of SPL and vehicle attitude, velocity, and altitude.

These calculations were performed for the transition onset and fully turbulent altitudes selected on the basis of the Flight 2 acoustic sensor data in Figures 16 through 18. These results together with the boundary layer transition altitudes and the local angle-of-attack at the sensor at that altitude are presented in Table VII. The ratios of rms surface pressure fluctuation level to the dynamic pressure at the sensor, $\tilde{P}/q_c$, shown in Table VII are calculated from the actual flow angle-of-attack. In addition, $\tilde{P}/q_c$ values calculated for a local angle-of-attack of 8 degrees (centerline angle-of-attack of zero) are shown in brackets for the Channel 5 sensor. For the low angles-of-attack of Flight 2 the assumption of the vehicle centerline at zero angle-of-attack results in less than a 4 percent change in the calculated nondimensional pressure fluctuation levels.

When the boundary layer is fully turbulent, the $\tilde{P}/q_c$ ratios vary from about 5.5×10^{-4} to 9×10^{-4} for this near zero angle-of-attack flight with a nonablating heatshield. In contrast, the ratios at boundary layer transition onset are over an order-of-magnitude lower, ranging from about 3×10^{-5} to 5.5×10^{-5}. These results will be used in the following section where the high angle-of-attack acoustic sensor data are presented and analyzed.

4.2.7 Correlation of Flight 2 Electrostatic Probe Data

The electrostatic probe zero angle-of-attack transition altitudes are

compared with those determined by other onboard instruments in Figure 22. The comparison shows that the electrostatic probe transition altitudes are higher than the acoustic sensor "fully turbulent" results by 0.5 to 1.0 kilometer. For each set of probe data, the altitude range over which sweeps contain continuously fluctuating data [type (2) fluctuations as defined in Section 4.2.3] is the range of altitudes below each indicated electrostatic probe transition altitude. The altitude ranges over which sweeps contain fluctuations in short bursts [type (1) fluctuations as defined in Section 4.2.3] are also shown in Figure 22 and occur above each transition altitude. Data fluctuations of type (1) may be a result of large intermittent turbulent disturbances passing over the probes during the first stages of transition onset. Fluctuations of this type are observed for brief periods at altitudes all of which are lower than the transition onset altitudes measured by the acoustic sensor. This indicates that the electrostatic probes have a higher threshold for transition detection than do the acoustic sensors, although the electrostatic probe data show continuous transition-induced fluctuations at altitudes slightly above the "turbulent" acoustic sensor altitudes.

The range, in the zero angle-of-attack data (Figure 22), over which fluctuations of type (1) are observed before type (2) fluctuations begin is significant because it is not possible to separate fluctuations of type (1) from those of type (2) in the high angle-of-attack (Flight 1) data. The extent of this range, which appears to be at most about 4 kilometers, is an indication of the uncertainty inherent in considering Flight 1 fluctuations to be evidence of a fully turbulent boundary layer as opposed to a transitional boundary layer. Since the Flight 1 data cannot be used to distinguish between transitional and turbulent boundary layers, it can only be said that Flight 1 results identify either laminar or "transitional" behavior, where (based on the comparisons in Figure 22) "transitional" refers to levels of turbulence from approximately that for acoustic sensor "transition-onset" to fully developed turbulence.

The presence of fluctuations (as defined in Section 4.2.3) has been used to identify "transitional" (as defined above) Flight 1 electrostatic probe data. The results are presented in Section 4.3.3.

4.3 HIGH ANGLE-OF-ATTACK BOUNDARY LAYER TRANSITION DATA

The Flight 1 acoustic sensor, base pressure and electrostatic probe data are presented in this section together with qualitative transition altitudes based on vehicle thermocouple instrumentation.

4.3.1 High Angle-of-Attack Acoustic Sensor Data

The rms sound pressure level (SPL) data from the three Flight 1 sensors are shown in Figures 24 through 26; the identification and location of the sensors are noted at the top of each figure. These figures present the basic SPL data from this flight for an altitude range extending from 31 to 50 km. The SPL data in each of these figures are characterized by a series of peaks and valleys with a generally increasing level until the sensors reached saturation.

These data were not analyzed on a point by point basis; instead, curves were faired through the data to yield a continuous best estimated SPL history for each sensor. The equations in Section 4.2.4 were then used to calculate the ratios of rms wall pressure fluctuation level to local dynamic pressure at the sensor, $\tilde{P}/q_c$, as a function of time. However, when the local angle-of-attack was less than zero, the freestream dynamic pressure was used to nondimensionalize the pressure fluctuation level. The $\tilde{P}/q_c$ histories which correspond to the SPL data in Figures 24 through 26 are presented in Figures 27 through 29, respectively. In addition, the vehicle total angle-of-attack history is presented at the top of the same figures, while below the corresponding $\tilde{P}/q_c$ data is the local angle-of-attack history at each sensor. These parameters are presented as a function of time after liftoff (TALO) for a TALO range of 1638 to 1644 seconds which encompasses all acoustic sensor data from the first strong acoustic sensor signals until all sensors were fully saturated. Again, the identification and location of the sensors are noted at the top of each figure.

The surface pressure fluctuation ratios in each figure are characterized by a series of peaks which coincide with the times when the vehicle was at a high local angle-of-attack. The gaps in the $\tilde{P}/q_c$ data correspond to period of sensor saturation (see Figures 24 to 26). In these regions the $\tilde{P}/q_c$ ratios can only be greater than the levels indicated where the data

reaches saturation.

The apparent correlation of the $\tilde{P}/q_c$ peaks with high levels of total angle-of-attack, which can be seen in Figures 27 through 29, actually results from the fact that the local angles-of-attack at the three sensors were near either a maximum or a minimum value when the vehicle total angle-of-attack was at a maximum. The sharp rises in pressure fluctuation level when the sensors are at a high positive local angle-of-attack are of interest in this study because they are caused by boundary layer transition. The high $\tilde{P}/q_c$ spikes which coincide with negative local angles-of-attack at the sensors are believed to be a result of a high turbulence level in the separated flow region on the leeward side of the vehicle. These regions of high pressure fluctuation level, which are marked with an asterisk (*) in Figures 27 through 29, were not analyzed because an investigation of separated flow turbulence was beyond the scope of the present study.

The first sensor signal for all three channels occurred at a TALO of about 1638.45 seconds. Although these signals are strong, the data is believed questionable because of the simultaneous occurrence of a strong vehicle vibration. The origin of this vibration is unknown but it is quite possible that it could have resulted in the indicated acoustic sensor response. Similar vibration levels were not measured with the vibration sensor at the other pressure fluctuation peaks which again casts suspicion on the first acoustic sensor signals. The first acoustic data peak with the Channel 5 sensor (see Figure 29) could be explained on the basis of the sensor being in a region of separated flow. However, the signals at the same time from the Channel 3 and 4 sensors cannot be explained on the basis of turbulent flow conditions at the sensors because of an inadequate combination of vehicle attitude and altitude conditions. This fact will be demonstrated later when flow field calculations are made for conditions corresponding to various $\tilde{P}/q_c$ levels.

These flow field calculations were performed for several cases; the case numbers and TALO for which they were calculated are shown in Figures 27 through 29 with a number and arrow. Emphasis was placed on calculations for conditions when the sensors were on the vehicle windward ray. The times when the sensors were on both the cone windward and leeward meridian

are indicated along the axis of each local angle-of-attack plot.

A dashed line has been placed through the $\tilde{P}/q_c$ data at a level of 9×10^{-4}. This is the "fully turbulent" level established by the Flight 2 data in Section 4.2.6. Pressure fluctuation levels above this value should indicate the presence of a turbulent boundary layer at that station if the sensor is not in a region of separated flow. Negligible levels, on the other hand, should indicate the presence of a laminar boundary layer, while values between these levels indicate a transitional boundary layer.

The following eight flow field cases were computed based on the Channel 3 acoustic sensor data (see Figure 27).

- Case 9: Peak level of $\tilde{P}/q_c$, sensor close to windward ray (turbulent)
- Case 10: Sensor on windward ray near $\tilde{P}/q_c$ peak (turbulent)
- Case 11: Peak level of $\tilde{P}/q_c$ and sensor on windward ray (turbulent)
- Case 12: Sensor on windward ray with intermediate $\tilde{P}/q_c$ level (transitional)
- Case 13: Peak level of $\tilde{P}/q_c$, sensor not close to either windward or leeward ray (turbulent level-sensor in separated flow)
- Case 14: Apparent peak level of $\tilde{P}/q_c$ although sensor saturated (turbulent)
- Case 15: Sensor on windward ray with intermediate $\tilde{P}/q_c$ level (transitional)
- Case 16: Sensor on windward ray with negligible $\tilde{P}/q_c$ level (laminar)

The Channel 4 and 5 sensors provided less acoustic data than the Channel 3 sensor because of their location further aft on the vehicle which caused earlier boundary layer transition and sensor saturation at a higher altitude. The following five flow field cases were analyzed based on the Channel 4 data (see Figure 28).

- Case 22: Peak level of $\tilde{P}/q_c$ which appears questionable (turbulent?)
- Case 23: Peak level of $\tilde{P}/q_c$ although sensor is saturated, a high local angle-of-attack (turbulent)

- Case 24: Sensor on windward ray with what appears could be a $\tilde{P}/q_c$ peak if the sensor was not saturated (turbulent)
- Case 25: Sensor on windward ray with an intermediate $\tilde{P}/q_c$ level (transitional)
- Case 26: Sensor on windward ray with an intermediate $\tilde{P}/q_c$ level (transitional)

Only four flow field cases were of interest based on the Channel 5 data. These cases are listed below (see Figure 29).

- Case 42: Local angle-of-attack at a maximum with a high but sensor saturated $\tilde{P}/q_c$ level (turbulent)
- Case 43: Apparent peak level of $\tilde{P}/q_c$ with the sensor saturated (turbulent)
- Case 44: Local angle-of-attack at a maximum with a high but sensor saturated $\tilde{P}/q_c$ level (turbulent)
- Case 45: Apparent peak level of $\tilde{P}/q_c$ with the sensor saturated (turbulent)

The results of flow field calculations corresponding to the above cases are presented in Section 5.3.2 following a description of the flow field analysis. Correlations of the high angle-of-attack transition data utilizing these flow field results are then presented in Section VI.

Prior to presenting the Flight 1 base pressure and electrostatic probe data and qualitative transition results from Flight 1 thermocouple data a brief comparison will be made between the acoustic sensor data from Flights 1 and 2. Channel 3 sound pressure level (SPL) data from these two flights are presented together in Figure 30. The Flight 1 data are presented as in Figure 24, while the Flight 2 data from Figure 16 have been shifted along the TALO scale so the altitudes for the two flights correspond at any given time. Since the velocity/altitude characteristics of the two flights were very similar, this will ensure that the freestream Mach numbers and Reynolds numbers for the two vehicles will almost be equal at a given TALO in Figure 30. Consequently, the difference in the SPL characteristics from the two flights should only be caused by the high angle-of-attack of Flight 1 during reentry. If the first peak of Flight 1 SPL data is ignored

(data is questionable for the reasons discussed earlier), the Flight 1 midcone sensor responds to a turbulent boundary (intermittent because of the varying angle-of-attack) about 10 km higher in altitude than the Flight 2 midcone sensor first responds to transition onset. At a TALO of about 1641 seconds the Flight 1 acoustic sensor still fluctuates in level but in the mean gradually increases until the sensor reaches saturation. A dashed line has been placed through the mean of the minimum levels of SPL in this region of generally increasing SPL. Figure 27 shows that these minimum levels of SPL correspond to minimum vehicle total angles-of-attack ranging from about 5 degrees at a TALO of 1641.4 seconds to 2.5 degrees at a TALO of 1643.4 seconds. As shown in Figure 30, the difference in altitudes between the minimum level Flight 1 data and the Flight 2 data are about 3 km and 2 km at sound pressure levels of 120 db ($\alpha_T \sim 5$ degrees) and 150 db ($\alpha_T \sim 2.5$ degrees), respectively. In the same period that the Flight 1 minimum total angle-of-attack decreased from 5 to 2.5 degrees the local angle-of-attack at the Channel 3 sensor had values at the five minimum levels in the Flight 1 data of about 4, 5, 9, 6, and 10 degrees.

A comparison of the Channel 4 and 5 data from Flights 1 and 2 showed similar trends to those presented here based on the more extensive Channel 3 data. On the basis of the facts presented above, it would appear that the acoustic sensor transition data are more directly affected by the vehicle total angle-of-attack than by the local angle-of-attack at the sensor. The reason for this behavior is not well understood but may be connected with the strong crossflow on cones at even small angles-of-attack.

4.3.2 High Angle-of-Attack Base Pressure Data

Flight 1 base pressure data normalized with the freestream pressure are presented in Figure 31 for an altitude range from 90 km to 30 km. The vehicle total angle-of-attack history is plotted below this data for the same range of altitude. The base pressure data shows a pronounced pressure variation because of vehicle angle-of-attack. This effect arises because the high cone pressure generated by excessive vehicle oscillation was fed aft through the separated boundary layer to the base region. The observed oscillations in base pressure correlate well with

the total angle-of-attack variations. Boundary layer transition onset at the base of this vehicle was not detectable from the base pressure data. Accuracy of the base pressure data was determined to be ±4 percent of full scale (see discussions of data errors in Section 4.2.2).

4.3.3 High Angle-of-Attack Electrostatic Probe Data

Examples of the saturation current density histories measured by the electrostatic probes on Flight 1 are shown in Figures 32 and 33. Also shown are the histories of total and local angle-of-attack, and of sensor/windward angle, for the probe locations at which the data were measured. The saturation current density histories shown in the figures are typical of those measured by all probes on Flight 1 in that large amplitude fluctuations were measured which correlate with total and local angle-of-attack. Over the portion of the altitude range where local and total angle-of-attack variations were of nearly equal period, the amplitude of the saturation current density fluctuations tend to be larger for probes located along azimuths for which variation in total and local angle-of-attack are nearly in phase (Figure 32) than for probes along azimuths where the angles-of-attack are nearly out of phase (Figure 33). The large changes in saturation current density levels are produced by variations in boundary layer densities and profiles which are due to the changes in vehicle altitude and attitude during reentry. Flight 1 saturation current histories cannot be used to distinguish laminar and transitional regimes. They do, however, provide an indication of the altitude ranges over which the individual data sweeps can be expected to provide such information. When the measured saturation currents are outside the range of the amplifiers, all or part of the currents measured during the corresponding sweep periods will be outside the amplifier range and will not be useful for transition detection. This occurs over different altitude ranges for different probes depending upon axial probe location, azimuthal probe location, and probe type. The full set of saturation current density histories for Flight 1 can be found in Reference 10. In addition to the altitude ranges excluded from consideration by the limits of the amplifiers, altitude ranges have been excluded where the probe data were affected either by vehicle nose outgassing (only at very high altitudes), boundary layer injection experiments, or interruptions for calibration sweep measurements (see References 9 through 12 for details). Electrostatic

probe measurements made within these excluded altitude ranges cannot be used as a source of information on boundary layer transition. Windward ray electrostatic probe data which were subject to one or more of these effects are identified in Table IX of this report and in Table III of the addendum, Reference 3.

The individual Flight 1 electrostatic probe data sweeps have been used to investigate boundary layer transition at each probe heatshield location. This has been done using the criterion developed for the zero angle-of-attack data and described in Section 4.2.3. Although large excursions in saturation current levels were measured during reentry, the changes in measured saturation current levels during single sweep periods were generally small enough that the individual current-voltage characteristics were qualitatively of the same form as those measured on Flight 2 (see Figures 9, 10, 20, 21, 34, 35 and 36). Examination of the useful data ranges (described above) shows that fluctuations appear in the data sweeps at higher altitudes on Flight 1 than on Flight 2 (particularly at rear probe locations), and that in many cases there are periods of laminar-type data without fluctuations between periods of fluctuating data. As described below, all data measured while probes were located along the windward ray or at ±5 degrees from the windward ray have been examined for evidence of boundary layer transition. In addition, some data obtained at much larger sensor/windward angles have been analyzed.

4.3.3.1 Measurements on Windward Ray

The electrostatic probes on Flight 1 were located along the heatshield surface at three azimuthal locations (ϕ_s = 0, 150 and 180 degrees) as shown in Figure 13. The times at which each of these azimuthal locations passed through the windward ray during reentry are given in Table III of Reference 3.* Also given in the same table are the times at which the probe azimuth locations were five degrees on either side of the windward ray. The probes did not pass through the windward ray at the same rate in each case, but did so at a rate determined by the corresponding rate of change of vehicle attitude. The time interval for the passage of probes from -5 degrees sensor/windward angle to +5 degrees sensor/windward angle varied

*Table III of Reference 3 contains the information in Table IX of this report together with the associated times after lift-off, vehicle velocities, altitudes, and freestream densities, temperatures, pressures and viscosities.

from approximately ten percent of a sweep period to nearly a full sweep period (0.1 second). The electrostatic probe measurements made at -5, 0 and +5 degree sensor/windward locations were examined to determine whether the data indicated that the boundary layer was locally laminar or transitional. With only a few exceptions (see Table IX of this report and Table III, Reference 3), the transition results obtained from the -5 and +5 degree sensor/windward measurements were the same as the transition result from the corresponding windward ray measurements. The freestream conditions (Mach number, velocity, temperature, pressure and density), altitude, and angles-of-attack (total and local) at the time of each windward ray probe measurement are given in Table IV of Reference 3. Freestream density, temperature, pressure, and viscosity have been evaluated for each altitude, using the U. S. Standard Atmosphere, 15 degrees North Annual of Reference 18. Freestream Mach number and velocity, altitude, and total angle-of-attack are also given for each -5 and +5 degree sensor/windward measurement. The Standard Atmosphere freestream properties are not listed for the ±5 degree measurements because it was found that they differed from the windward ray values by no more than a few percent.

Each windward ray probe measurement has been assigned a case number in Table IX of this report and Table III of Reference 3. Flow field calculations of local Mach number and Reynolds number based on local boundary layer displacement thickness have been made for each case. The results, which are given in the same tables, have been used to correlate the electrostatic probe windward ray transition results in Section VI.

4.3.3.2 Measurements off Windward Ray

With the exception of the excluded altitude ranges referred to above, the Flight 1 electrostatic probe measurements constitute a potential source of boundary layer transition information over the full range of reentry altitudes and vehicle attitudes. Although investigation of boundary layer transition using windward ray measurements was the primary objective of this study, certain measurements made at sensor/windward angles greater than ±5 degrees have been examined. Several criteria were used to select the measurements which were examined. First the investigation was restricted to data obtained while probes were located at sensor/windward angles no

greater than ±90 degrees. This was done to establish a reasonable upper bound on the sensor/windward angles for the flowfield calculations. Even with this restriction, the amount of data available for analysis was beyond the scope of this effort, since measurements were made at six axial stations while vehicle attitude and reentry altitude were continuously changing. Investigation of "off windward ray" data was therefore further restricted to:

(a) measurements made at or near each onset of fluctuations in the probe data. Included in this set were measurements (sampled at short time intervals and only when the sensor/windward angle was <90 degrees, see Table IX of this report and Table V of Reference 3) which were made during the period of data fluctuations that followed each onset. (Figure 36 shows an example of onset during a single sweep period and identifies the corresponding samples used in the tables.) These measurements were selected because they provide a sampling of the range of reentry conditions for which the electrostatic probe data indicate the presence of local boundary layer transition or turbulence. It should be noted, however, that this sampled range of conditions does not include cases where the boundary layer may have been turbulent while probe currents were outside the amplifier range, or cases where data fluctuations occurred in measurements made at sensor/windward angles >90 degrees (which often occurred).

(b) measurements (primarily of smooth laminar-type data) which were made at or near local angle-of-attack maxima. These measurements were selected to provide a sampling of the largest angle-of-attack conditions under which the electrostatic probe data indicate that the boundary layer was laminar (or, in several cases, transitional). Here, too, it should be noted that this sampled range of conditions does not include cases where the boundary layer may have been laminar while probe currents were outside the amplifier range.

The transition results, attitude conditions, and flowfield parameters for the measurements described in (a) and (b) above are summarized in Table IX of this report and presented in detail in Table V and Table VI of Reference 3, respectively. Flowfield calculations of local Mach number and local Reynolds number based on boundary layer displacement thickness for these data were beyond the scope of this effort and so the "off windward ray" results are not plotted in the figures of this report.

4.3.4 High Angle-of-Attack Thermocouple Data

Temperature data as a function of time were obtained from eight forebody thermocouples on the Flight 1 vehicle. These thermocouples were located at four axial stations along two conical rays 90 degrees apart. The

thermocouple installations and locations were identical to those described in Section 4.2.4 for the Flight 2 vehicle. Plots of the temperature history data for each thermocouple are presented in Reference 1 and, consequently, are not repeated here.

Boundary layer transition onset altitudes were estimated for each thermocouple station by determining the altitude where the temperature/time slope departed significantly from the preflight laminar prediction. These boundary layer transition altitudes and estimated error bars are presented in Figure 37 as a function of vehicle axial station. The error bands were established by the difference in the transition altitudes estimated from the two thermocouples at each axial station. Since these data were not reduced to heat transfer rates and because of the angle-of-attack effects in the data, it is quite possible that the errors are greater than those shown.

As a basis for comparison, the altitudes at which the acoustic sensors first responded with a strong turbulent signal (questionable signal at TALO = 1638.45 seconds was not used) and also when they fully saturated are shown in Figure 37. It can be seen that the acoustic sensors responded to intermittent turbulent conditions at altitudes well above those presently determined from the thermocouple data. The temperature data from the thermocouples did show a slight variation with vehicle angle-of-attack, but this was essentially ignored in the selection of the transition onset altitudes. As a result of this and thermal lag effects inherent in this type of measurement, the transition altitudes presented are actually based on an integrated or averaged heating rate history. It is quite possible that if the thermocouple data were reduced to heat transfer rates, these data would also show intermittent transitional or turbulent boundary layers at higher altitudes.

Also presented in Figure 37 for comparison are the vehicle transition altitudes established by the Flight 2 electrostatic probe and thermocouple data. Comparison of the transition onset altitudes for Flights 1 and 2 based on these thermocouple data substantiates the acoustic sensors result that vehicle angle-of-attack tends to increase the boundary layer transition altitude. The thermocouple data indicate that the difference in transition altitude varies from about 5.5 km at the aft vehicle station to about

2.5 km at a midcone station. These results and the transition altitudes determined from the Flight 1 thermocouple data should only be considered in a qualitative sense because of the nature of the data and the method used to select the transition altitudes.

V. FLOW FIELD ANALYSIS

A flow field analysis for a cone at angle-of-attack was performed in an attempt to correlate the boundary layer transition flight data presented in Section IV with instantaneous flow parameters. The main objective was to develop an engineering approach for estimating the flow field about a sharp cone for angles-of-attack up to 40 degrees.

5.1 GENERAL APPROACH

The flow field around cones at high angle-of-attack is extremely complicated. With the help of some recent experiments, it is well recognized that the problem is basically one involving a viscous-inviscid interaction for which no satisfactory solution has as yet been reported. In fact, because of the existence of a vortical singularity on the leeward meridianal plane, even a solution to the inviscid flow field is not a trivial matter as demonstrated by Stocker and Mauger in Reference 21. In spite of these difficulties, an approximate calculation scheme has been developed and is presented here in which the inviscid surface streamlines are determined for a given angle-of-attack and freestream condition by relating the external pressure field to the local geometry. With this solution, the boundary layer characteristics, such as the displacement thickness and the momentum thickness, along the inviscid surface streamlines are estimated using a local similarity approximation. The viscous-inviscid interaction between the external flow field and the boundary layer is also accounted for in this analysis. However, the vorticity interaction was ignored for the relatively sharp-nosed configurations of interest here. The analysis uses real gas properties and does not account for real gas effects.

5.2 ANALYSIS

5.2.1 Governing Equations

Let ξ and η be the orthogonal curvilinear coordinates on the cone surface and ζ be the distance measured normal to the surface. Furthermore, let h_1, h_2 be the metric coefficients associated with this coordinate system. Then, a differential line element is given by

$$(d\ell)^2 = h_1^2\, d\xi^2 + h_2^2\, d\eta^2 + d\zeta^2 \tag{5.1}$$

When the boundary layer thickness is small compared with the cone radius, the metrics h_1 and h_2 may be considered as functions of ξ and η only.

Let u, v, and w represent the corresponding velocity components in this coordinate. Then, the boundary layer equations become:

Continuity

$$\frac{\partial}{\partial \xi}(\rho u h_2) + \frac{\partial}{\partial \eta}(\rho v h_1) + \frac{\partial}{\partial \zeta}(\rho w h_1 h_2) = 0 \tag{5.2}$$

Momentum

$$\frac{\rho u}{h_1}\frac{\partial u}{\partial \xi} + \frac{\rho v}{h_2}\frac{\partial u}{\partial \eta} + \rho w \frac{\partial u}{\partial \zeta} - K_2 \rho u v + K_1 \rho v^2 = -\frac{1}{h_1}\frac{\partial p}{\partial \xi} + \frac{\partial}{\partial \xi}\left(\mu \frac{\partial u}{\partial \zeta}\right) \tag{5.3}$$

$$\frac{\rho u}{h_1}\frac{\partial v}{\partial \xi} + \frac{\rho v}{h_2}\frac{\partial v}{\partial \eta} + \rho w \frac{\partial v}{\partial \zeta} - K_1 \rho u v + K_2 \rho u^2 = -\frac{1}{h_2}\frac{\partial p}{\partial \eta} + \frac{\partial}{\partial \zeta}\left(\mu \frac{\partial v}{\partial \zeta}\right) \tag{5.4}$$

$$\frac{\partial p}{\partial \zeta} = 0 \tag{5.5}$$

Energy

$$\frac{\rho u}{h_1}\frac{\partial H}{\partial \xi} + \frac{\rho v}{h_2}\frac{\partial H}{\partial \eta} + \rho w \frac{\partial H}{\partial \zeta} = \frac{\partial}{\partial \zeta}\left(\frac{\mu}{P_r}\frac{\partial H}{\partial \zeta}\right) + \frac{\partial}{\partial \zeta}\left[\frac{P_r - 1}{P_r}\mu \frac{\partial}{\partial \zeta}\left(\frac{u^2+v^2+w^2}{2}\right)\right] \tag{5.6}$$

where $H = h + \frac{1}{2}(u^2 + v^2 + w^2)$ is the total enthalpy.

And, K_1 and K_2 denote the curvatures of lines ξ = constant and η = constant, respectively, and are given by

$$K_1 = -\frac{1}{h_1 h_2}\frac{\partial h_2}{\partial \xi}, \quad K_2 = -\frac{1}{h_1 h_2}\frac{\partial h_1}{\partial \eta} \tag{5.7}$$

5.2.1.1 Inviscid Field

At the edge of the boundary layer, Equation (5.4) becomes

$$K_2 \rho u^2 = -\frac{1}{h_2}\frac{\partial p}{\partial \eta} \tag{5.8}$$

by taking η = constant along the inviscid streamline.

Now, let (R, Φ) be the polar coordinates on the developed cone surface, as shown on the following sketch.

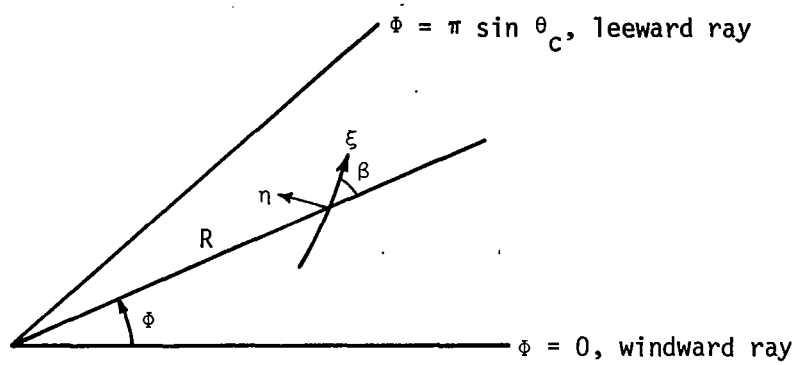

The angle Φ on the sketch is defined by $\Phi = \psi \sin \theta_c$ with ψ being the azimuthal angle measured clockwise from the windward meridian when viewing from the base, and θ_c being the cone half-angle. Furthermore, let β be the angle between the inviscid streamline and the ray Φ = constant. Then the streamline curvature K_2 is given from the geometry by

$$K_2 = \frac{1}{h_1} \frac{\partial}{\partial \xi} (\beta + \Phi) \tag{5.9}$$

Combining Equations (5.8) and (5.9) gives

$$\frac{1}{h_1} \frac{\partial \beta}{\partial \xi} + \frac{1}{h_1} \frac{\partial \Phi}{\partial \xi} = - \frac{1}{\rho_e u_e^2 h_2} \frac{\partial p}{\partial \eta} \tag{5.10}$$

Also, from the geometry

$$\frac{1}{h_1} \frac{\partial R}{\partial \xi} = \cos \beta \tag{5.11}$$

and

$$\frac{1}{h_1}\frac{\partial\Phi}{\partial\xi} = \frac{1}{R}\sin\beta \tag{5.12}$$

Moreover, since the cone is a developable surface

$$\frac{\partial}{\partial\xi}\left(\frac{1}{h_1}\frac{\partial h_2}{\partial\xi}\right) + \frac{\partial}{\partial\eta}\left(\frac{1}{h_2}\frac{\partial h_1}{\partial\eta}\right) = 0 \tag{5.13}$$

Then, Equations (5.7) and (5.8) yield

$$\frac{1}{h_1}\frac{\partial}{\partial\xi}\left(\frac{1}{h_1}\frac{\partial h_2}{\partial\xi}\right) + \left[\frac{1}{h_2}\frac{\partial}{\partial\eta}\left(\frac{1}{\rho_e u_e^2 h_2}\frac{\partial p}{\partial\eta}\right) + \left(\frac{1}{\rho_e u_e^2 h_2}\frac{\partial p}{\partial\eta}\right)^2\right] h_2 = 0 \tag{5.14}$$

Equations (5.10), (5.11), (5.12), and (5.14) determine the inviscid surface streamline if the pressure is known as functions of ξ and η. The four unknowns β, Φ, R, and h_2 describe the geometry of the surface streamline.

5.2.1.2 Boundary Layer

In the inviscid surface streamline coordinates, the crossflow velocity v vanishes both at the wall and at the edge of boundary layer. Therefore, if the pressure gradient normal to the streamline, $\partial p/\partial\eta$, (and hence the streamline curvature) is not too large, the crossflow velocity will be small across the entire boundary layer. As a first order approximation, the boundary layer equations for small crossflow may be written as

$$\frac{\partial}{\partial\xi}(\rho u h_2) + \frac{\partial}{\partial\zeta}(\rho w h_1 h_2) = 0 \tag{5.15}$$

$$\frac{\rho u}{h_1}\frac{\partial u}{\partial\xi} + \rho w\frac{\partial u}{\partial\zeta} + \frac{1}{h_1}\frac{\partial p}{\partial\xi} = \frac{\partial}{\partial\zeta}\left(\mu\frac{\partial u}{\partial\zeta}\right) \tag{5.16}$$

$$\frac{\rho u}{h_1}\frac{\partial H}{\partial\xi} + \rho w\frac{\partial H}{\partial\zeta} = \frac{\partial}{\partial\zeta}\left(\frac{\mu}{P_r}\frac{\partial H}{\partial\zeta}\right) - \frac{\partial}{\partial\zeta}\left(\frac{1 - P_r}{P_r}\mu u\frac{\partial u}{\partial\zeta}\right) \tag{5.17}$$

Now, define the transformed coordinates by

$$\tilde{s}(\xi;\eta) = \int_0^{\xi} \frac{\rho_e u_e \mu_e}{\rho_\infty u_\infty \mu_\infty} \frac{h_2^2}{L} \frac{h_1}{L} d\xi \tag{5.18}$$

$$z(\xi,\zeta;\eta) = \frac{R_\infty^{1/2} u_e h_2}{u_\infty L^2 \sqrt{2\tilde{s}}} \int_0^{\zeta} \frac{\rho}{\rho_\infty} d\zeta \tag{5.19}$$

where

$$R_\infty \equiv \frac{\rho_\infty u_\infty L}{\mu_\infty}$$

Also, let

$$\frac{u}{u_e} = f_z(\tilde{s},z) \tag{5.20}$$

$$\frac{H}{H_e} = 1 + S(\tilde{s},z) \tag{5.21}$$

with subscripts z and $\tilde{s}$ indicating partial differentiations. Then, the governing equations can be written as

$$(Cf_{zz})_z + ff_{zz} - \left(\frac{\rho_e}{\rho} - f_z^2\right) \frac{2\tilde{s}}{\rho_e u_e^2} \frac{\partial p}{\partial \tilde{s}} = 2\tilde{s}(f_z f_{\tilde{s}} - f_{\tilde{s}} f_{zz})$$

$$\left(\frac{C}{P_r} S_z\right)_z + fS_z - \frac{u_e^2}{H_e} \left(\frac{1 - P_r}{P_r} Cf_z f_{zz}\right)_z = 2\tilde{s}(f_z S_{\tilde{s}} - f_{\tilde{s}} S_z)$$

$$C = \frac{\rho\mu}{\rho_e \mu_e} \tag{5.22}$$

Similarity solutions for Equations (5.22) exist only under special circumstances. For example, if the rate of change of the pressure gradient parameter

$$\bar{\beta} = - \frac{H_e}{h_e} \frac{2\tilde{s}}{\rho_e u_e^2} \frac{\partial p}{\partial \tilde{s}} \tag{5.23}$$

along $\tilde{s}$ is small, the flow may be considered as locally similar and Equation (5.22) may be approximated by

$$(Cf_{zz})_z + ff_{zz} + \bar{\beta}(1 + S - f_z^2) = 0$$

$$\left(\frac{C}{P_r} S_z\right)_z + fS_z - \bar{\gamma}\left(\frac{1 - P_r}{P_r} Cf_z f_{zz}\right)_z = 0 \qquad (5.24)$$

where

$$\bar{\gamma} = \frac{u_e^2}{H_e} \approx 2 \text{ for } M_e >> 1.$$

Solutions to Equation (5.24) with various boundary conditions are well known (e.g., Dewey and Gross have presented a compilation of similar solutions for a wide variety of physical situations in Reference 22). Based on the similarity solutions, the boundary layer momentum thickness is obtained from

$$\frac{\theta^*}{L} = \frac{\rho_\infty u_\infty L}{\rho_e u_e h_2} R_\infty^{-1/2} \sqrt{2\tilde{s}}\ I_1(\bar{\beta}) \qquad (5.25)$$

where

$$I_1(\bar{\beta}) = \int_0^\infty f_z(1 - f_z)dz$$

The displacement thickness is similarly obtained from

$$\frac{\delta^*}{L} = \frac{\rho_\infty u_\infty L}{\rho_e u_e h_2} R_\infty^{-1/2} \sqrt{2\tilde{s}} \left[\frac{T_o}{T_e} I_2 - I_1\right] \qquad (5.26)$$

where

$$I_2 = \int_0^\infty (1 - f_z^2)dz - \left(1 - \frac{T_w}{T_o}\right) \int_0^\infty (1 - G)dz$$

and

$$G = \frac{H - H_w}{H_e - H_w}$$

A correction caused by the crossflow within the boundary layer may be obtained by computing the crossflow velocity component v by neglecting the convective term ($v\ \partial v/\partial \eta$) in the crossflow momentum Equation (5.4). Then, the correction to u, w, and H may be obtained from the full equations by treating v terms as forcing functions. For the present investigation, this correction was not performed.

5.2.2 Inviscid Pressure Field

It is apparent from the governing equations that the pressure field outside the boundary layer has to be specified or linked to the local geometry. Since the Mach number range of interest in the present investigation was of the order of 20, the Newtonian pressure field gave a good approximation. The experiment of Tracy (Reference 23) clearly demonstrated the adequacy of a simple Newtonian representation by comparison to other more sophisticated theories. If the interaction caused by the growth of the boundary layer displacement thickness is taken into account, an even better agreement of the Newtonian theory with Tracy's data is expected. However, for a cone at high angle-of-attack, the Newtonian representation is definitely in error in the "shadow" region near the leeward ray. On the other hand, none of the more sophisticated inviscid theories give a correct description in this region because of the strong interaction with the viscous crossflow. Therefore, a Newtonian pressure field was used in the present investigation and the pressure in the "shadow" region was assumed to be the freestream value.

The Newtonian angle, θ_L, is defined as the angle between the tangent to the surface and the freestream velocity. Thus, θ_L is generally greater than zero. At the stagnation point, $\theta_L = \pi/2$. When the freestream velocity vector coincides with the surface, $\theta_L = 0$. For $\theta_L < 0$, θ_L is set to zero as a result of the constant pressure shadow region assumption discussed above.

According to Newtonian theory, the pressure coefficient is defined by

$$C_p = \frac{P - P_\infty}{\frac{1}{2}\rho_\infty u_\infty^2} = 2 \sin^2 \theta_L \tag{5.27}$$

and

$$\frac{u_e}{u_\infty} = \cos \theta_L \tag{5.28}$$

The static temperature is similarly obtained from

$$\frac{T_e}{T_\infty} = 1 + \frac{\gamma - 1}{2} M_\infty^2 \sin^2\theta_L \tag{5.29}$$

For the purpose of estimating the local Reynolds number, it is further assumed that $\mu \sim T$. All other variables of interest can also be related to this Newtonian angle, θ_L. For a given cone half-angle, θ_c and angle-of-attack, α the Newtonian angle is related to the azimuthal angle, ψ by:

$$\sin \theta_L = \sin \theta_c \cos \alpha + \cos \theta_c \sin \alpha \cos \psi \tag{5.30}$$

5.2.3 Method of Solution

Let $h_1 d\xi = ds$ and $L = 1$, the final set of governing equations are

$$\begin{aligned}
\frac{dR}{ds} &= \cos \beta \\
\frac{d\psi}{ds} &= \frac{\sin \beta}{R \sin \theta_c} \\
\frac{d\beta}{ds} &= - 2F_1 \sin \theta_L \cos \theta_L \frac{1}{h_2} \frac{\partial \theta_L}{\partial \eta} - \sin \theta_c \frac{d\psi}{ds} \\
\frac{d\tilde{s}}{ds} &= (1 + 1.4M_\infty^2 \sin^2\theta_L) \cos \theta_L h_2^2
\end{aligned} \tag{5.31}$$

$$\frac{dh_2}{ds} = H_1$$

$$\frac{dH_1}{ds} = - h_2 \left[4F_1^2 \sin^2\theta_L \left(\cos\theta_L \frac{1}{h_2}\frac{\partial\theta_L}{\partial\eta}\right)^2 + 2F_1F_2 \sin\theta_L \left(\cos\theta_L \frac{1}{h_2}\frac{\partial\theta_L}{\partial\eta}\right) \right.$$

$$\left. + 2F_1 \left\{ \left(\cos\theta_L \frac{1}{h_2}\frac{\partial\theta_L}{\partial\eta}\right)^2 + \sin\theta_L \frac{1}{h_2}\frac{\partial}{\partial\eta}\left(\cos\theta_L \frac{1}{h_2}\frac{\partial\theta_L}{\partial\eta}\right) \right\} \right]$$

where

$$F_1(\theta_L) \quad \frac{\rho_\infty u_\infty^2}{\rho_e u_e^2} = \frac{1}{\cos^2\theta_L} \; \frac{1 + 0.2M_\infty^2 \sin^2\theta_L}{1 + 1.4M_\infty^2 \sin^2\theta_L}; \; F_2 = \frac{1}{F_1}\frac{1}{h_2}\frac{\partial F_1}{\partial\eta}$$

Solution to this set of equations describes the inviscid surface streamline. The boundary layer characteristics are obtained by first estimating the pressure gradient parameter, $\bar{\beta}$.

$$\bar{\beta} = - \frac{1 + 0.2M_\infty^2}{1 + 0.2M_\infty^2 \sin^2\theta_L} \; \frac{4F_1\tilde{s} \sin\theta_L \cos\theta_L \frac{d\theta_L}{ds}}{(\tilde{ds}/ds)} \tag{5.32}$$

Then, the displacement thickness is given by

$$\delta^* = F_1 \cos\theta_L \frac{R_\infty^{-1/2}}{h_2} \sqrt{2\tilde{s}} \left[\frac{T_o}{T_e} I_2 - I_1 \right] \tag{5.33}$$

and the momentum thickness

$$\theta^* = F_1 \cos\theta_L \frac{R_\infty^{-1/2}}{h_2} \sqrt{2\tilde{s}} \; I_1 \tag{5.34}$$

The integrals I_1 and I_2 as functions of the pressure gradient parameter $\bar{\beta}$ are obtained from Dewey and Gross' similarity solutions.

Since relatively high altitude flights are of primary interest in the present study, the freestream Reynolds number may be low enough such that the interaction caused by the growth of boundary layer should be considered. This interaction is accounted for by modifying the local surface inclination. Specifically, the local cone angle and azimuthal angle become $(\theta_c + \delta_R^*)$ and $(\Phi - \delta_\psi^*/R \sin \theta_c)$, respectively. Here the subscripts R and ψ indicate partial differentiations and are further approximated by

$$\delta_R^* = \frac{\cos \beta}{h_1} \frac{\partial \delta^*}{\partial \xi}$$

$$\frac{1}{R \sin \theta_c} \delta_\psi^* = \frac{\sin \beta}{h_1} \frac{\partial \delta^*}{\partial \xi} \tag{5.35}$$

The rate of growth of the boundary layer displacement thickness across the streamline has been neglected in obtaining Equations (5.35). With this displacement thickness interaction included, Equation (5.30) becomes

$$\begin{aligned} \sin \theta_L &= \cos \theta_c \sin \alpha \cos \psi + \sin \theta_c \cos \alpha \\ &+ \frac{d\delta^*}{ds} \Big[\cos \beta \, (\cos \theta_c \cos \alpha - \sin \theta_c \sin \alpha \cos \psi) \\ &+ \sin \beta \cos \theta_c \sin \alpha \sin \psi \Big] \end{aligned} \tag{5.36}$$

The rate of change of the displacement thickness, δ^*, along the streamline can be obtained from Equation (5.33) and then used in Equation (5.36) to estimate the Newtonian angle, θ_L, at the next station. This method of solution is not an exact interaction model which requires a simultaneous integration of δ^* together with the remaining unknowns. However, because of the relatively high Reynolds number flow considered, this set of equations is very "stiff" and is difficult to handle numerically. The present alternate method of solution is believed to give a fair approximation to the full interaction result and does not pose any numerical problem.

5.2.4 Initial Conditions

The complete set of governing equations can be readily integrated numerically with the proper initial conditions. It should be noted that as R tends to zero (sharp-pointed cone), the equations become singular. However, for all practical situations, there is a small spherical nosetip. Since the streamline on a spherical section is always a great circle passing through the stagnation point, certain closed form solutions can be obtained if the viscous-inviscid interaction is ignored on the spherical section. Then the initial conditions at the sphere-cone junction can be estimated.

Each streamline is characterized by an initial azimuthal angle, ψ_o, at the sphere-cone junction. For a spherical cap of radius r_o, the geometry gives

$$R = r_o \operatorname{ctn} \theta_c \tag{5.37}$$

Let O' be the center of the sphere, S the stagnation point and P be a point on the sphere-cone junction with $\psi = \psi_o$. Then the angle Θ_o defined by the angle formed by SO'P is given by

$$\cos \Theta_o = \cos \alpha \sin \theta_c + \cos \theta_c \sin \alpha \cos \psi_o \tag{5.38}$$

and the streamline passing through P is the circular arc along the sphere surface from S to P. For any point Q on the streamline, the angle defined by the angle formed by SO'Q is related by the local inclination by

$$\cos \Theta = \cos \alpha \sin \theta_\ell + \cos \theta_\ell \sin \alpha \cos \psi_\ell \tag{5.39}$$

with subscript ℓ referring to local values. The remaining initial conditions can be easily shown to be

$$h_{20} = r_o \sin \Theta_o$$

$$H_{10} = \cos \Theta_o$$

$$\beta_o = \tan^{-1} \frac{\sin \alpha \sin \psi_o}{\cos \theta_c \cos \alpha - \sin \theta_c \sin \alpha \cos \psi_o} \tag{5.40}$$

$$\tilde{s}_o = r_o^3 \left[\frac{2}{3} + \frac{2.8M_\infty^2}{15} - \cos \Theta_o \left\{ 1 - \frac{1 - 1.4M_\infty^2}{3} \cos^2\Theta_o - \frac{1.4M_\infty^2}{5} \cos^4\Theta_o \right\} \right]$$

$$\delta_o^* = \frac{1 + 0.2M_\infty^2\cos^2\Theta_o}{1 + 1.4M_\infty^2\cos^2\Theta_o} \frac{R_\infty^{-1/2}}{\sin^2\Theta_o} \frac{\sqrt{2\tilde{s}_o}}{r_o} \left[\frac{1 + 0.2M_\infty^2}{1 + 0.2M_\infty^2\cos^2\Theta_o} I_2 - I_1 \right]$$

After estimating the derivative $(d\delta^*/ds)_o$, the initial Newtonian angle is given by

$$\sin \theta_o = \cos \Theta_o + \left(\frac{d\delta^*}{ds}\right)_o \left[\cos \beta_o (\cos \theta_c \cos \alpha - \sin \theta_c \sin \alpha \cos \psi_o) + \sin \beta_o \cos \theta_c \sin \alpha \sin \psi_o\right] \tag{5.41}$$

5.3 RESULTS AND DISCUSSIONS

The flow field analysis described in Section 5.2 was developed primarily for the purpose of calculating inviscid and viscous flow parameters for specific vehicle attitude and flow conditions. In order to demonstrate general features of the flow field several cases were computed which yielded results of general interest for hypersonic flow over cones at angle-of-attack. These results are presented in Section 5.3.1 while the specific results to support the boundary layer transition analysis are presented in Section 5.3.2.

5.3.1 General Flow Field Results

As a test case, a calculation was performed for the sharp-nosed (r_o = 0.1-inch) 8-degree half-angle cone at zero angle-of-attack and a freestream condition of $M_\infty = 22.4$ and $R_{\infty,r_b} = 4.8 \times 10^6$. The growth of the boundary layer displacement thickness as a function of the distance along the cone axis is shown in Figure 38. The characteristic length has been taken as the base radius r_b = 2 feet.

Figure 39 shows the top view of several surface streamlines on a polar coordinate plot for an angle of attack $\alpha_T = 12°$ ($\alpha_T/\theta_c = 1.5$) at $M_\infty = 21.7$ and $R_\infty = 2.8 \times 10^6$. Figure 40 shows the same plot for a higher angle-of-attack ($\alpha_T/\theta_c = 3.5$) and altitude. Notice that, except for the windward streamline, all streamlines are turned away from the windward ray by the azimuthal pressure gradient. It is interesting to note that this convergence of streamlines on the leeward side has been a main concern for people interested in nosetip transpiration cooling.

Figure 41 demonstrates the change in pressure gradient for three streamlines. The windward streamline ($\psi_0 = 0$) shows a practically constant pressure as expected. Only a slight pressure rise over the inviscid value is observed near the nose because of the weak interaction effect at this high Reynolds number. For most of the streamlines off the windward ray, a rapidly decreasing pressure is experienced as the streamline is turned away from the windward meridian. Figure 42 shows the change of azimuthal angle along the streamline $\psi_0 = 2.5°$ and the corresponding growth of the boundary layer displacement thickness. For the purposes of comparison, the corresponding boundary layer growth on the windward meridian is shown on the same plot. The thickening of the boundary layer as it passes from the windward to the leeward side can be visualized from this plot.

For the purpose of correlation of the transition data, it was sometimes desirable to obtain the local flow conditions at sensors located off the windward meridian. Figure 43 shows the local Mach number, M_L, as a function of the meridian angle ψ at $x/r_0 = 1$ for a freestream Mach number of 21.7 and an angle-of-attack of 12 degrees. For this angle-of-attack the shadow region starts at $\psi = 131°$. Figure 44 gives the corresponding variation in the local Reynolds number based on the boundary layer displacement and momentum thicknesses. Figure 45 shows a cross plot of the last two figures in terms of $R_{\delta*}$ vs M_L. Two presumed transition correlation curves are also shown on the plot. First, consider correlation I. According to this correlation, the windward side is more unstable than the leeward. The opposite is true for correlation II. This relation may offer

the possible explanation to the conflicting test results concerning the effect of angle-of-attack on the transition location movement. However, it should be emphasized that the crossflow interaction may play an important role in this regard and has been ignored in the present analysis.

Figures 46 and 47 indicate the effects of angle-of-attack on the local conditions on the windward rays. It is interesting to note that the local unit Reynolds number becomes less than the freestream value for $\alpha_T \gtrsim 5°$.

5.3.2 Flow Field Results for Flight 1 Transition Analysis

Flow field calculations were performed for specific vehicle attitude and flow conditions experienced by the Flight 1 vehicle during reentry. These calculations were performed initially to support the analysis of the acoustic sensor data and were then extended in the second phase of the study to provide additional results for analysis of the electrostatic probe data.

The local cone Mach number and local Reynolds number based on the boundary layer momentum and displacement thicknesses and wetted length to the sensor were calculated for each acoustic sensor case. It was hoped that these parameters could be used to correlate the acoustic sensor transition data. The calculations were straightforward for the cases where the acoustic sensor was on the windward meridian. However, when the sensor was off the windward ray a trial-and-error technique was adopted in which the initial streamline angle at the vehicle nose was varied until a solution was obtained along a streamline which passed over the sensor.

The results of these calculations are presented in Table VIII together with the vehicle attitude conditions and nondimensional wall pressure fluctuation levels. The results for the cases with the sensor on the windward meridian are presented first for each sensor. The vehicle velocity and altitude which correspond to each case are not given in Table VIII for security reasons as discussed in the report introduction. Instead, these parameters are listed by case number in Table VII of the addendum to this report, Reference 3. For many of the calculation cases the corresponding wall pressure fluctuation levels are

identified only as being greater than a certain value because the sensors were saturated.

Results of calculations of local Mach number and local Reynolds number based on displacement thickness for electrostatic probe windward ray cases are presented in Table III of the of the addendum.

These tabulated flow field results for both the acoustic sensors and electrostatic probes are utilized in Section VI where attempts are made to correlate the boundary layer transition results in terms of these parameters.

VI. CORRELATION OF BOUNDARY LAYER TRANSITION DATA

6.1 CORRELATION OF ZERO ANGLE-OF-ATTACK DATA

The problem of predicting transition from laminar to turbulent flow is a difficult task due to the large number of factors which affect the flow but which are not independent of each other. Stability theory while not complete enough to imply exactly what parameters should be used to correlate transition data does provide some theoretical guidance in the selection of parameters. In Reference 24, Lees and Reshotko present a stability theory for laminar compressible boundary layer which takes into account the effect of temperature fluctuations on the viscous disturbances. Their results indicate that the minimum critical Reynolds number is likely to increase sharply with increasing Mach number at hypersonic speeds. This trend has been verified by experimental studies (References 25 through 31). From these experimental and theoretical studies it is apparent that of the many parameters affecting transition two of the most important are the Mach number and the Reynolds number based on the properties at the edge of the boundary layer. The question of what length to use in calculating the Reynolds number has as yet no definite answer. Frequently used lengths are the wetted length and the boundary layer momentum and displacement thicknesses.

Flight test data on boundary layer transition have been correlated for nonablating vehicles which entered the atmosphere at small angles-of-attack. This study performed by TRW Systems is documented in Reference 32. The reentry data considered in this correlation were obtained from flight tests of sphere-cone reentry vehicles. All vehicles had graphite nose tips with 0.25-inch nose radii (Flights 1 and 2 vehicles had nose radii of 0.1-inch). Three of the eight vehicles had cone half-angles of 8 degrees, two had 10 degree half-angles, and three had 22 degree half-angles. Since the trajectories of all vehicles considered were nearly identical, the cone angle was the primary vehicle configuration variable.

Most of the transition data were obtained from thermal sensors embedded in the surface of the vehicles. For the data considered in this earlier

study, the point at which the temperature slope changed was quite abrupt and allowed the altitude of transition to be determined within 1 KM. The transition data from the 10 degree half-angle vehicles were based on accelerometer data. Upon transition there was an increase in vibration and an increase in deceleration due to the higher drag coefficient associated with turbulent flow. The data for one of the other flights were based on radar determined plots of ballistic coefficient versus altitude. The increase in the drag coefficient associated with transition caused the ballistic coefficient to decrease as transition occurred. In both the accelerometer and ballistic coefficient methods, the altitude of transition was presumed to indicate the onset of transition at the base of the vehicle.

Additional details on these vehicles and the methods used to interpret the transition onset altitudes are contained in Reference 32. The method used in this Reference to calculate the local flow properties includes the effects of nose bluntness and the associated curved bow-shock wave as well as real gas properties. This method of calculation is not, therefore, strictly equivalent to the method developed as part of this study for calculation of local flowfield properties for cones at angles-of-attack (described in Section V). In order to provide a basis for a consistent comparison of the zero angle-of-attack transition results from Reference 32 and the high angle-of-attack transition results from this study, local flowfield properties were calculated from the actual transition data of Reference 32 (transition altitudes, freestream velocities and Mach numbers, etc.) using the method discussed in Section V.

The correlations of these zero angle-of-attack transition data are presented in Figures 48 through 50 in terms of the local Mach number and local Reynolds number based on the wetted length and the boundary layer momentum and displacement thicknesses. In each figure the zero angle-of-attack data are represented by bars which encompass all flight data points. These bars are placed at local Mach numbers of 5.3 and 12.8 since the majority of the data were obtained for these conditions. Dashed lines have been placed in each figure which encompass the available zero angle-of-attack transition data. It should be noted that these lines have been extrapolated beyond the range of data only as a reference for the high

angle-of-attack data.

First consider the boundary layer transition data in terms of the local Reynolds number based on wetted length versus the local Mach number as presented in Figure 48. At a given Mach number the zero angle-of-attack flight transition data have about a $\pm$ 35 percent variation in the local Reynolds number based on wetted length. The shaded band in Figure 48 shows the variation in transition Reynolds number with local Mach number on sharp cone models in a 22-inch helium wind tunnel (Reference 27). The transition Reynolds numbers from this wind tunnel test are somewhat lower than the zero angle-of-attack flight data. This difference is probably related to the higher level of freestream turbulence associated with the wind tunnel data.

In Figure 49 the zero angle-of-attack flight transition data are presented with local Reynolds number based on boundary layer momentum thickness versus local Mach number. In this form the zero angle-of-attack data have a variation in the local Reynolds number of about 20 percent from the mean. A similar variation of slightly less than $\pm$ 20 percent is shown by the local Reynolds number based on boundary layer displacement thickness in Figure 50. The use of a local Reynolds number based on either the boundary layer displacement or momentum thickness appears to correlate the zero angle-of-attack transition data to a reasonable degree.

6.2 CORRELATION OF ACOUSTIC SENSOR DATA

Also presented in Figures 48 through 50 are the calculated Flight 1 flow field parameters discussed in Section 5.3.2 and presented in Table VIII. The symbols used to represent the calculated flow field results for each acoustic sensor channel are identified at the top of each figure. Solid symbols indicate that the corresponding pressure fluctuation levels are greater than 9×10^{-4} (turbulent), open symbols indicate levels below 3×10^{-5} (laminar), and flagged symbols indicate that the values of $\tilde{P}/q_c$ are between 3×10^{-5} and 9×10^{-4} (transitional). Each data point in the figure is identified with a number which corresponds to the calculation case number. The results of all the flow field calculations performed are presented in Figures 48 through 50, with the exception of the local

flow properties for case 13 which had a strong acoustic sensor signal as a result of separated flow at the sensor.

Four of the five data points corresponding to laminar or transitional pressure fluctuation levels ($\tilde{P}/q_c < 9 \times 10^{-4}$) are in the local Mach range from 8 to 10 because of relatively low local angles-of-attack between 11 and 14 degrees. The one exception is case 25 which has a local Mach number of about 3.7 as a result of a high local angle-of-attack at the sensor of 30.8 degrees.

In contrast, all eleven data points which correspond to turbulent pressure fluctuation levels ($\tilde{P}/q_c > 9 \times 10^{-4}$) range between local Mach numbers of 3.5 and 7 because of relatively high local angles-of-attack from about 17 to 31 degrees.

In general, the relation of the calculated flow parameters from one case to another are fairly well maintained in all three correlations (i.e., in Figures 48 through 50). For example, the calculated flow parameters for cases 9 and 10 fall below the trend of the data while cases 14, 15, 24, 44, and 45 are consistently above the trend. It is quite apparent that the Flight 1 data are best correlated with the local Reynolds number based on boundary layer displacement thickness versus the local Mach number (i.e., in Figure 50 as compared to Figures 48 and 49). The correlation of local Reynolds number based on wetted length to the sensor versus local Mach number (Figure 48) is particularly poor.

As a result of these comparisons, the electrostatic probe data are presented and discussed in Section 6.3 only in terms of the boundary layer displacement thickness correlation. In addition, comparisons of the combined high angle-of-attack acoustic sensor and electrostatic probe data to the low angle-of-attack transition data are made only in terms of this correlation (Section 6.4).

It was anticipated that the proximity of the Flight 1 data points to the zero angle-of-attack data would vary in relation to the corresponding magnitude of the wall pressure fluctuation levels. For example, it was expected that the flow field conditions corresponding to the onset of a turbulent signal would be close to the zero angle-of-attack transition

correlation whereas a negligible signal such as in case 16 would result in a local Reynolds number below the data correlation. It should be noted again that the data bars representing the range of zero angle-of-attack data are based on transition onset, not full turbulence of the boundary layer. Also, the placement of the straight lines on this semilogarithmic plot bracketing the zero angle-of-attack data may not be correct for the full range of local Mach numbers but was done only to provide a reference for comparison of the angle-of-attack data.

The data points for laminar case 16 and for transitional case 15 are slightly above the linear interpolation of the zero angle-of-attack data. However, all fully turbulent points in the local Mach number range from about 5 to 7 fall close to or in the range of the zero angle-of-attack transition onset data. At the lower local Mach numbers the angle-of-attack data tends to fall below the linear extrapolation of the zero angle-of-attack data. Additional comments are made on these data points in Section 6.4 where the acoustic sensor results are compared to the data from the electrostatic probes.

All acoustic sensor results appear to be self-consistent except for cases 10 and 25. The sensors were on the vehicle windward meridian for both of these cases and in addition the vehicle attitude and freestream conditions were almost identical. As a result, the Reynolds number at the aft cone sensor (case 25) is larger than at the midcone sensor (case 10) for all three length parameters used to calculate the Reynolds numbers. The surprising and unexplained result is that the wall pressure fluctuation level is higher at the midcone sensor than at the aft sensor.

6.3 CORRELATION OF ELECTROSTATIC PROBE WINDWARD RAY DATA

The windward ray electrostatic probe transition results, in terms of calculated local Mach numbers and Reynolds numbers based on local displacement thickness, are shown in Figure 51. Each symbol is identified by case number so that the data in the figure can be related to the appropriate altitude and flow field information in Table IX of this report and Tables III and IV of Reference 3. Solid symbols identify results for which the probe data sweeps contain fluctuations which indicate that the boundary layer was locally transitional or turbulent. The open symbols identify

results for which the probe sweeps contain smoothly varying data (without fluctuations) which indicate that the boundary layer was locally laminar. Flagged symbols identify cases where the measured data sweeps contain fluctuations of order ±1 pcm step size, and therefore do not strictly meet the transition criterion of Section 4.2.3, but are also not smooth laminar-type measurements. These results apparently correspond to measurements made just at the threshold of electrostatic probe transition detection.

The seven turbulent (or transitional) data points in Figure 51 lie within a range of local Mach number of 6 to 10.4, corresponding to a range of local angle-of-attack of 19 to 11 degrees. The laminar data points extend to lower local Mach numbers, covering a range of values of from 3 to 10. The range of local angle-of-attack covered by the laminar data is from 35 to 11 degrees. The absence of turbulent (or transitional) windward ray data points at the lowest local Mach numbers is due primarily to the tendency of windward ray probe currents to exceed the upper limit of the amplifier range at the highest angles-of-attack. Since probe currents also tended to increase with decreasing altitude, the windward ray measurements at the highest angles-of-attack were within the amplifier range at the higher altitudes where Reynolds numbers were relatively low, but not at the lower altitudes where Reynolds numbers were higher and where transition may have occurred.

The addition of results calculated from the transition data in Table V of Reference 3 (measurements made at locations off the windward ray) should widen the range of local Mach numbers covered by turbulent (or transitional) data points. This is expected because nearly all the data in that table correspond to turbulent (or transitional) measurements and cover a wide range of local angle-of-attack (from 24 to 9 degrees). In addition, since Table VI of Reference 3 identifies laminar boundary layer measurements made at or near local angle-of-attack maxima, results calculated from the data in Table V combined with those from Table VI (both from Reference 3) should provide an improved description of transition at the lower local Mach numbers.

The windward ray results alone, however, do provide a reasonably good description of boundary layer transition over the range of local Mach

numbers from 6 to 11. The results are consistent in that the changeover from laminar to turbulent data at fixed local Mach number always corresponds to increasing Reynolds number, and the indicated Reynolds numbers for transition increase continuously with increasing local Mach number. In addition, several sets of windward ray data show the transition from laminar to turbulent behavior along the vehicle surface at fixed altitude. This can be seen by comparing results obtained at a fixed altitude by probes located along a single vehicle ray. In particular, two sets of data from probes on ϕ_s = 0 degrees (cases 8-17-26 and 9-18) and two sets from probes on ϕ_s = 180 degrees (cases 37-48-59-70 and 38-49-60-71) correspond to conditions where forward stations were laminar while stations further aft were turbulent.

The zero angle-of-attack data discussed in Section 6.1 are shown with the windward ray electrostatic probe results in Figure 51. Over the range of local Mach number from approximately 6 to 11, where there are both laminar and turbulent electrostatic probe data points, the rate of change of the indicated transition Reynolds number with local Mach number agrees well with the rate of change defined by the slope of the line which has been drawn through the zero angle-of-attack results. The actual magnitudes of the critical Reynolds numbers indicated by the probe data, however, are somewhat higher than those defined by the extrapolated band of zero angle-of-attack results. This is particularly true at local Mach numbers between 8 and 10, where there are laminar probe results at Reynolds numbers above the range of zero angle-of-attack transition values. This apparent tendency of the electrostatic probe results to be higher than the zero angle-of-attack values is more likely to be due simply to the fact that a straight line has been used to connect the zero angle-of-attack data points than to angle-of-attack effects. Additional zero angle-of-attack data at local Mach numbers other than 5.3 or 12.8 may indicate that a more correct approximation to the variation of zero angle-of-attack transition Reynolds number with local Mach number would be a curve such as that which has been drawn through the high angle-of-attack data in Figure 52.

6.4 CORRELATION OF ACOUSTIC SENSOR AND ELECTROSTATIC PROBE DATA

The transition results obtained from both the acoustic sensor data and the windward ray electrostatic probe data are presented in Figure 52 in terms of local Reynolds number based on displacement thickness and local Mach number. The combined results complement one another in that the range of local Mach number for which there are both laminar and turbulent data points is greater than for either set of results alone. The indicated transition Reynolds numbers from the two sets of data are consistent, the only exceptions being the pair of acoustic sensor points at local Mach number 3.7 (discussed in Section 6.2) and several data points near local Mach number 6.5 to 7.0 (where two electrostatic probe laminar results occur at Reynolds numbers equal to or slightly higher than two acoustic sensor turbulent results). The latter inconsistency may be due, at least in part, to the fact that the electrostatic probes tend to detect transition at lower altitudes than the acoustic sensors (as discussed in Section 4.2.7).

Also shown in Figure 52 are the zero angle-of-attack data (discussed in Section 6.1) and the straight lines which have been used to extrapolate those data over the range of local Mach number for which there is high angle-of-attack data. Over the upper half of that local Mach number range (i.e., for local Mach numbers between 7 and 11), there is good qualitative agreement between the high angle-of-attack data and the extrapolation of the zero angle-of-attack results. Over most of this range, the transition Reynolds numbers indicated by the high angle-of-attack data points tend to be slightly above the extrapolated zero angle-of-attack levels. This difference tends to decrease with decreasing local Mach number, however, and for local Mach numbers between about 5 and 7 the indicated high angle-of-attack transition Reynolds numbers fall within the band of zero angle-of-attack data. At still lower local Mach numbers, the high angle-of-attack results are below the zero angle-of-attack data extrapolation, and the difference increases with decreasing local Mach number.

If the straight line extrapolation of the zero angle-of-attack data were known to be correct, the comparison in Figure 52 would provide a measure of the effects of crossflow and angle-of-attack on boundary layer transition, since decreases in local Mach number correspond to increases in

angle-of-attack for a given vehicle geometry. The comparison in Figure 52 would then indicate that only at angles-of-attack corresponding to local Mach numbers less than about 5 do high angle-of-attack transition Reynolds numbers (based on displacement thickness) differ appreciably from those for zero angle-of-attack. In addition, the comparison would show that when angle-of-attack effects on transition are significant, they tend to result in transition onset at local Reynolds numbers (based on displacement thickness) lower than those for zero angle-of-attack transition onset at the same local Mach number.

The zero angle-of-attack data in Figure 52 is not, however, sufficient to accurately describe the variation of zero angle-of-attack transition Reynolds number over the required range of local Mach number. For this reason, and because there is good agreement between zero angle-of-attack and high angle-of-attack results where direct comparison can be made, it cannot be assumed that the differences between the extrapolated zero angle-of-attack data and the high angle-of-attack data in Figure 52 are necessarily representative of real angle-of-attack effects. The extrapolation in Figure 52 can only be considered a first order approximation to the magnitude and variation of zero angle-of-attack transition Reynolds number over the indicated range of local Mach number. The comparison in Figure 52, therefore, shows simply that the magnitude and local Mach number dependence of the high angle-of-attack and zero angle-of-attack data are in general agreement over most of the local Mach number range.

The combined acoustic sensor and electrostatic probe transition results are correlated sufficiently well by the parameters of Figure 52 that they can be used, without regard to the zero angle-of-attack extrapolation, to describe the variation of transition Reynolds number with local Mach number. The result is the dashed curve shown in the figure. Since the zero angle-of-attack data points also fall on or near the curve, it appears possible that additional zero angle-of-attack transition data may also tend to describe such a curve rather than the straight line used in the figure. The indicated variation of transition Reynolds number with local Mach number is greatest at low local Mach numbers, and decreases as local Mach number increases.

VII. CONCLUSIONS AND RECOMMENDATIONS

Boundary layer transition data have been obtained from acoustic sensor and electrostatic probe measurements made along the surface of a conical nonablating vehicle during a high angle-of-attack reentry. The data correspond to a range of local angle-of-attack at the sensor locations of from 8 to 31 degrees. Observations and conclusions which have been made directly from these data include:

- Acoustic sensors have a lower threshold for transition detection than all other instrumentation (electrostatic probes, thermocouples and base pressure gages) installed in these reentry vehicles. The altitudes for onset of boundary layer transition established by the acoustic sensor data for the Flight 2 vehicle are about 4 km higher than those established by the electrostatic probe and vehicle temperature data. The electrostatic probe transition altitudes are higher than the acoustic sensor "fully turbulent" results by about 0.5 to 1.0 km.

- Boundary layer transition results based on vehicle thermocouple measurements for both Flights 1 and 2 should be treated as only qualitative since a reduction of these data to heat transfer rates for a more rigorous analysis was beyond the scope of this study.

- Boundary layer transition altitudes established for the Flight 2 vehicle by the electrostatic probe data are in good agreement with the qualitative thermocouple results over the range of vehicle axial stations. This agreement is demonstrated in Figure 22.

- Analysis of the Flight 2 acoustic sensor data show that the ratio of rms surface pressure fluctuation level to local dynamic pressure at the sensors varied from a range of 3×10^{-5} to 5.5×10^{-5} at transition onset to a range of 5.5×10^{-4} to 9×10^{-4} (an order of magnitude larger) for "fully turbulent" conditions.

- Comparisons of transition data from a vehicle with an ablating heatshield and the Flight 2 nonablating vehicle indicate that boundary layer transition occurred at higher altitudes, and the transition process was much more abrupt, for the ablating heatshield vehicle. The increase in transition altitude caused by ablative mass addition effects ranged from slightly over 1 km at the aft vehicle station to about 5 km at a station located at 20 percent of the vehicle length.

- Comparison of boundary layer transition altitudes measured on the Flight 1 and 2 vehicles indicate that high angles-of-attack caused boundary layer transition (which was at first intermittent) to occur at higher altitudes on Flight 1 than on the zero angle-of-attack flight (Flight 2).

A method of flowfield analysis has been developed which can be used to calculate local flowfield parameters about sharp cones at high angles-of-attack. This analysis utilizes Newtonian theory to describe the inviscid flow field and a local similarity solution for the viscous flow. Boundary layer crossflow and viscous-inviscid interaction effects have been included. Local flowfield parameters have been calculated as a part of this study for all acoustic sensor transition results and all windward ray electrostatic probe transition results.

Comparisons of correlations of high angle-of-attack transition data using Re_x, Re_θ, and $Re_\delta{}^*$ versus M_L indicate the data are best correlated in terms of $Re_\delta{}^*$ versus M_L. The combined results of the acoustic sensor and windward ray electrostatic probe measurements have been correlated sufficiently well using $Re_\delta{}^*$ versus M_L that the data can be used to describe the variation of indicated transition $Re_\delta{}^*$ with M_L over a range of M_L from approximately 3 to 11. This correlation indicates that the variation of transition $Re_\delta{}^*$ with M_L becomes greater as M_L decreases.

Comparison (in terms of $Re_\delta{}^*$ versus M_L) of the high angle-of-attack transition data with an extrapolation of zero angle-of-attack transition data (at $M_L = 5.3$ and $M_L = 12.8$) shows generally good agreement for $M_L \gtrsim 5$. For $M_L \lesssim 5$, the high angle-of-attack data show transition at values of $Re_\delta{}^*$ lower than values produced by a semi-log plot straight line extrapolation (power law variation) of the zero angle-of-attack data.

The flight data presented in this report were all obtained under nearly identical reentry conditions for which vehicle angle-of-attack and cone angle were the only parameters which changed significantly. For this reason, and because all flowfield parameters were calculated using a single analysis method, the results of this study are self-consistent and can be compared and correlated without ambiguity. The flowfield analysis which has been developed as part of this study does not, however, include real gas properties. Since real gas effects may become significant for high freestream Mach number reentry at high angle-of-attack (or for large cone angle), a study of the effect of including real gas properties in flowfield calculations of parameters such as $R_\delta{}^*$ and M_L should be undertaken. The

results of such a study would indicate what corrections, if any, are required to assure that comparisons of transition data from flows which may be subject to real gas effects (such as those in this study) with transition data from flows where real gas effects are definitely negligible are made in terms of self-consistent flowfield parameters.

A large amount of boundary layer transition data obtained from analysis of electrostatic probe data has been presented for which flowfield calculations have not been performed. The flowfield analysis developed as part of this study should be applied to these data to considerably enlarge the base of high angle-of-attack transition results for use in flowfield parameter correlations.

The Flight 2 thermocouple temperature history data presented in Appendix A should be reduced to heat transfer rates. This would allow transition onset and "fully turbulent" altitudes to be accurately defined and would broaden the base of zero angle-of-attack boundary layer transition data. In addition, preliminary studies could be conducted with the Flight 1 thermocouple data to investigate whether further analysis would provide useful data to supplement the present high angle-of-attack acoustic sensor and electrostatic probe results.

Additional zero angle-of-attack transition data (at local Mach numbers between 3 and 12) should be acquired to make possible (using the high angle-of-attack results presented here) a quantitative assessment of the relationship between high angle-of-attack and zero angle-of-attack boundary layer transition criteria.

REFERENCES

1-2 (See corresponding reference numbers in Reference 3.)

3. Haigh, W. W., Lake, B. M., and Ko, D. R. S., Addendum to Analysis of Flight Data on Boundary Layer Transition at High Angles-of-Attack," TRW Systems Report No. 17181-6001-R3-81, March 1971 (Secret). (NASA CR-1914)

4-12 (See corresponding reference numbers in Reference 3.)

13. Sherman, M. M. and Nakamura, T., "Flight Test Measurements of Boundary Layer Transition on a Nonablating 22° Cone," Journal of Spacecraft, Vol. 7, No. 2, February 1970, pp. 137-142.

14-17 (See corresponding reference numbers in Reference 3.)

18. U. S. Standard Atmosphere Supplements, 1966.

19. (See corresponding reference number in Reference 3.)

20. Kistler, A. L. and Chen, W. S., "The Fluctuating Pressure Field in a Supersonic Turbulent Boundary Layer," Jet Propulsion Laboratory Report TR-32-277, 15 August 1962.

21. Stocker, P. M. and Mauger, F. E., "Supersonic Flow Past Cones of General Cross-Section," Journal of Fluid Mechanics, Vol. 13, pp. 383-399, 1962.

22. Dewey, C. F., Jr. and Gross, J. F., "Exact Similar Solutions of the Laminar Boundary Layer Solutions," The Rand Corp. Memo RM-5089-ARPA, July 1967.

23. Tracy, R. R., "Hypersonic Flow Over a Yawed Circular Cone," GALCIT Memo No. 69, August 1963.

24. Lees, L. and Reshotko, E., "Stability of the Compressible Laminar Boundary Layer," Journal of Fluid Mechanics, Vol. 12, pp. 555-590, 1962.

25. Nagamatsu, H. T., Graber, B. C., and Sheer, R. E., "Roughness, Bluntness, and Angle-of-Attack Effects on Hypersonic Boundary-Layer Transition," Journal of Fluid Mechanics, Vol. 24, Part I, pp. 1-31, 1966.

26. Nagamatsu, H. T., Sheer, R. E., and Graber, B. C., "Hypersonic Laminar Boundary-Layer Transition on 8-Foot-Long, 10° Cone, M_1 = 9.1 -16," AIAA Journal, Vol. 5, No. 7, pp. 1245-1252, July 1967.

27. Maddalon, D. V. and Henderson, A., Jr., "Boundary Layer Transition on Sharp Cones at Hypersonic Mach Numbers," AIAA Journal, Vol. 6, No. 3, pp. 424-431, March 1968.

28. Potter, J. L., "Observations on the Influence of Ambient Pressure on Boundary Layer Transition," AIAA Journal, Vol. 6, No. 10, pp. 1907-1911, October 1968.

29. Whitfield, J. D. and Iannuzzi, F. A., "Experiments on Roughness Effects on Cone Boundary Layer Transition up to Mach 16," AIAA Journal, Vol. 7, No. 3, pp. 465-470, March 1969.

30. Pate, S. R. and Scheler, C. J., "Radiated Aerodynamic Noise Effects on Boundary Layer Transition in Supersonic and Hypersonic Wind Tunnels," AIAA Journal, Vol. 7, No. 3, pp. 450-457, March 1969.

31. Softley, E. J., Braber, B. C., and Zempel, R. E., "Experimental Observation of Transition of the Hypersonic Boundary Layer," AIAA Journal, Vol. 7, No. 2, pp. 257-263, February 1969.

32. (See corresponding reference number in Section 3.)

Table I. Nominal Specifications for Acoustic Sensors

Dynamic Range -	120 to 160 db depending on the amplifier gain setting
Reference Level -	0.0002 dynes/cm^2
Sample Rate -	125 samples per second
Signal-to-Noise Ratio -	The electrical noise at the output must be at least 30 db below full scale
Frequency Response -	+10 db, -15 db from 30 kHz to 110 kHz +10 db, -20 db from 110 kHz to 200 kHz

Table II. Acoustic Sensor Locations and Saturation Levels

Flight No.	Sensor Channel No.	Station (inch)	Angular* Location (Degrees)	Saturation** Level (db)
1	3	88	101	154.3
1	4	166	110	149.0
1	5	166	290	148.8
2	3	88	101	155.9
2	4	166	110	152.0
2	5	166	290	147.8

* Measured clockwise from the vehicle -Z axis (see Figure 4)

** The saturation level is the rms flat-spectrum random sound pressure level input in db, referenced to 0.0002 dynes/cm^2 that will produce a full scale output of 5.0 volts at the output of the amplifier.

Table III. Pressure Gauge Locations

Flight No.	Radial Distance From Centerline (inch)	Angular* Location (Degrees)
1	13.1	37
2	13.0	130

* Measured clockwise from the -Z axis (see Figure 4)

Table IV. Flight 2 Thermocouple Locations

Thermocouple Number	Axial Station (inch)	Angular Location* (Degrees)
145	31.87	225
146	77.45	225
147	123.53	225
148	169.62	225
149	31.87	315
150	77.45	315
151	123.53	315
152	169.62	315

* Measured clockwise from the vehicle -Z axis (see Figure 4)

Table V. Summary of Acoustic Sensor Errors

Error Source	SPL Error db
Acoustic chamber calibration	±1.5
Amplifier calibration	±0.4
Sensor linearity	±2.0
Microphone calibration	±0.2
Transfer functions in sensor calibration	Negligible
Telemetry and receiving	Negligible(for SPL < 130 db)
Numerical processing	Negligible
Temperature	Not considered in detail but considered negligible**
Total anticipated error (RSS)	±2.5 db

** Heat soak tests of representative sensor systems indicate a maximum variation of up to ±1 db in system response for a maximum temperature variation of ±25 degrees F from the calibration temperature.

Table VI. Error Summary for Base Pressure Gauge

Source	0.01 Psia Range	0.05 Psia Range
Linearity, repeatability, hysterisis	±2% of full scale	±2% of full scale
Zero shift	±1%	±1%
Time response	±1%	±1%
Total	±4% of full scale	±4% of full scale

Table VII. Comparison of Flight 2 rms Surface Pressure Fluctuations at Boundary Layer Transition

	CHANNEL 3 $X = 88''$, $\phi_s = 101°$			CHANNEL 4 $X = 166''$, $\phi_s = 110°$			CHANNEL 5 $X = 166''$, $\phi_s = 290°$		
	ALTITUDE (KM)	θ_{LOCAL} (DEG)	$\tilde{P}/q_c$	ALTITUDE (KM)	θ_{LOCAL} (DEG)	$\tilde{P}/q_c$	ALTITUDE (KM)	θ_{LOCAL} (DEG)	$\tilde{P}/q_c$
TRANSITION ONSET-ACOUSTIC SENSOR	37.8	8.09	3.16×10^{-5}	41.2	7.36	5.41×10^{-5}	41.6	8.19 (8.0)	5.40×10^{-5} (5.47×10^{-5})
TURBULENT BOUNDARY LAYER - ACOUSTIC SENSOR	32.3	8.06	8.91×10^{-4}	37.0	8.43	5.48×10^{-4}	39.1	8.75 (8.0)	6.81×10^{-4} (7.06×10^{-4})

$\tilde{P}/q_c$ = RATIO OF RMS SURFACE PRESSURE FLUCTUATION TO DYNAMIC PRESSURE AT SENSOR

Table VIII. Flight 1 Acoustic Sensor Flow Field Parameters and Pressure Fluctuation Levels

Sensor Channel	Case Number	X_S† (inches)	ψ (deg)	θ_L (deg)	α_T (deg)	M_∞	M_L	Local Reynolds Number Based On: Displacement Thickness, R_δ*	Momentum Thickness, R_θ	Wetted Length, R_x	$\tilde{P}/q_c$	Local B.L.††
3	10	88	0	30.8	22.8	20.55	3.67	463.	172.	4.09×10^5	1.6×10^{-3}	T
3	11	88	0	23.4	15.4	21.38	5.00	1,830.	366.	1.51×10^6	1.2×10^{-3}	T
3	12	88	0	11.3	3.3	21.62	9.83	18,100.	935.	6.59×10^6	0.45×10^{-3}	TR
3	15	88	0	14.1	6.1	21.81	8.15	11,500.	869.	6.33×10^6	0.8×10^{-3}	TR
3	16	88	0	12.0	4.0	20.91	9.29	11,600.	669.	3.49×10^6	1.7×10^{-5}	L
3	9	88	-13.0	28.2	20.7	20.53	4.07	630.	190.	4.72×10^5	1.95×10^{-3}	T
3	13**	88	117.9	2.2	12.3	21.70	18.80	89,800.	1920.	1.12×10^7	3.1×10^{-3}	T
3	14	88	-35.5	19.3	13.9	21.78	6.11	4,490.	618.	3.66×10^6	$>1.3 \times 10^{-3}$	T
4	24	166	0	24.0	16.0	21.38	4.86	2,330.	492.	2.77×10^6	$>1.0 \times 10^{-3}$	T
4	25	166	0	30.8	22.8	20.56	3.67	638.	236.	7.80×10^5	0.45×10^{-3}	TR
4	26	166	0	11.8	3.8	20.93	9.43	15,600.	875.	5.94×10^6	0.25×10^{-3}	TR
4	22	166	62.7	16.8	19.3	20.42	7.04	3,860.	450.	1.60×10^6	2.85×10^{-3}	T
4	23	166	-27.3	25.3	19.5	20.54	4.61	1,270.	305.	1.09×10^6	$>2.4 \times 10^{-3}$	T
5	42	166	43.7	20.2	16.8	20.73	5.86	3,150.	485.	2.27×10^6	$>2.8 \times 10^{-3}$	T
5	43	166	58.6	18.3	19.7	20.80	6.52	4,280.	577.	2.82×10^6	$>2.8 \times 10^{-3}$	T
5	44	166	-34.6	22.1	17.2	21.12	5.33	2,740.	500.	2.62×10^6	$>1.2 \times 10^{-3}$	T
5	45	166	-43.9	21.3	18.4	21.37	5.59	3,140.	532.	2.80×10^6	$>1.2 \times 10^{-3}$	T

†Symbols: X_S = wetted length to sensor, ψ = sensor/windward angle, θ_L = local angle of attack at probe station, α_T = vehicle centerline angle of attack, M_∞ = freestream Mach number, M_L = local Mach number

††Local B.L. = Local Boundary Layer Condition: T = turbulent, TR = transitional, L = laminar

Table IX Electrostatic Probe Boundary Layer Transition Results†

Case Nos. 1-82 Measurements on Windward Ray (See Section 4.3.3.1):

Case No.	X_S †† (inches)	ϕ_S (deg)	ψ (deg)	θ_L (deg)	α_T (deg)	M_∞	Local B.L.†††	Re_δ*††††	M_L ††††
1a-1b	32.75	0					ND		
1c	32.75	0	+5.0		25.45	20.75	ND at +5° L at +7°		
2a	32.75	0	0	19.63	11.63	20.40	L	1.009[3]	5.96
2b	32.75	0	-5.0		12.80	20.87	L		
2c	32.75	0	+5.0		10.60	20.40	L		
3a	32.75	0	0	12.97	4.97	20.48	L	4.022[3]	8.73
3b	32.75	0	-5.0		4.80	20.48	L		
3c	32.75	0	+5.0		5.17	20.50	L		
4a-5c	32.75	0					CAL		
6a	32.75	0	0	21.50	13.50	21.58	L	1.663[3]	5.46
6b	32.75	0	-5.0		15.20	21.56	L		
6c	32.75	0	+5.0		12.10	21.55	L		
7a	32.75	0	0	11.90	3.90	21.76	L	1.066[4]	9.49
7b	32.75	0	-5.0		3.70	21.70	L		
7c	32.75	0	+5.0		4.20	21.70	L		
8a	32.75	0	0	10.90	2.90	22.00	L	1.555[4]	10.22
8b	32.75	0	-5.0		3.10	21.96	L		
8c	32.75	0	+5.0		2.80	21.96	L		
9a	32.75	0	0	17.64	9.64	22.20	L	4.724[3]	6.67
9b	32.75	0	-5.0		10.14	22.25	L		
9c	32.75	0	+5.0		8.87	22.27	L		

†Tables III through VI of Reference 3 give these results together with associated vehicle velocities, altitudes and freestream densities, temperatures, pressures and viscosities.

††Symbols: X_S, ψ, θ_L, α_T, M_∞, Re_δ* and M_L as defined in Table VIII.
ϕ_S = sensor azimuth angle.

†††Local B.L. = local boundary layer condition: T = turbulent, L = laminar, LT = fluctuations of order ±1 pcm step size, may be just at threshold of transition detection by probe, ND = no probe data, may be just at threshold of amplifier range, CAL = no boundary layer data due to calibration sweep measurement.

††††Calculated only for ψ = 0 cases.

Table IX (continued)

Case No.	X_s (inches)	ϕ_s (deg)	ψ (deg)	θ_L (deg)	α_T (deg)	M_∞	Local B.L.	$Re_\delta{}^*$	M_L
10a-10c	47.5	0					ND		
11a	47.5	0	0	19.63	11.63	20.40	L	1.218^3	5.96
11b	47.5	0	-5.0		12.80	20.87	L		
11c	47.5	0	+5.0		10.60	20.40	L		
12a	47.5	0	0	12.97	4.97	20.48	L	4.861^3	8.73
12b	47.5	0	-5.0		4.80	20.48	L		
12c	47.5	0	+5.0		5.17	20.50	L		
13a-14c	47.5	0					CAL		
15a-15b	47.5	0					ND		
15c	47.5	0	+5.0		12.10	21.55	L		
16a	47.5	0	0	11.90	3.90	21.76	L	1.288^4	9.49
16b	47.5	0	-5.0		3.70	21.70	L		
16c	47.5	0	+5.0		4.20	21.70	L		
17a	47.5	0	0	10.90	2.90	22.00	L	1.881^4	10.22
17b	47.5	0	-5.0		3.10	21.96	L		
17c	47.5	0	+5.0		2.80	21.96	LT		
18a	47.5	0	0	17.64	9.64	22.20	LT	5.705^3	6.67
18b	47.5	0	-5.0		10.14	22.25	T		
18c	47.5	0	+5.0		8.87	22.27	T		
19a	88.0	0	0	35.00	27.00	20.57	L	1.632^2	3.14
19b-19c	88.0	0					ND		
20a	88.0	0	0	19.63	11.63	20.40	L	1.658^3	5.96
20b	88.0	0	-5.0		12.80	20.87	L		
20c	88.0	0	+5.0		10.60	20.40	L		
21a	88.0	0	0	12.97	4.97	20.48	L	6.618^3	8.73
21b	88.0	0	-5.0		4.80	20.48	L		
21c	88.0	0	+5.0		5.17	20.50	L		
22a-23c	88.0	0					CAL		
24a-24b	88.0	0					ND		
24c	88.0	0	+5.0		12.10	21.55	L		
25a	88.0	0	0	11.90	3.90	21.76	L	1.755^4	9.49
25b	88.0	0	-5.0		3.70	21.70	L		

Table IX (continued)

Case No.	X_s (inches)	ϕ_s (deg)	ψ (deg)	θ_L (deg)	α_T (deg)	M_∞	Local B.L.	$Re_\delta{}^*$	M_L
25c	88.0	0	+5.0		4.20	21.70	T		
26a	88.0	0	0	10.90	2.90	22.00	T	2.563^4	10.22
26b	88.0	0	-5.0		3.10	21.96	T		
26b	88.0	0	+5.0		2.80	21.96	T		
27a-27b	88.0	0					ND		
27c	88.0	0	+5.0		8.87	22.27	LT		
28a	32.75	180	0	21.81	13.81	23.70	L	2.178^2	5.42
28b	32.75	180	-5.0		13.18	23.70	L		
28c	32.75	180	+5.0		14.52	23.63	L		
29a-29c	32.75	180					ND		
30a	32.75	180	0	14.82	6.82	21.00	L	1.517^3	7.80
30b	32.75	180	-5.0		6.81	20.86	L		
30c	32.75	180	+5.0		6.87	20.90	L		
31a	32.75	180	0	14.78	6.78	20.42	L	1.968^3	7.79
31b	32.75	180	-5.0		6.48	20.40	L		
31c	32.75	180	+5.0		7.14	20.45	L		
32a-32c	32.75	180					CAL		
33a	32.75	180	0	15.60	7.60	20.61	L	2.750^3	7.44
33b	32.75	180	-5.0		8.25	20.63	L		
33c	32.75	180	+5.0		7.10	20.61	L		
34a	32.75	180	0	14.05	6.05	20.91	L	4.471^3	8.18
34b	32.75	180	-5.0		5.50	20.95	L		
34c	32.75	180	+5.0		6.75	20.92	L		
35a	32.75	180	0	12.16	4.16	21.45	L	8.150^3	9.30
35b	32.75	180	-5.0		4.50	21.45	L		
35c	32.75	180	+5.0		3.90	21.43	L		
36a	32.75	180	0	16.98	8.98	21.65	L	3.762^3	6.90
36b	32.75	180	-5.0		8.00	21.66	L		
36c	32.75	180					ND		
37a	32.75	180	0	10.57	2.57	21.89	L	1.547^4	10.47
37b	32.75	180	-5.0		2.55	21.90	L		
37c	32.75	180	+5.0		2.62	21.89	L		

Table IX (continued)

Case No.	X_s (inches)	ϕ_s (deg)	ψ (deg)	θ_L (deg)	α_T (deg)	M_∞	Local B.L.	$Re_\delta{}^*$	M_L
38a	32.75	180	0	13.25	5.25	22.10	L	1.020^4	8.69
38b	32.75	180	-5.0		5.95	22.10	L		
38c	32.75	180	+5.0		4.75	22.10	L		
39a-39b	67.0	180					ND		
39c	67.0	180	+5.0		14.52	23.63	L		
40a-40c	67.0	180					ND		
41a	67.0	180	0	14.82	6.82	21.00	L	2.173^3	7.80
41b	67.0	180	-5.0		6.81	20.86	L		
41c	67.0	180	+5.0		6.87	20.90	L		
42a-42c	67.0	180					ND		
43a-43c	67.0	180					CAL		
44a	67.0	180	0	15.60	7.60	20.61	L	3.930^3	7.44
44b	67.0	180	-5.0		8.25	20.63	L		
44c	67.0	180	+5.0		7.10	20.61	L		
45a	67.0	180	0	14.05	6.05	20.91	L	6.404^3	8.18
45b	67.0	180	-5.0		5.50	20.95	L		
45c	67.0	180	+5.0		6.75	20.92	L		
46a	67.0	180	0	12.16	4.16	21.45	L	1.169^4	9.30
46b	67.0	180	-5.0		4.50	21.45	L		
46c	67.0	180	+5.0		3.90	21.43	L		
47a	67.0	180					ND		
47b	67.0	180	-5.0		8.00	21.66	L		
47c	67.0	180					ND		
48a	67.0	180	0	10.57	2.57	21.89	L	2.221^4	10.47
48b	67.0	180	-5.0		2.55	21.90	L		
48c	67.0	180	+5.0		2.62	21.89	L		
49a	67.0	180	0	13.25	5.25	22.10	LT	1.461^4	8.69
49b	67.0	180	-5.0		5.95	22.10	LT		
49c	67.0	180	+5.0		4.75	22.10	LT		
50a	139.0	180	0	21.81	13.81	23.70	L	4.492^2	5.42
50b	139.0	180	-5.0		13.18	23.70	L		
50c	139.0	180	+5.0		14.52	23.63	L		

Table IX (continued)

Case No.	X_s (inches)	ϕ_s (deg)	ψ (deg)	θ_L (deg)	α_T (deg)	M_∞	Local B.L.	$Re_\delta{}^*$	M_L
51a-51c	139.0	180					ND		
52a	139.0	180	0	14.82	6.82	21.00	L	3.132^3	7.80
52b	139.0	180	-5.0		6.81	20.86	L		
52c	139.0	180	+5.0		6.87	20.90	L		
53a	139.0	180	0	14.78	6.78	20.42	L	4.063^3	7.79
53b	139.0	180	-5.0		6.48	20.40	L		
53c	139.0	180	+5.0		7.14	20.45	L		
54a-54c	139.0	180					CAL		
55a	139.0	180	0	15.60	7.60	20.61	L	5.670^3	7.44
55b	139.0	180	-5.0		8.25	20.63	L		
55c	139.0	180	+5.0		7.10	20.61	L		
56a	139.0	180	0	14.05	6.05	20.91	L	9.231^3	8.18
56b	139.0	180	-5.0		5.50	20.95	L		
56c	139.0	180	+5.0		6.75	20.92	L		
57a	139.0	180	0	12.16	4.16	21.45	L	1.685^4	9.30
57b	139.0	180	-5.0		4.50	21.45	L		
57c	139.0	180	+5.0		3.90	21.43	L		
58a-58c	139.0	180					ND		
59a	139.0	180	0	10.57	2.57	21.89	T	3.204^4	10.47
59b	139.0	180	-5.0		2.55	21.90	T		
59c	139.0	180	+5.0		2.62	21.89	T		
60a	139.0	180	0	13.25	5.25	22.10	LT	2.107^4	8.69
60b	139.0	180	-5.0		5.95	22.10	LT		
60c	139.0	180	+5.0		4.75	22.10	LT		
61a	166.0	180	0	21.81	13.81	23.70	L	4.911^2	5.42
61b	166.0	180	-5.0		13.18	23.70	L		
61c	166.0	180	+5.0		14.52	23.63	L		
62a-62c	166.0	180					ND		
63a	166.0	180	0	14.82	6.82	21.00	L	3.424^3	7.80
63b	166.0	180	-5.0		6.81	20.86	L		
63c	166.0	180	+5.0		6.87	20.90	L		
64a	166.0	180	0	14.78	6.78	20.42	L	4.442^3	7.79

Table IX (continued)

Case No.	X_s (inches)	ϕ_s (deg)	ψ (deg)	θ_L (deg)	α_T (deg)	M_∞	Local B.L.	$Re_\delta{}^*$	M_L
64b	166.0	180	-5.0		6.48	20.40	L		
64c	166.0	180					ND		
65a-65c	166.0	180					CAL		
66a	166.0	180	0	15.60	7.60	20.61	L	6.200[3]	7.44
66b	166.0	180	-5.0		8.25	20.63	L		
66c	166.0	180	+5.0		7.10	20.61	L		
67a	166.0	180	0	14.05	6.05	20.91	L	1.009[4]	8.18
67b	166.0	180	-5.0		5.50	20.95	L		
67c	166.0	180	+5.0		6.75	20.92	L		
68a	166.0	180	0	12.16	4.16	21.45	L	1.842[4]	9.30
68b	166.0	180	-5.0		4.50	21.45	L		
68c	166.0	180	+5.0		3.90	21.43	L		
69a-69c	166.0	180					ND		
70a	166.0	180	0	10.57	2.57	21.89	T	3.503[4]	10.47
70b	166.0	180	-5.0		2.55	21.90	T		
70c	166.0	180	+5.0		2.62	21.89	T		
71a	166.0	180	0	13.25	5.25	22.10	T	2.303[4]	8.69
71b	166.0	180	-5.0		5.95	22.10	T		
71c	166.0	180	+5.0		4.75	22.10	LT		
72a-75c	166.0	150					ND		
76a	166.0	150	0	20.88	12.88	20.41	L	1.963[3]	5.60
76b	166.0	150					ND		
76c	166.0	150	+5.0		14.15	20.40	L		
77a	166.0	150	0	21.40	13.40	20.60	ND at 0° L at -2°	2.393[3]	5.47
77b	166.0	150	-5.0		15.00	20.60	L		
77c	166.0	150	+5.0		11.97	20.60	ND at +5° L at +6°		
78a	166.0	150	0	12.08	4.08	20.90	L	1.485[4]	9.30
78b	166.0	150	-5.0		3.96	20.95	L		
78c	166.0	150					ND		
79a	166.0	150	0	15.99	7.99	21.43	T	8.634[3]	7.30
79b	166.0	150	-5.0		9.17	21.40	T		
79c	166.0	150	+5.0		6.90	21.40	T		

Table IX (continued)

Case No.	X_s (inches)	ϕ_s (deg)	ψ (deg)	θ_L (deg)	α_T (deg)	M_∞	Local B.L.	$Re_\delta{}^*$	M_L
80a	166.0	150					ND		
80b	166.0	150	-5.0		4.42	21.63	T		
80c	166.0	150					ND		
81a	166.0	150	0	10.74	2.74	21.88	T	3.365[4]	10.34
81b	166.0	150	-5.0		2.84	21.85	T		
81c	166.0	150	+5.0		2.66	21.85	T		
82a	166.0	150	0	19.16	11.16	22.08	ND at 0° L at -3°	7.655[3]	6.15
82b	166.0	150	-5.0		11.60	22.05	T		
82c	166.0	150	+5.0		10.40	22.10	ND at +5° T at +7°		

(Case Nos. 83-152 Measurements off Windward Ray--Type a (See Section 4.3.3.2):

83	32.75	180	-30.09	19.55	13.45	20.6	LT
84	32.75	180	-25.42	18.84	12.06	20.6	LT
85	32.75	180	-19.68	8.06	10.71	20.6	LT
86	32.75	180	-12.77	17.19	9.43	20.6	LT
87	47.5	0	-76.22	8.78	3.33	22.16	T
88	47.5	0	-45.36	11.20	4.57	22.16	T
89	47.5	0	-27.72	14.89	7.80	22.00	T
90	47.5	0	-21.04	16.34	8.95	22.00	T
91	47.5	0	-15.73	17.50	9.88	22.00	LT
92	67.0	180	63.25	14.44	14.94	20.45	L
93	67.0	180	68.34	12.78	13.61	20.49	L
94	67.0	180	73.19	11.35	12.25	20.50	LT
95	67.0	180	-30.09	19.55	13.45	20.61	LT
96	67.0	180	-25.42	18.84	12.06	20.62	T
97	67.0	180	-19.68	18.06	10.71	20.62	T
98	67.0	180	-12.77	17.19	9.43	20.63	LT
99	67.0	180	-70.99	9.25	3.90	20.93	L
100	67.0	180	-38.36	11.05	3.90	20.95	L
101	67.0	180	-72.39	8.98	3.29	21.66	L

Table IX (continued)

Case No.	X_s (inches)	ϕ_s (deg)	ψ (deg)	θ_L (deg)	α_T (deg)	M_∞	Local B.L.
102	67.0	180	-83.12	8.78	7.04	21.89	LT
103	67.0	180	-57.56	9.99	3.73	21.90	LT
104	67.0	180	-24.77	10.41	2.66	21.91	T
105	67.0	180	20.50	10.61	2.78	21.92	LT
106	67.0	180	51.60	10.42	3.92	21.92	LT
107	67.0	180	68.20	10.05	5.61	21.93	T
108	67.0	180	79.07	9.33	7.37	21.93	T
109	67.0	180	88.35	8.16	9.09	21.94	LT
110	67.0	180	-65.80	10.62	6.51	22.05	T
111	67.0	180	-59.44	12.05	8.10	22.06	T
112	67.0	180	-52.95	13.49	9.48	22.07	T
113	67.0	180	-41.27	16.74	11.76	21.00	T
114	67.0	180	-37.35	17.26	11.76	21.01	T
115	67.0	180	-32.33	17.56	11.39	21.02	T
116	67.0	180	-21.98	16.95	9.68	21.03	T
117	67.0	180	-16.85	15.92	8.28	21.03	T
118	67.0	180	- 9.08	14.53	6.62	21.04	T
119	88.0	0	-34.49	19.82	14.49	20.70	T
120	88.0	0	- 9.39	23.65	15.88	21.58	T
121	88.0	0	- 5.49	23.28	15.35	21.59	T
122	88.0	0	43.65	14.88	9.61	21.80	T
123	88.0	0	48.66	15.10	10.91	21.81	T
124	88.0	0	53.15	15.12	12.13	21.81	LT
125	88.0	0	81.64	9.54	11.87	21.87	T
126	88.0	0	86.53	8.50	10.43	21.87	LT
127	88.0	0	-43.10	12.75	6.55	22.02	T
128	88.0	0	-31.48	12.08	4.80	22.03	T
129	88.0	0	- 8.96	11.12	3.16	22.04	T
130	88.0	0	37.60	9.94	2.45	22.05	T
131	139.0	180	-38.49	15.80	10.05	21.44	T
132	139.0	180	-32.20	15.16	8.50	21.44	L
133	139.0	180	44.87	10.20	3.12	21.45	T

Table IX (continued)

Case No.	X_s (inches)	ϕ_s (deg)	ψ (deg)	θ_L (deg)	α_T (deg)	M_∞	Local B.L.
134	139.0	180	82.72	8.44	3.61	21.45	T
135	166.0	180	23.74	17.83	10.78	21.00	LT
136	166.0	180	33.04	19.19	13.47	21.00	LT
137	166.0	180	56.00	18.20	19.10	21.07	L
138	166.0	180	56.90	17.96	19.10	21.10	T
139	166.0	180	59.30	17.22	18.98	21.11	T
140	166.0	180	-75.64	11.57	15.74	21.36	T
141	166.0	180	-72.08	12.58	16.03	21.37	T
142	166.0	180	-68.47	13.50	15.92	21.38	T
143	166.0	180	-56.53	15.93	14.85	21.40	T
144	166.0	180	-52.48	16.32	14.01	21.40	T
145	166.0	150	-84.13	8.56	5.96	20.40	T
146	166.0	150	-66.06	10.40	6.01	20.40	T
147	166.0	150	-62.18	13.83	12.93	21.33	T
148	166.0	150	-57.63	15.19	13.85	21.33	T
149	166.0	150	-53.22	16.56	14.69	21.34	T
150	166.0	150	-38.47	20.27	15.92	21.38	T
151	166.0	150	-26.53	21.20	14.85	21.40	T
152	166.0	150	-22.48	20.89	14.01	21.40	T
Case Nos. 153-175 Measurements off Windward Ray--Type b (See Section 4.3.3.2):							
153a	32.75	0	-26.41	36.35	32.40	24.44	L
153b	47.5	0	-26.41	36.35	32.40	24.44	L
153c	88.0	0	-26.41	36.35	32.40	24.44	L
154a-154b							ND
154c	88.0	0	24.87	37.86	33.66	22.48	L
155a	32.75	0	29.20	33.73	30.21	21.30	L
155b	47.5	0	29.20	33.73	30.21	21.30	L
155c	88.0	0	29.20	33.73	30.21	21.30	L
156a	32.75	0	25.05	25.06	18.99	20.51	L
156b	47.5	0	25.05	25.06	18.99	20.51	L
156c	88.0	0	25.05	25.06	18.99	20.51	L

Table IX (continued)

Case No.	X_s (inches)	ϕ_s (deg)	ψ (deg)	θ_L (deg)	α_T (deg)	M_∞	Local B.L.
157a	32.75	0	47.45	14.34	9.49	20.50	L
157b	47.5	0	47.45	14.34	9.49	20.50	L
157c	88.0	0	47.45	14.34	9.49	20.50	L
158a	32.75	0	26.04	19.54	12.91	20.84	L
158b	47.5	0	26.04	19.54	12.91	20.84	L
158c	88.0	0	26.04	19.54	12.91	20.84	L
159a	32.75	0	87.82	8.28	12.93	21.32	L
159b	47.5	0	87.82	8.28	12.93	21.32	L
159c	88.0	0	87.82	8.28	12.93	21.32	L
160a	32.75	0	-16.68	23.91	16.66	21.56	L
160b	47.5	0	-16.68	23.91	16.66	21.56	L
160c	88.0	0					ND
161a	32.75	0	53.15	15.12	12.13	21.81	L
161b	47.5	0	53.15	15.12	12.13	21.81	L
161c	88.0	0	53.15	15.12	12.13	21.81	T
162a	32.75	0	-56.27	13.18	9.50	22.35	L
162b	47.5	0	-56.27	13.18	9.50	22.35	L
162c	88.0	0	-56.27	13.18	9.50	22.35	T
163a	32.75	180	41.33	39.85	47.30	25.40	L
163b	67.0	180	41.33	39.85	47.30	25.40	L
163c	139.0	180	41.33	39.85	47.30	25.40	L
163d	166.0	180	41.33	39.85	47.30	25.40	L
164a	32.75	180	31.53	24.73	19.91	23.35	L
164b	67.0	180	31.53	24.73	19.91	23.35	L
164c	139.0	180	31.53	24.73	19.91	23.35	L
164d	166.0	180	31.53	24.73	19.91	23.35	L
165a	32.75	180	44.74	18.69	15.36	20.40	L
165b	67.0	180	44.74	18.69	15.36	20.40	L
165c	139.0	180	44.74	18.69	15.36	20.40	L
165d	166.0	180	44.74	18.69	15.36	20.40	L
166a	32.75	180	55.34	17.41	17.16	20.45	L
166b	67.0	180	55.34	17.41	17.16	20.45	L

Table IX (continued)

Case No.	X_S (inches)	ϕ_S (deg)	ψ (deg)	θ_L (deg)	α_T (deg)	M_∞	Local B.L.
166c	139.0	180	55.34	17.41	17.16	20.45	L
166d	166.0	180	55.34	17.41	17.16	20.45	L
167a	32.75	180	-38.93	20.20	15.94	20.60	L
167b	67.0	180	-38.93	20.20	15.94	20.60	L
167c	139.0	180	-38.93	20.20	15.94	20.60	L
167d	166.0	180	-38.93	20.20	15.94	20.60	L
168a	32.75	180	-48.48	16.38	12.88	21.40	L
168b	67.0	180	-48.48	16.38	12.88	21.40	L
168c	139.0	180	-48.48	16.38	12.88	21.40	LT
168d	166.0	180	-48.48	16.38	12.88	21.40	T
169	166.0	150	10.45	43.24	36.01	25.40	L
170	166.0	150	32.84	26.09	21.92	20.42	L
171	166.0	150	-28.96	26.77	21.75	20.56	L
172	166.0	150	53.74	14.26	10.78	21.00	L
173	166.0	150	-26.53	21.20	14.85	21.40	T
174	166.0	150	44.32	16.51	12.07	21.69	T
175	166.0	150	-63.47	12.53	10.43	22.25	T

Figure 1

Flight 1 Vehicle Total Angle-of-Attack History

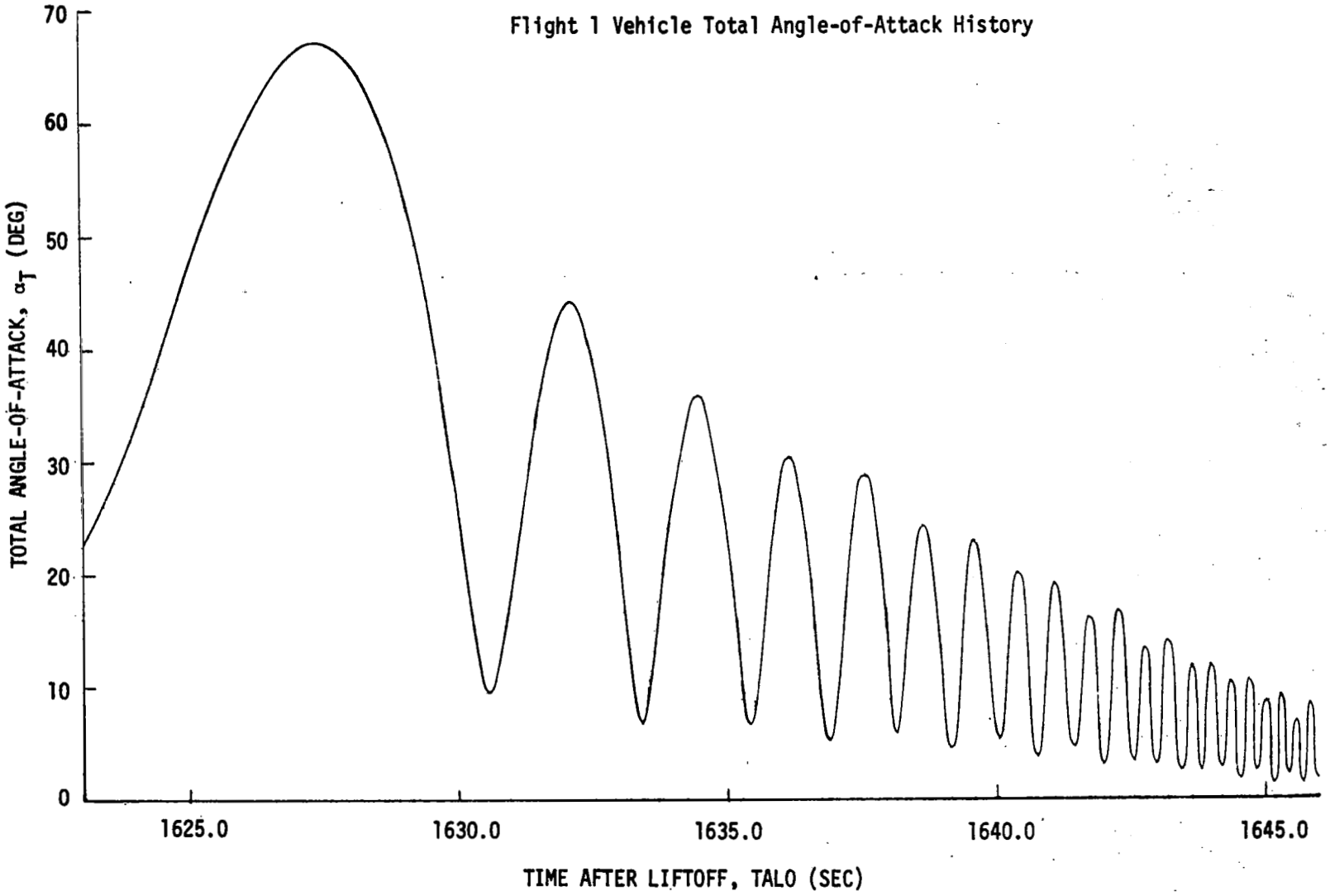

Figure 2a. Flight 1 Vehicle Polar Angle-of-Attack History

(1623.0 < TALO < 1637.0)

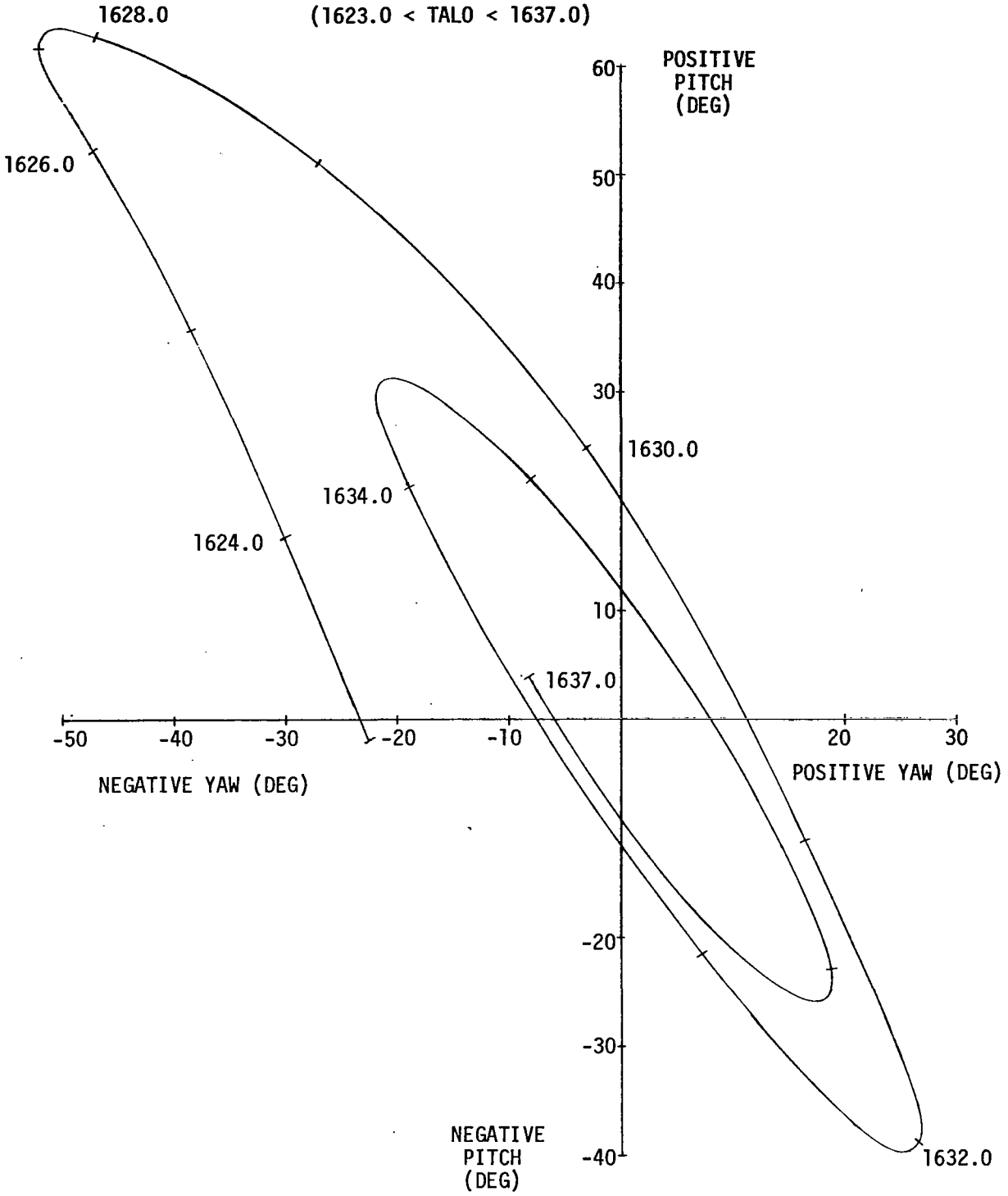

Figure 2b. Flight 1 Vehicle Polar Angle-of-Attack History
(1637.0 < TALO < 1644.0)

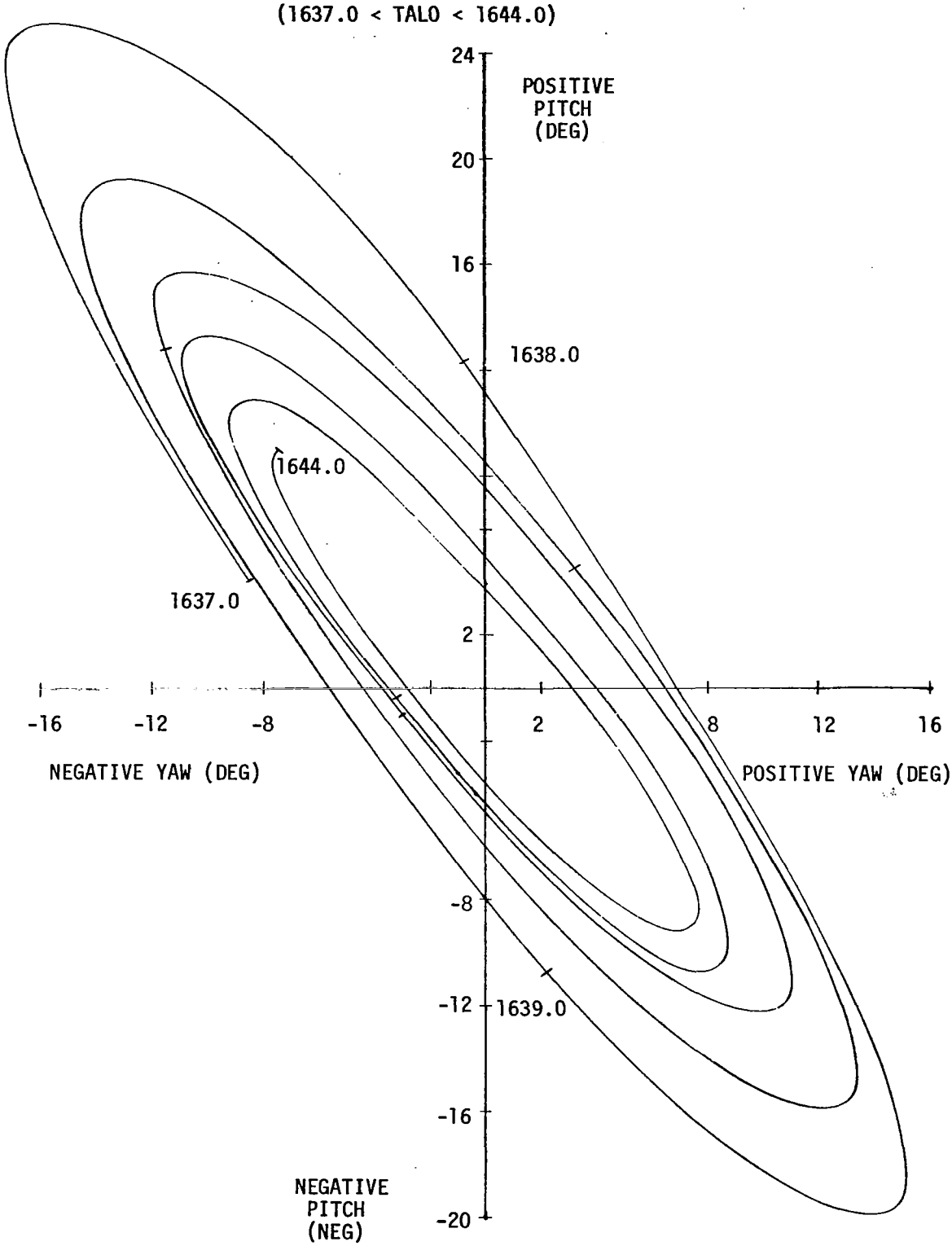

Figure 3. Flight 1 Vehicle Roll Attitude History

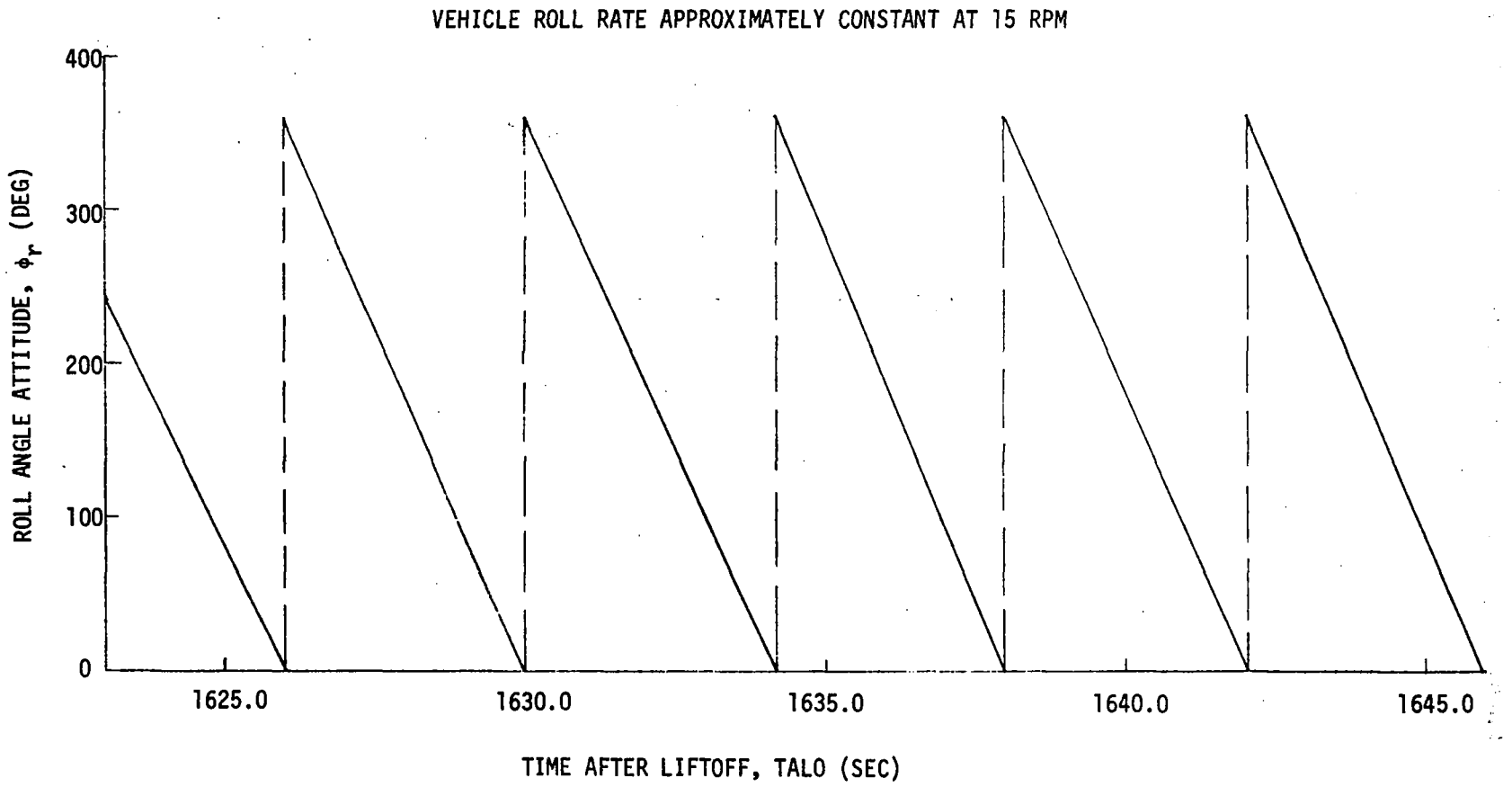

Figure 4. Definition of Vehicle Attitude Angles

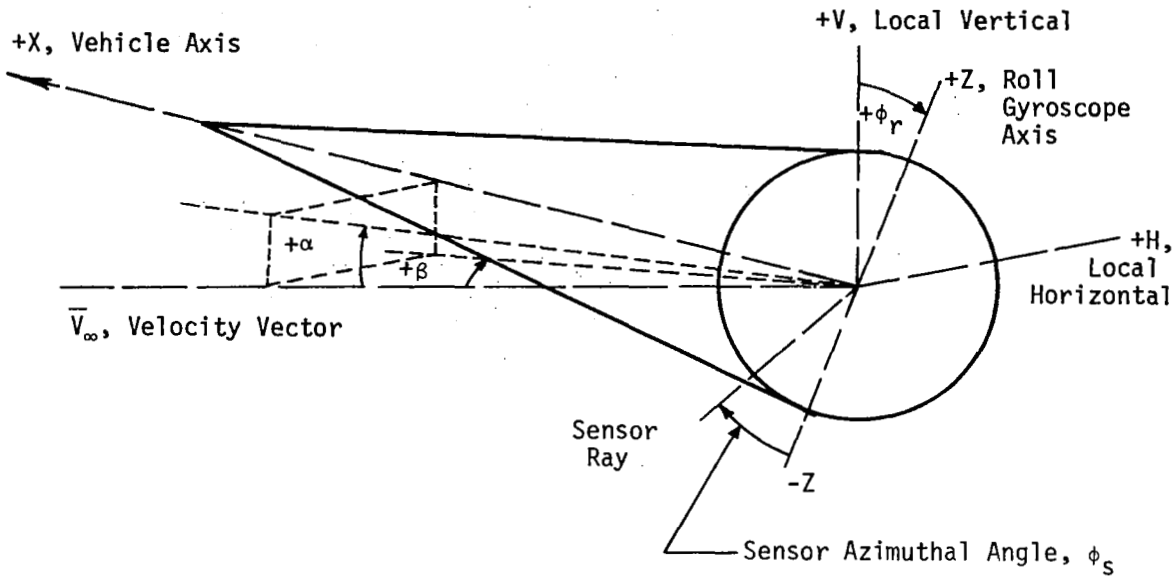

Pitch angle-of-attack, α

This is defined as the angle between the vehicle velocity vector and the vehicle axis, projected to lie in the plane of the trajectory. Vehicle nose pitch up is positive

Yaw angle-of-attack, β

This is defined as the angle between the plane of the trajectory and the vehicle axis projected to lie in the plane formed by the vehicle velocity vector and the local horizontal. Vehicle nose yaw to the right of the trajectory as seen from the rear of the vehicle is positive.

Roll attitude angle, ϕ_r

This is defined as the angle of the roll attitude gyroscope. The roll attitude is zero when the +Z axis of the vehicle lies in the plane of the trajectory and points upward. The roll attitude angle is positive when the vehicle rotates clockwise, as seen from the rear of the vehicle.

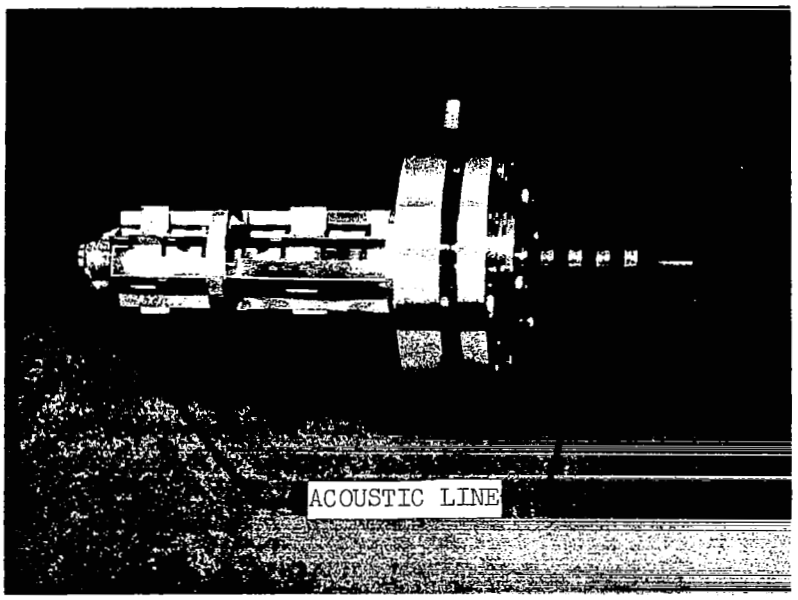

Figure 5. Acoustic Line for Beryllium Sensor

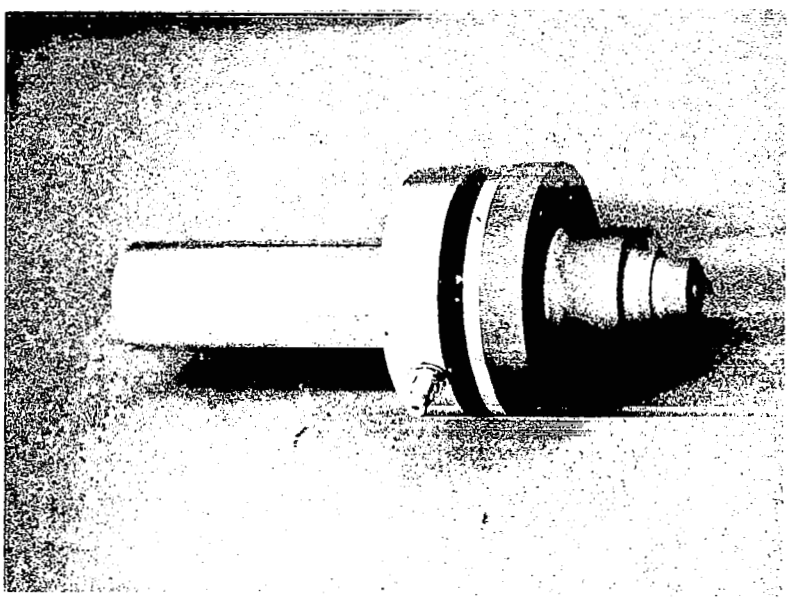

Figure 6. Packaged Beryllium Acoustic Sensor

Figure 7. Acoustic Sensor Locations

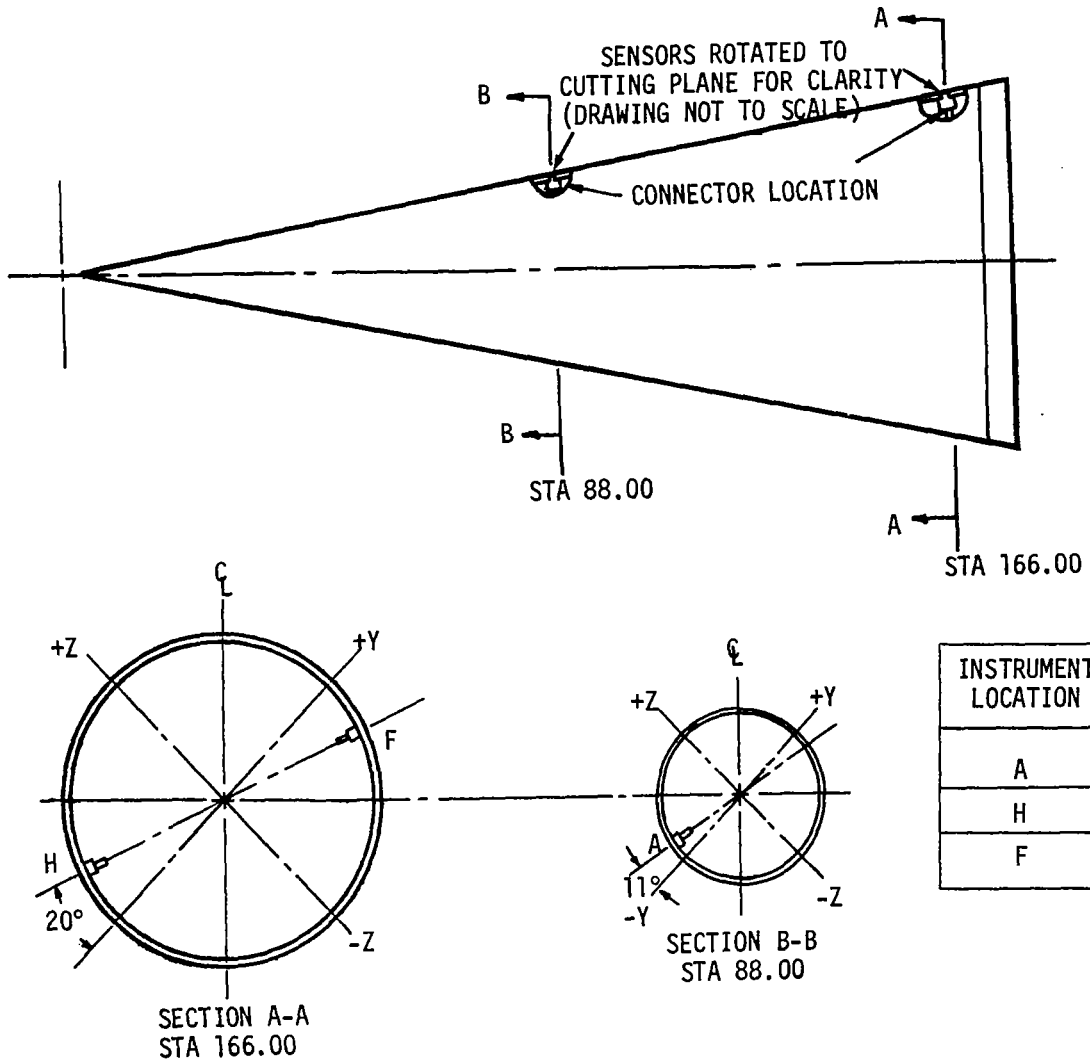

INSTRUMENT LOCATION	CHANNEL NUMBER
A	3
H	4
F	5

Figure 8. Pressure Gauge Block Diagram

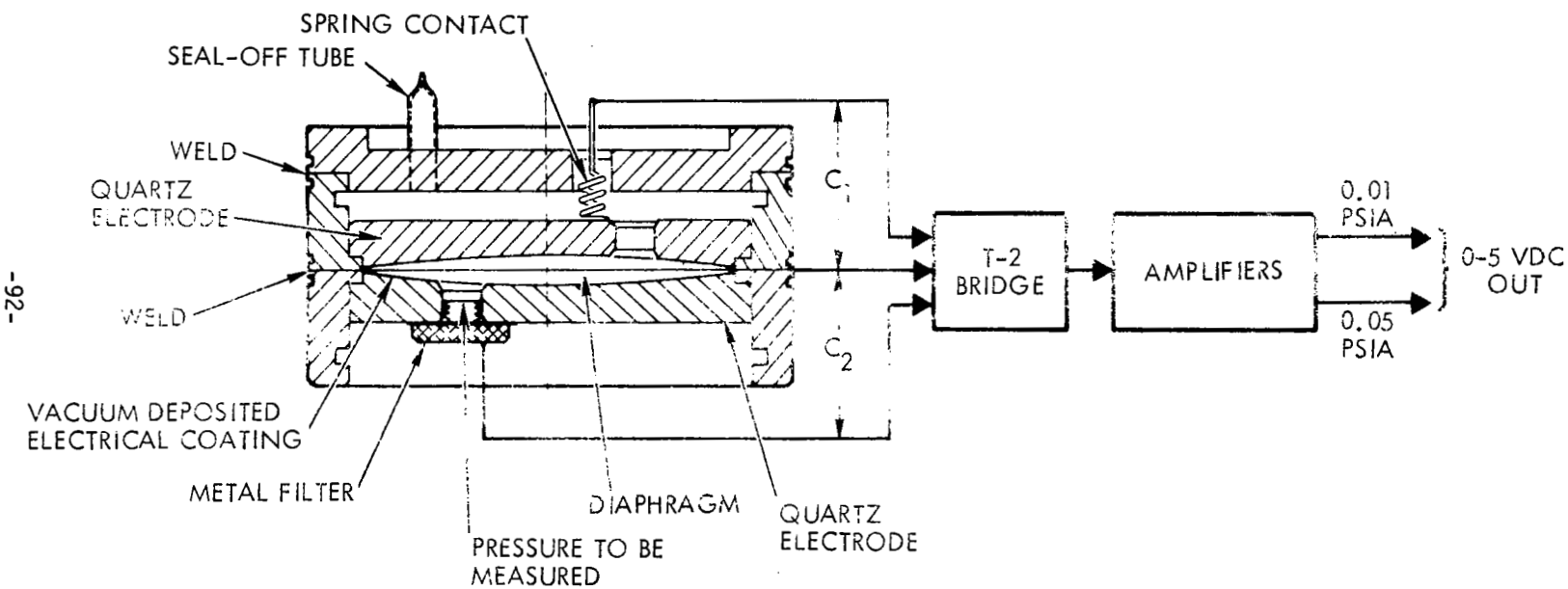

ISODYNAMIC PRESSURE CAPSULE

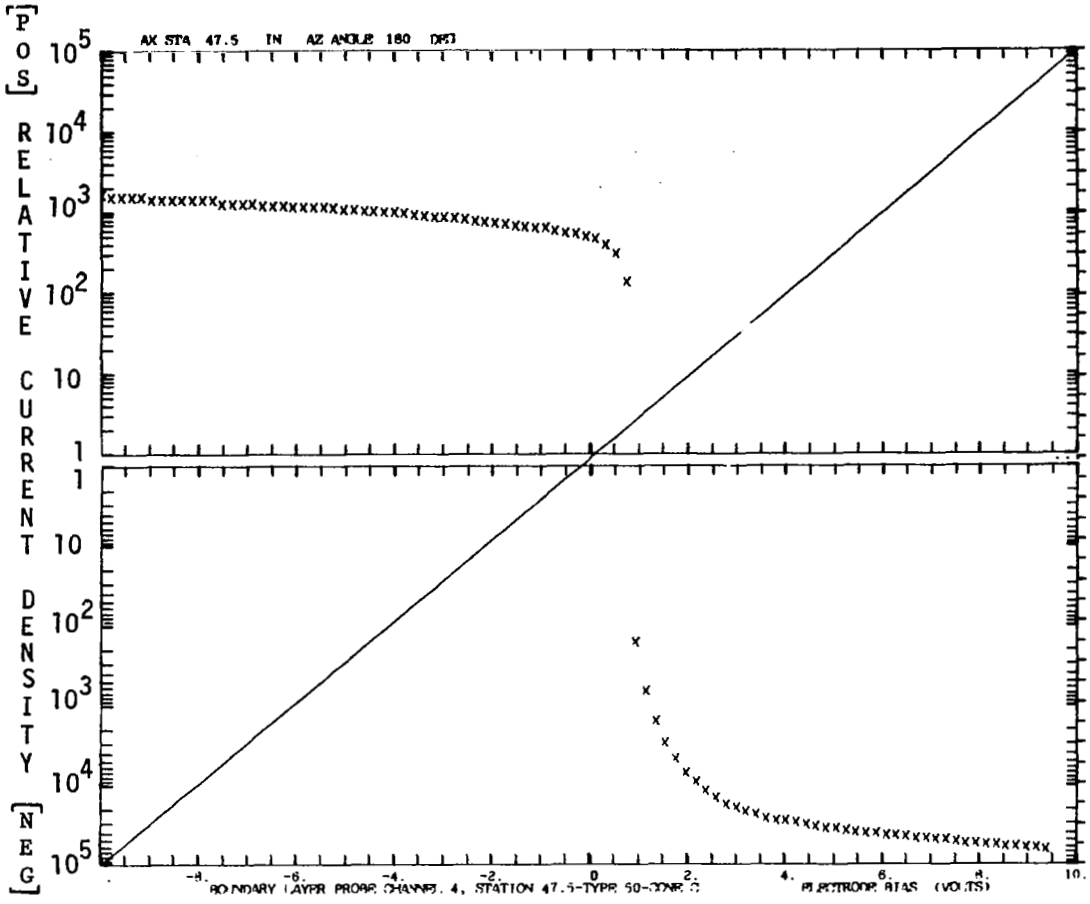

Figure 9. Example of Electrostatic Probe Current-Voltage Characteristic Measured under Laminar Flow Conditions--Flight 2

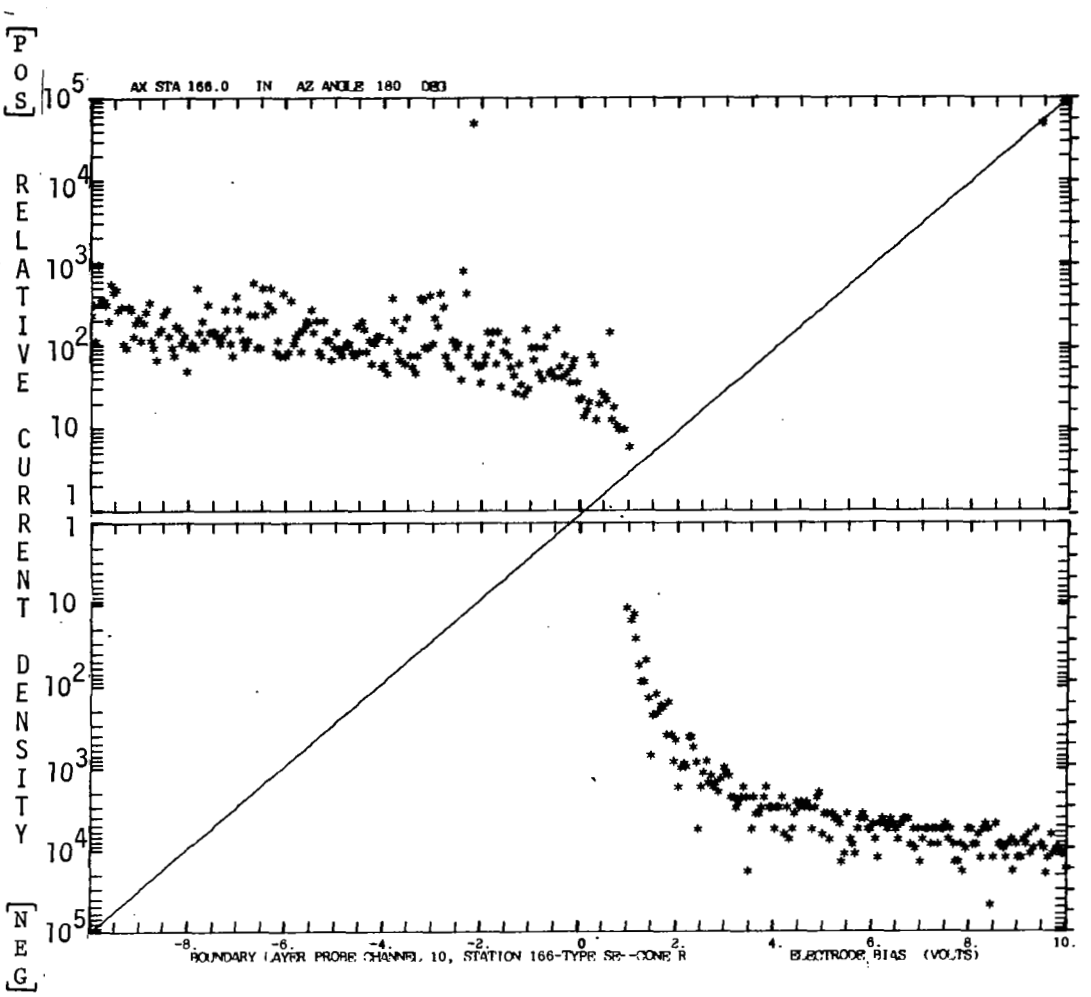

Figure 10. Example of Electrostatic Probe Current-Voltage Characteristic Measured under Laminar Flow Conditions--Flight 2

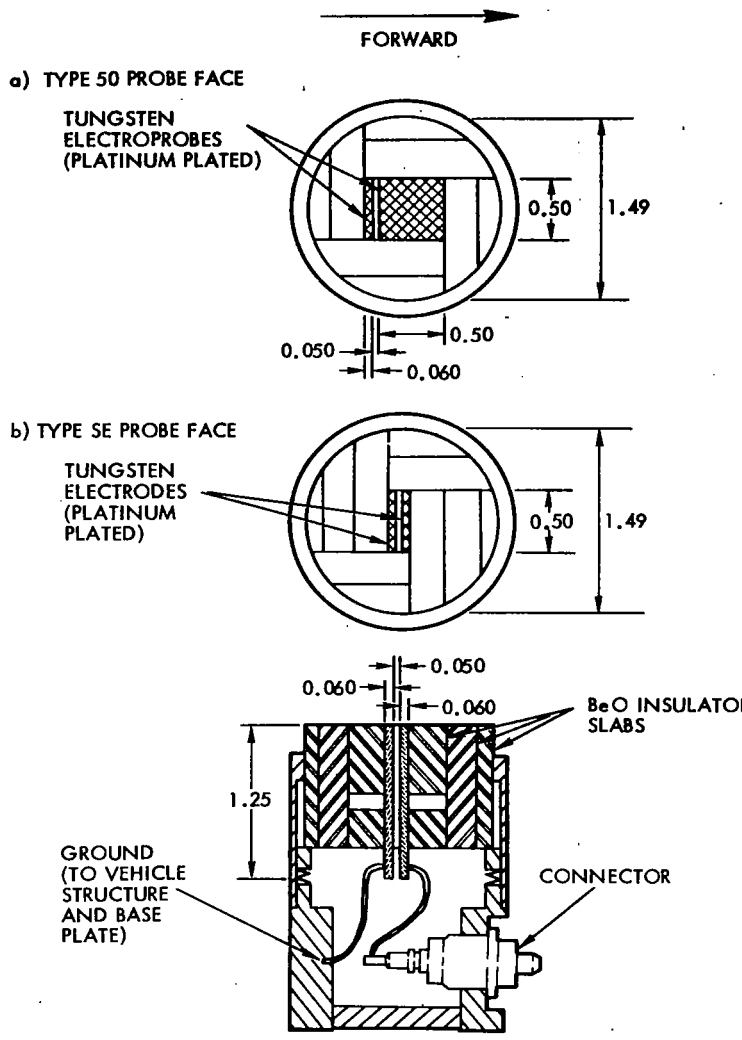

Figure 11. Schematic of Electrostatic Probe Designs

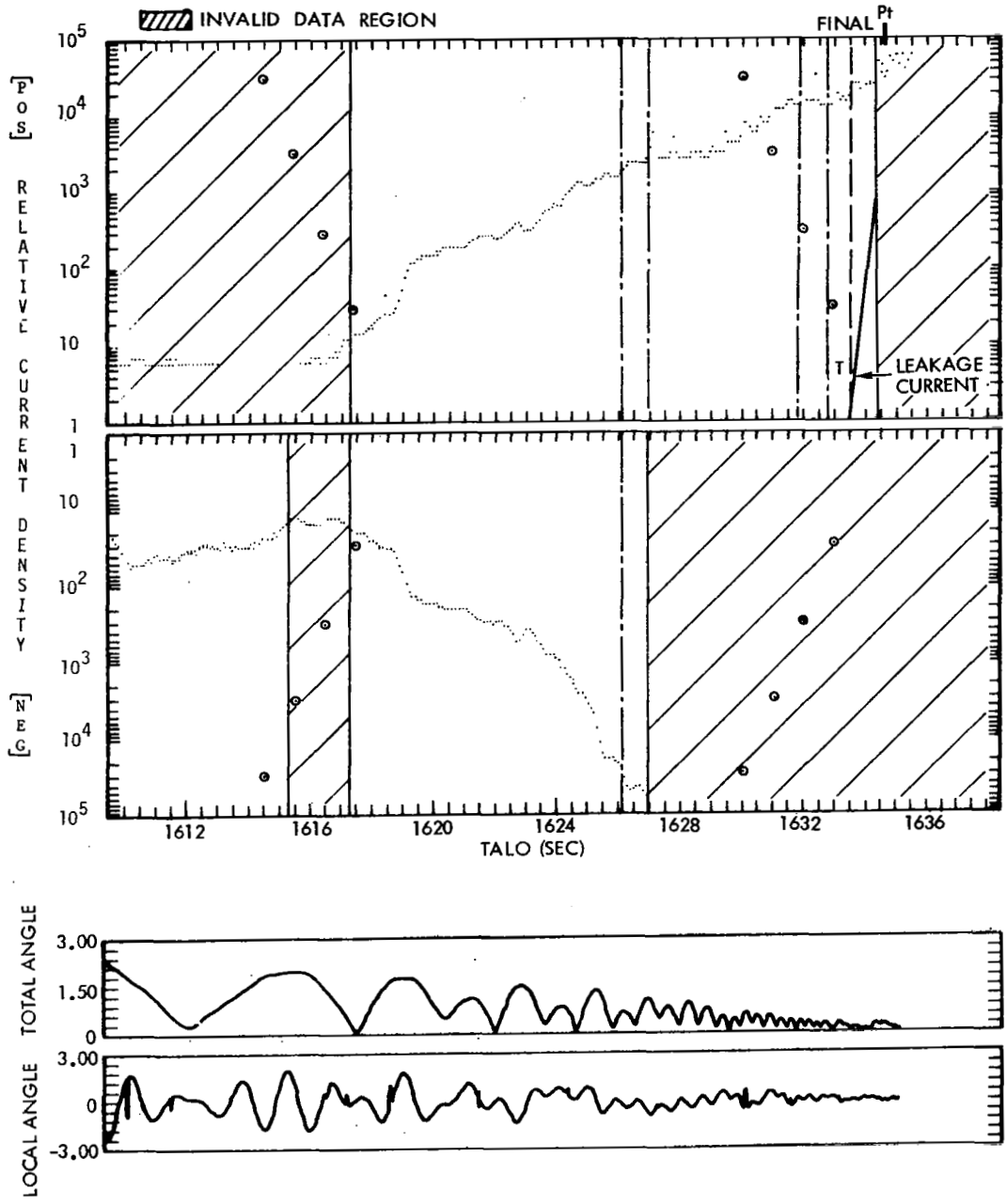

Figure 12. Example of Electrostatic Probe Saturation Current Density History--Flight 2

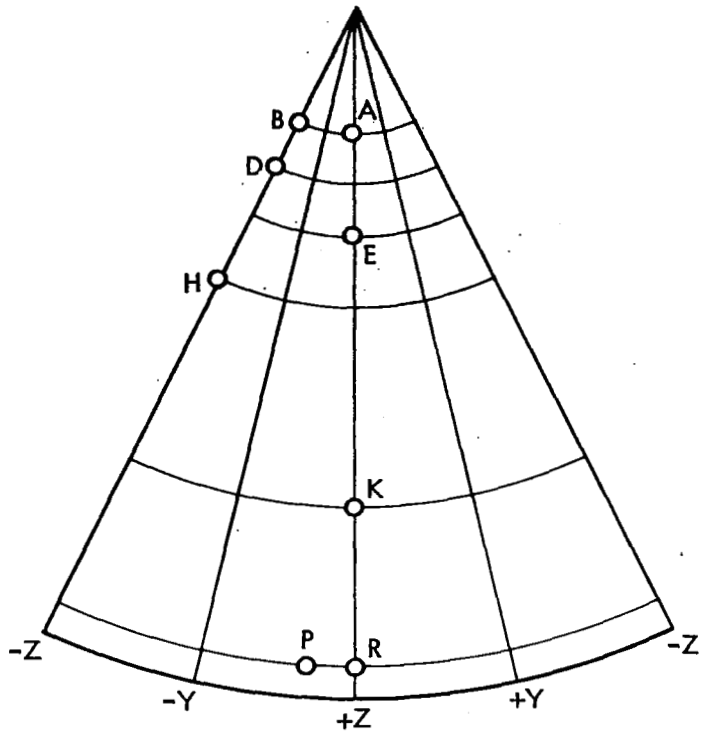

PROBE LOCATION	CHANNEL	PROBE TYPE	SAMPLING RATE, SPS	AXIAL STA (IN.)	ANGLE* (DEG)
A	3	50	1000	32.75	180
D	4	50	1000	47.00	0
E	5	50	1000	67.00	180
H	6	50	1000	88.00	0
K	7	50	1000	139.00	180
R	8	50	1000	166.00	180
B	9	SE	4000	32.75	0
P	10	SE	4000	166.00	150

*CLOCKWISE FROM-Z AXIS, LOOKING FORWARD

Figure 13. Flight 1 Electrostatic Probe Locations

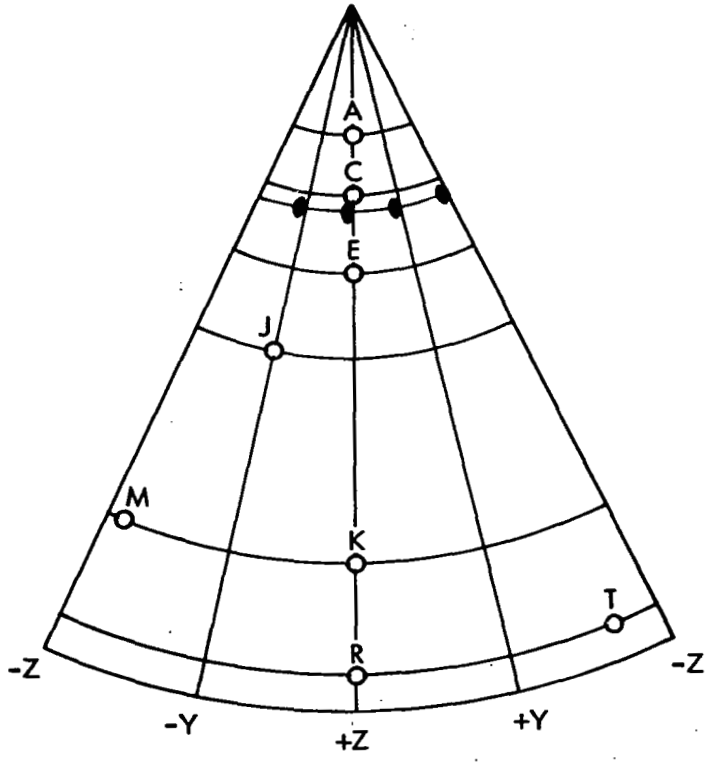

PROBE LOCATION	CHANNEL	PROBE TYPE	SAMPLING RATE (SPS)	AXIAL STA (IN.)	ANGLE* (DEG)
T	3	B-50	1000	166.00	330
C	4	B-50	1000	47.50	180
J	5	B-SE	1000	88.00	90
M	6	B-SE	1000	139.00	15
A	7	B-50	1000	32.75	180
E	8	B-50	1000	67.00	180
K	9	B-50	4000	139.00	180
R	10	B-SE	4000	166.00	180

*Clockwise from Z axis, looking forward.

Figure 14. Flight 2 Electrostatic Probe Locations

Figure 15. Typical Calculated Local Angles-of-Attack and Sensor Angles Relative to the Windward Meridian

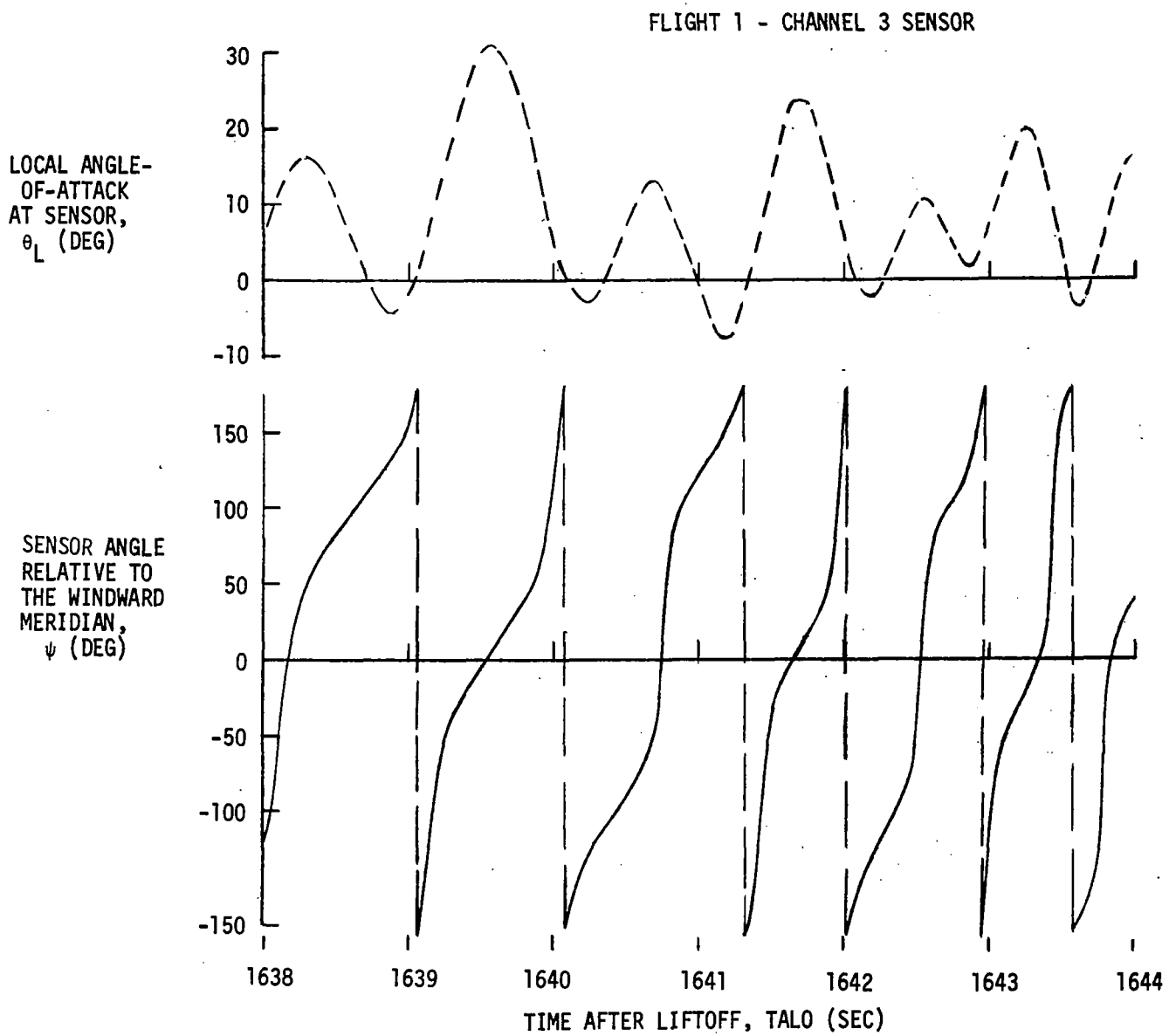

Figure 16. Flight 2 Sound Pressure Level and Local Angle-of-Attack Histories - Channel 3 Sensor

$X = 88''$, $\phi_S = 101°$

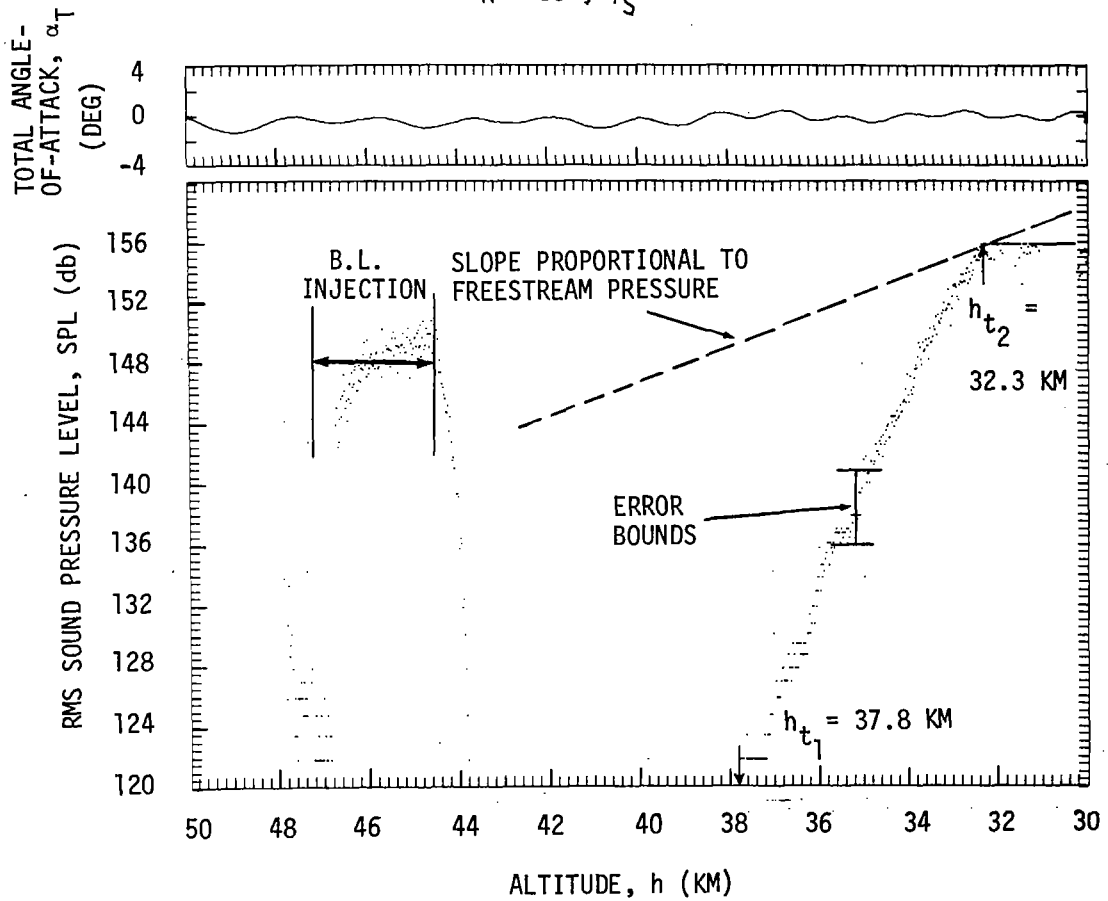

Figure 17. Flight 2 Sound Pressure Level and Local Angle-of-Attack Histories - Channel 4 Sensor

$X = 166''$, $\phi_S = 110°$

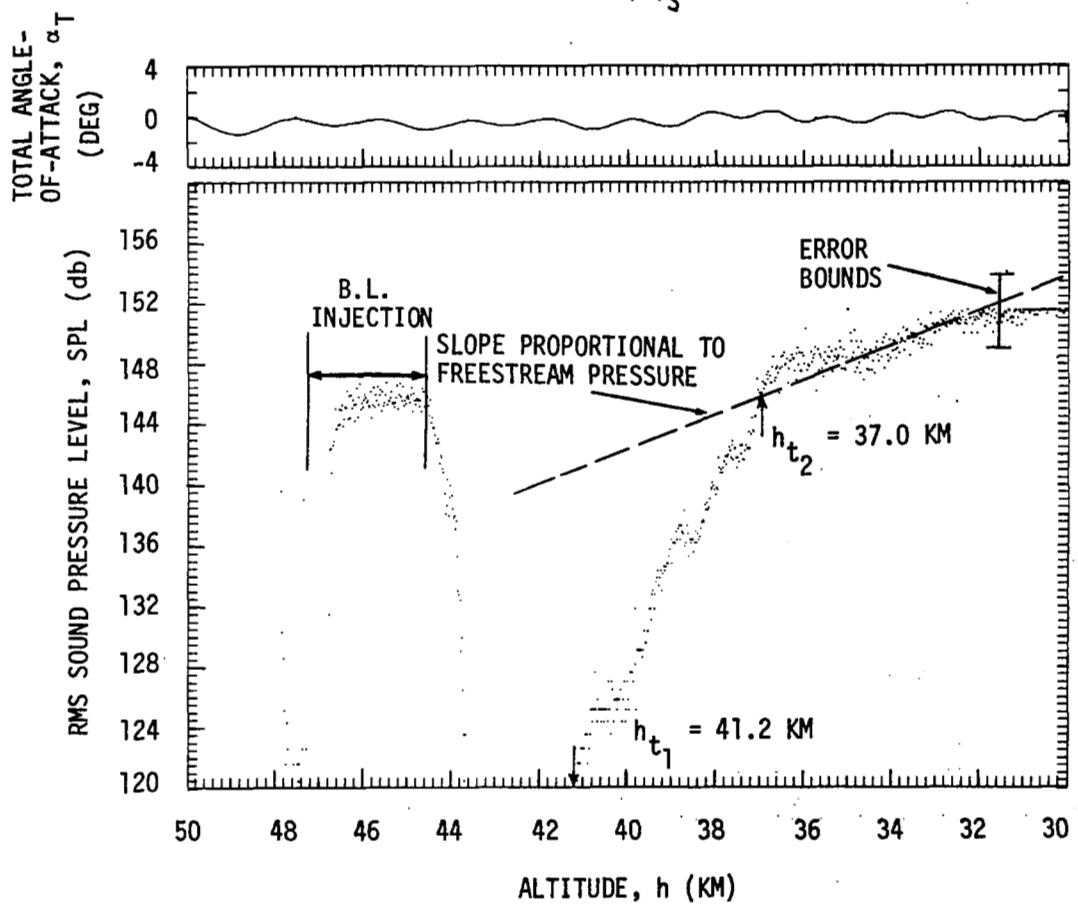

Figure 18. Flight 2 Sound Pressure Level and Local Angle-of-Attack Histories - Channel 5 Sensor

$X = 166''$, $\phi_S = 290°$

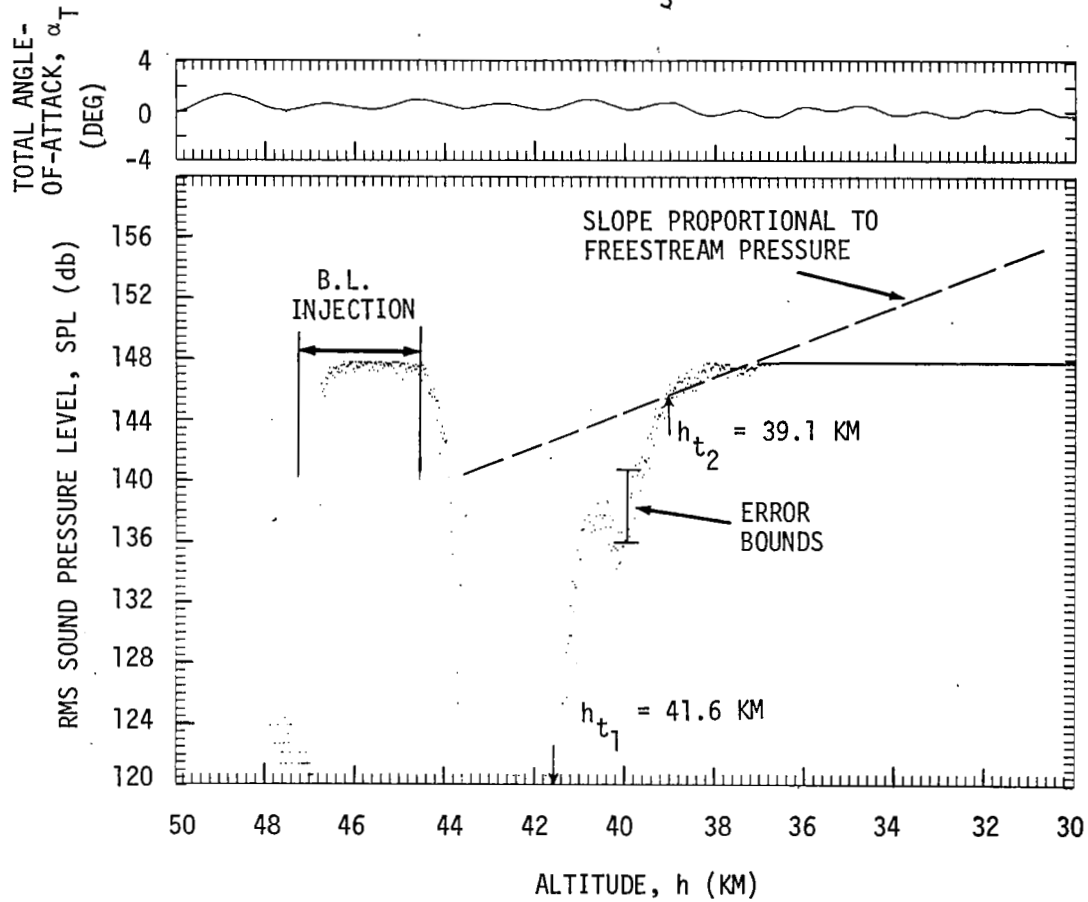

Figure 19. Determination of Transition Altitude From Base Pressure Response

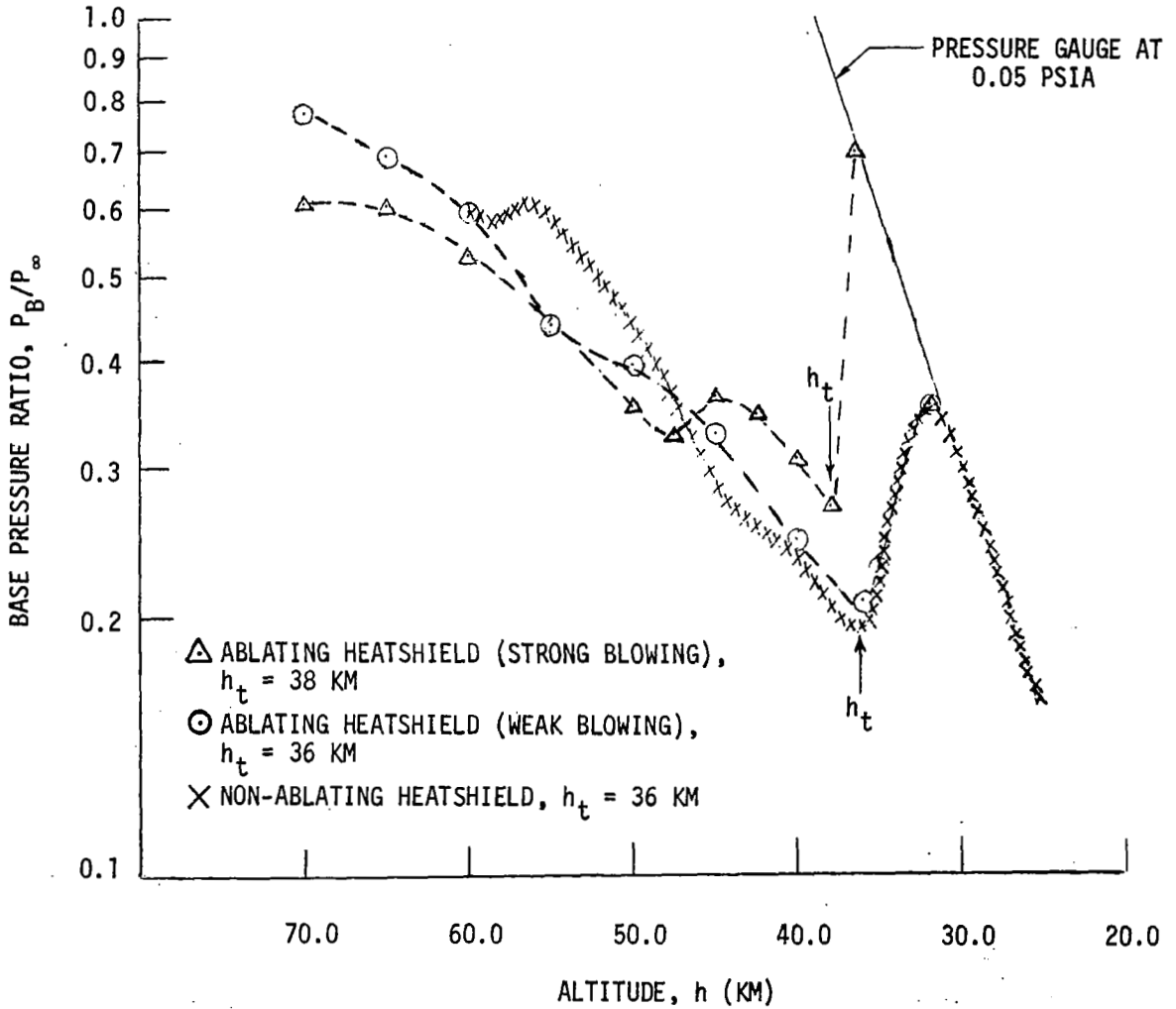

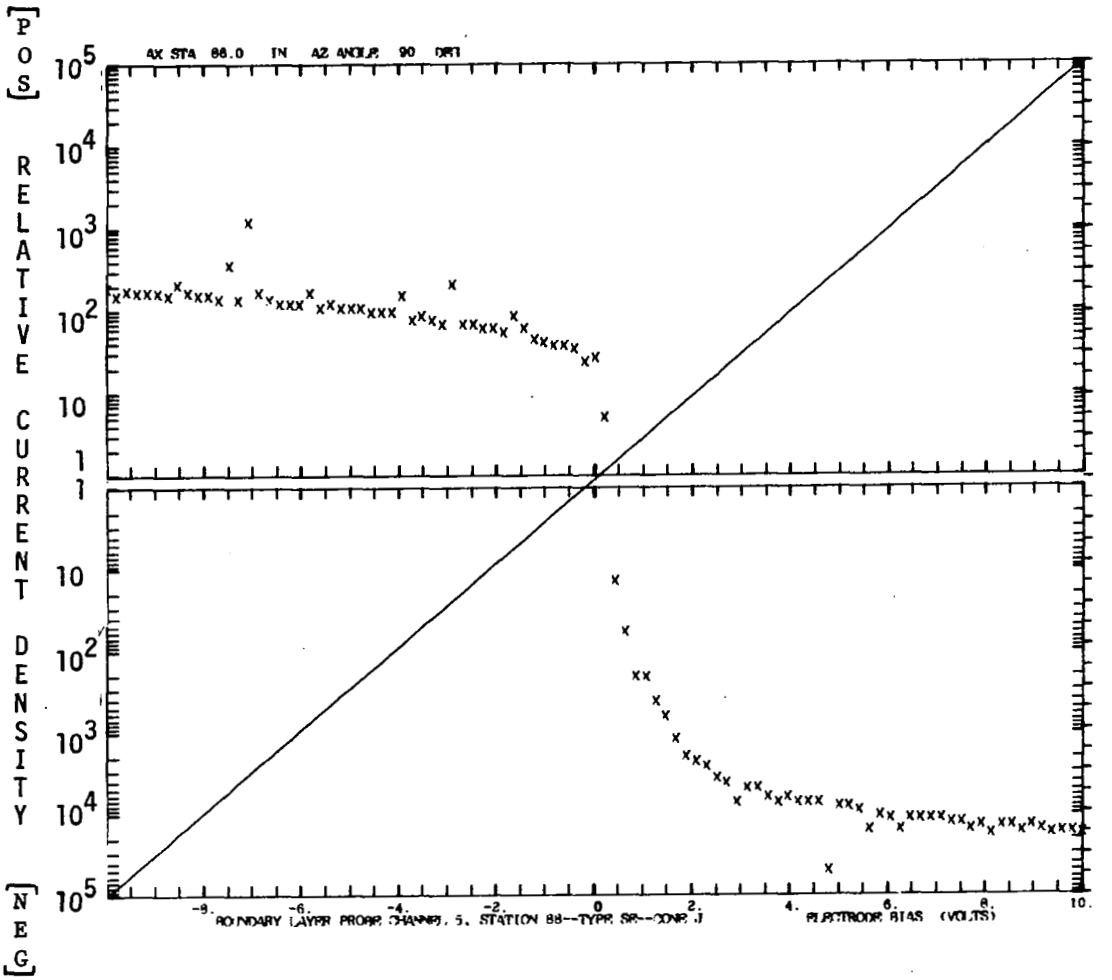

Figure 20. Electrostatic Probe Current-Voltage Characteristic with Fluctuations of Type 1 (see Section 4.2.3)--Flight 2

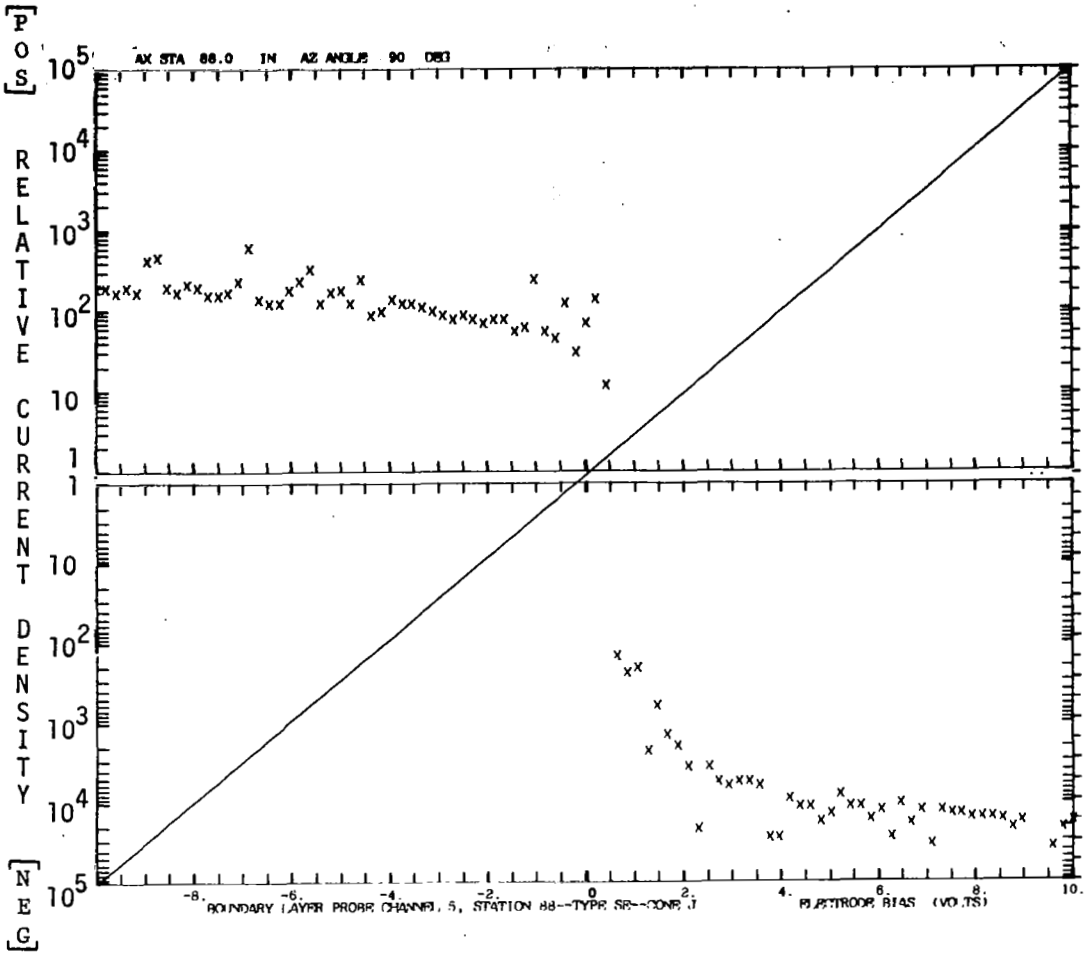

Figure 21. Electrostatic Probe Current-Voltage Characteristic with Fluctuations of Type 2 (see Section 4.2.3)--Flight 2

Figure 22. Flight 2 Boundary Layer Transition Altitudes Versus Vehicle Axial Station

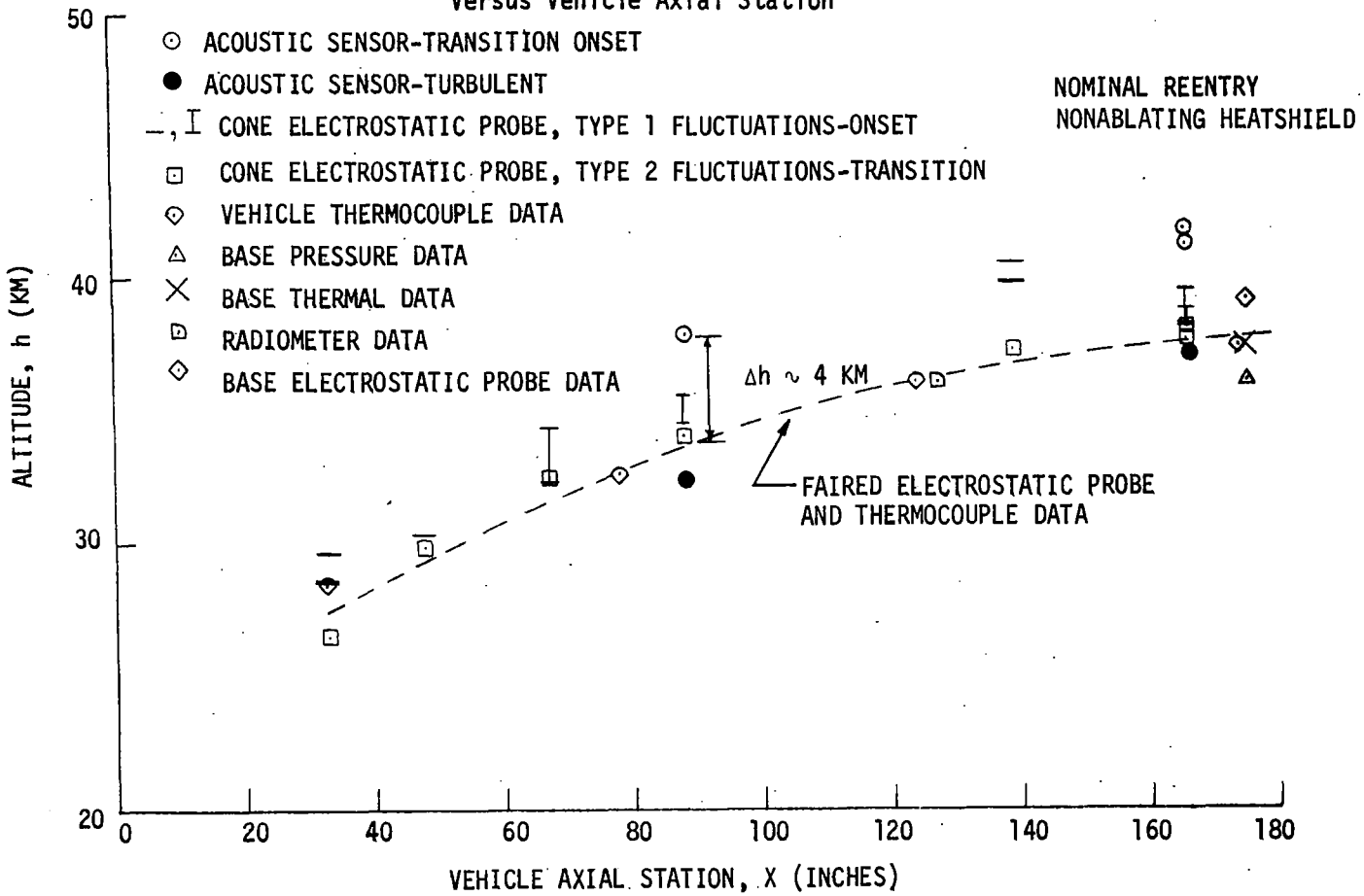

Figure 23. Transition Altitudes Versus Vehicle Axial Station for an Ablating Vehicle (Flight 3)

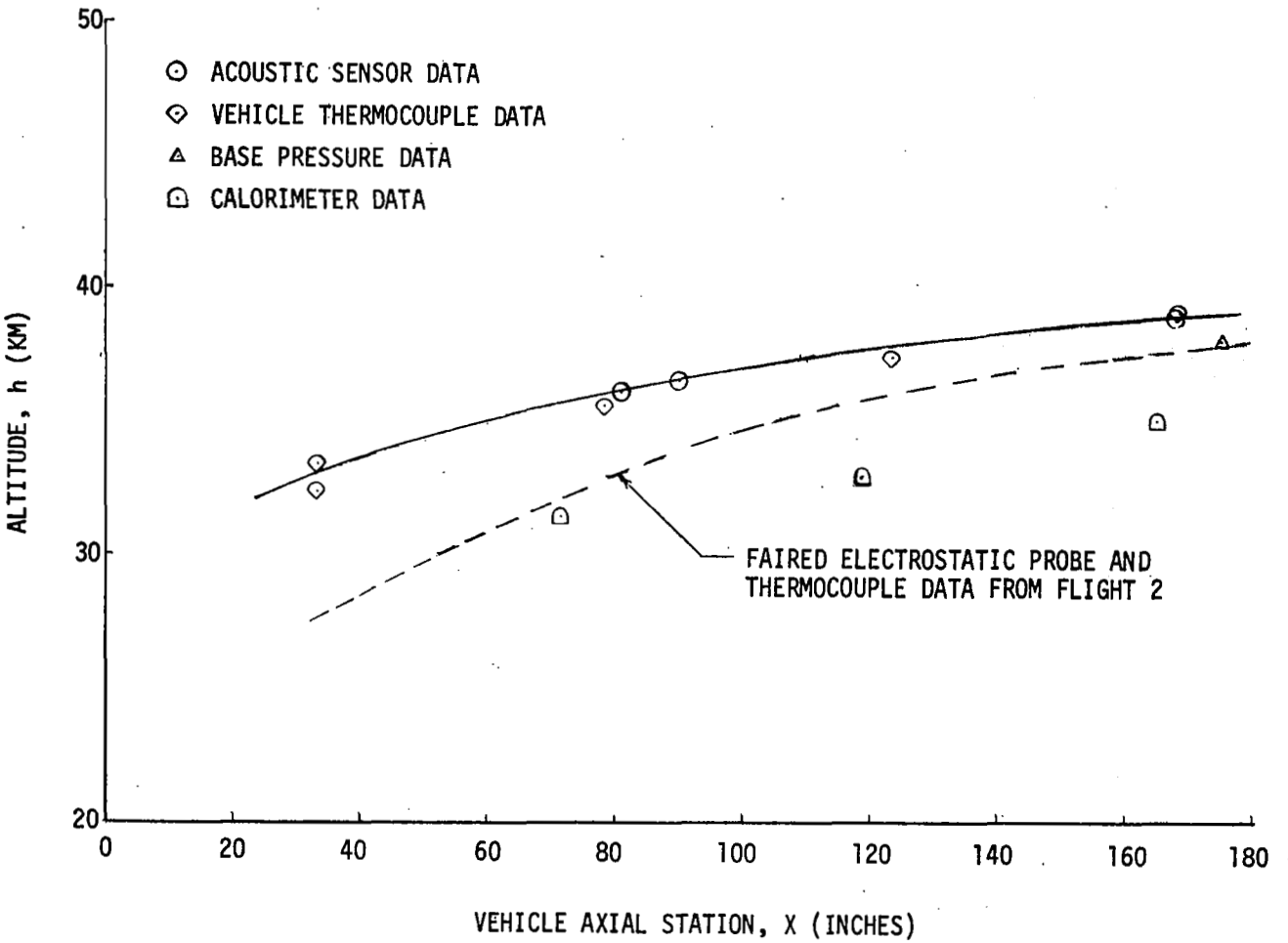

Figure 24. Flight 1 Sound Pressure Level Data - Channel 3 Sensor

$X = 88", \phi_S = 101°$

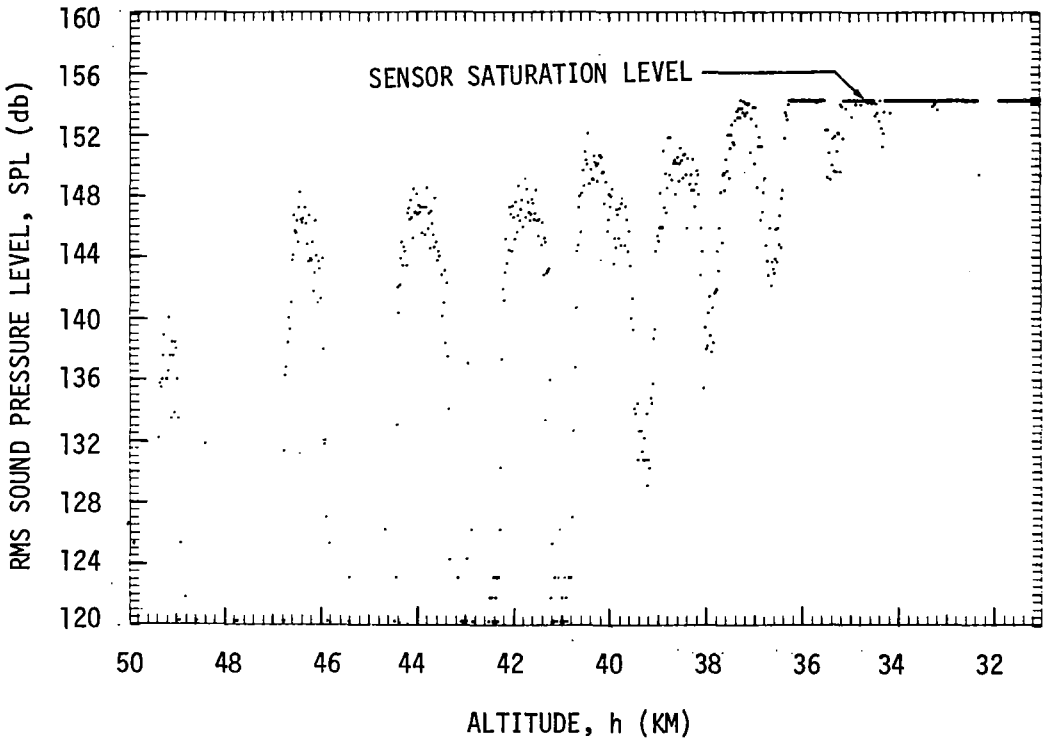

Figure 25. Flight 1 Sound Pressure Level Data - Channel 4 Sensor

$X = 166"$, $\phi_S = 110°$

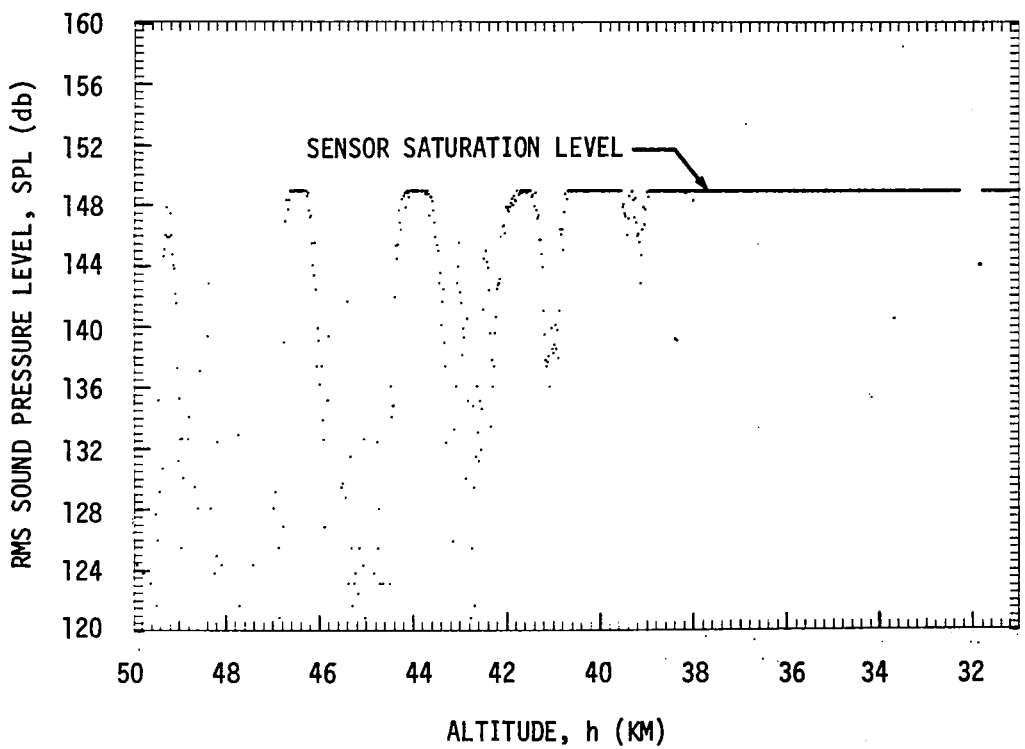

Figure 26. Flight 1 Sound Pressure Level Data - Channel 5 Sensor

$X = 166", \phi_S = 290°$

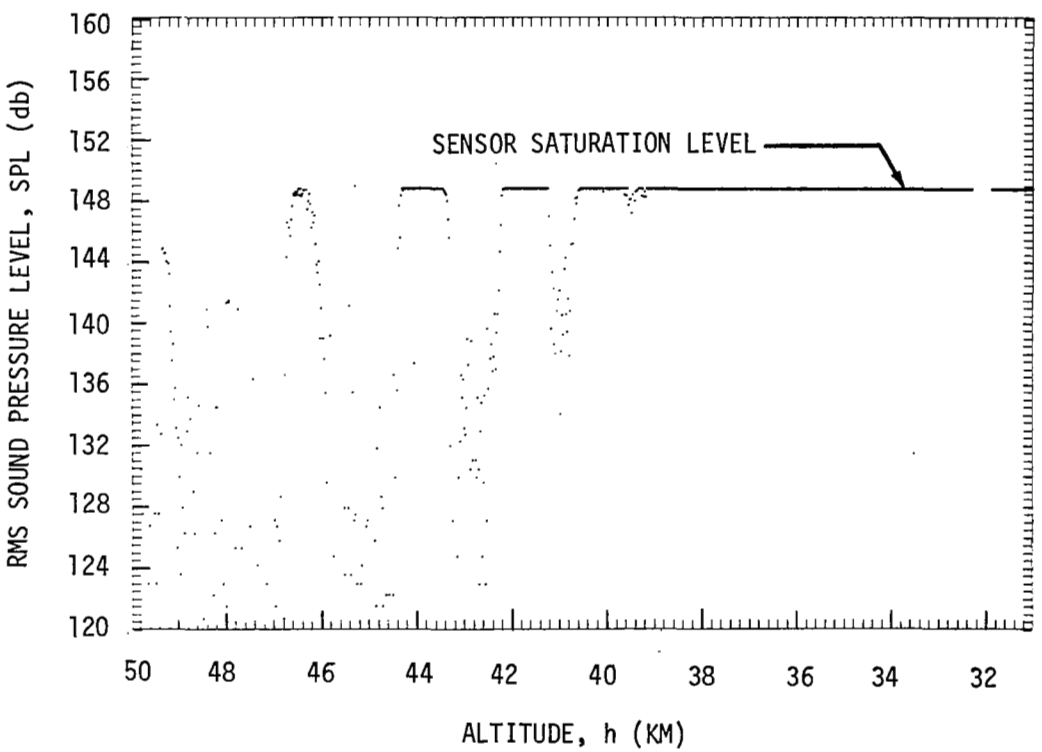

Figure 27
Flight 1 Surface Pressure Fluctuation and Total and Local Angle-of-Attack Histories

Channel 3 Sensor, X = 88", ϕ_s = 101°

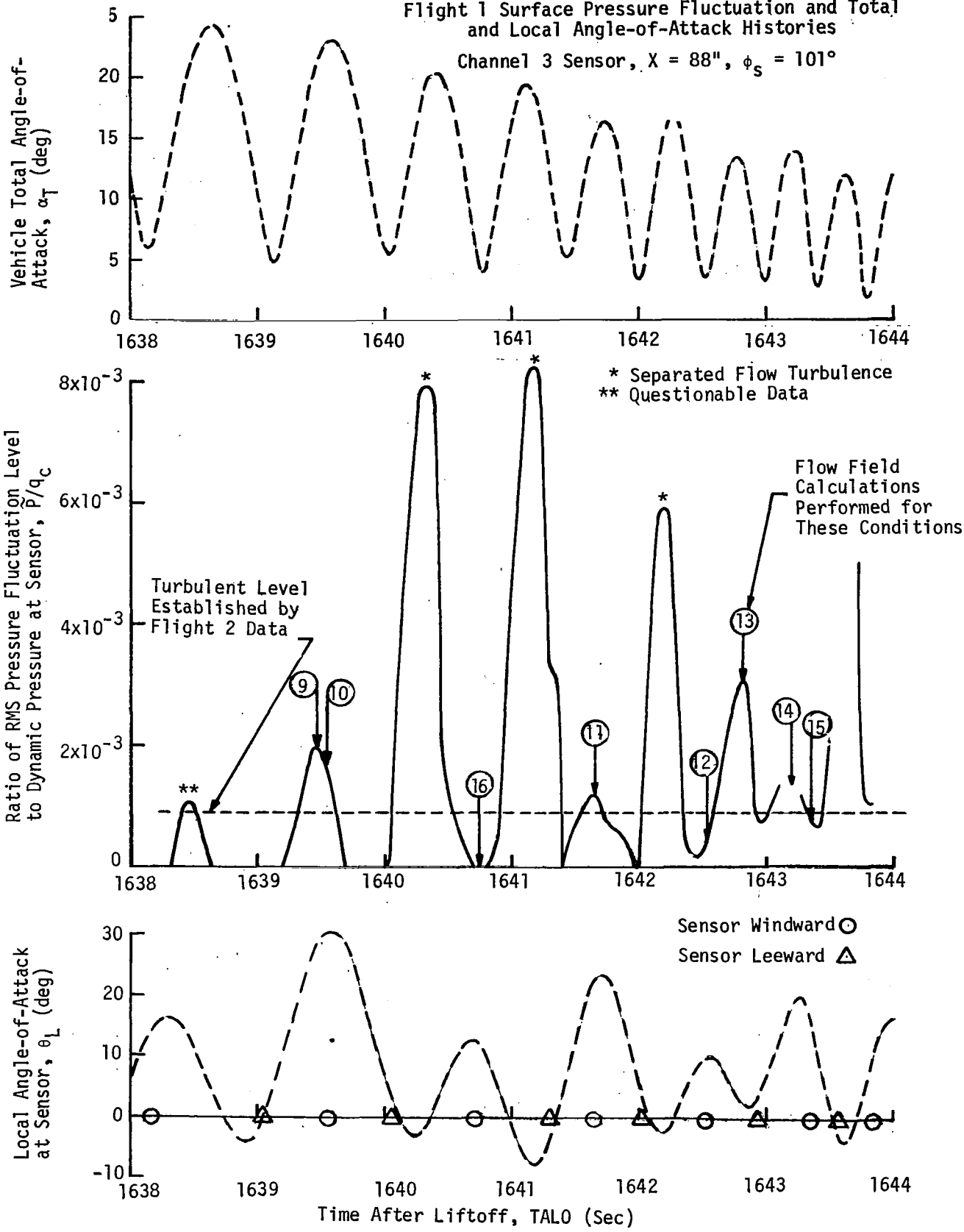

Figure 28

Flight 1 Surface Pressure Fluctuation and Tota
and Local Angle-of-Attack Histories

Channel 4 Sensor, X = 166", ϕ_s = 110°

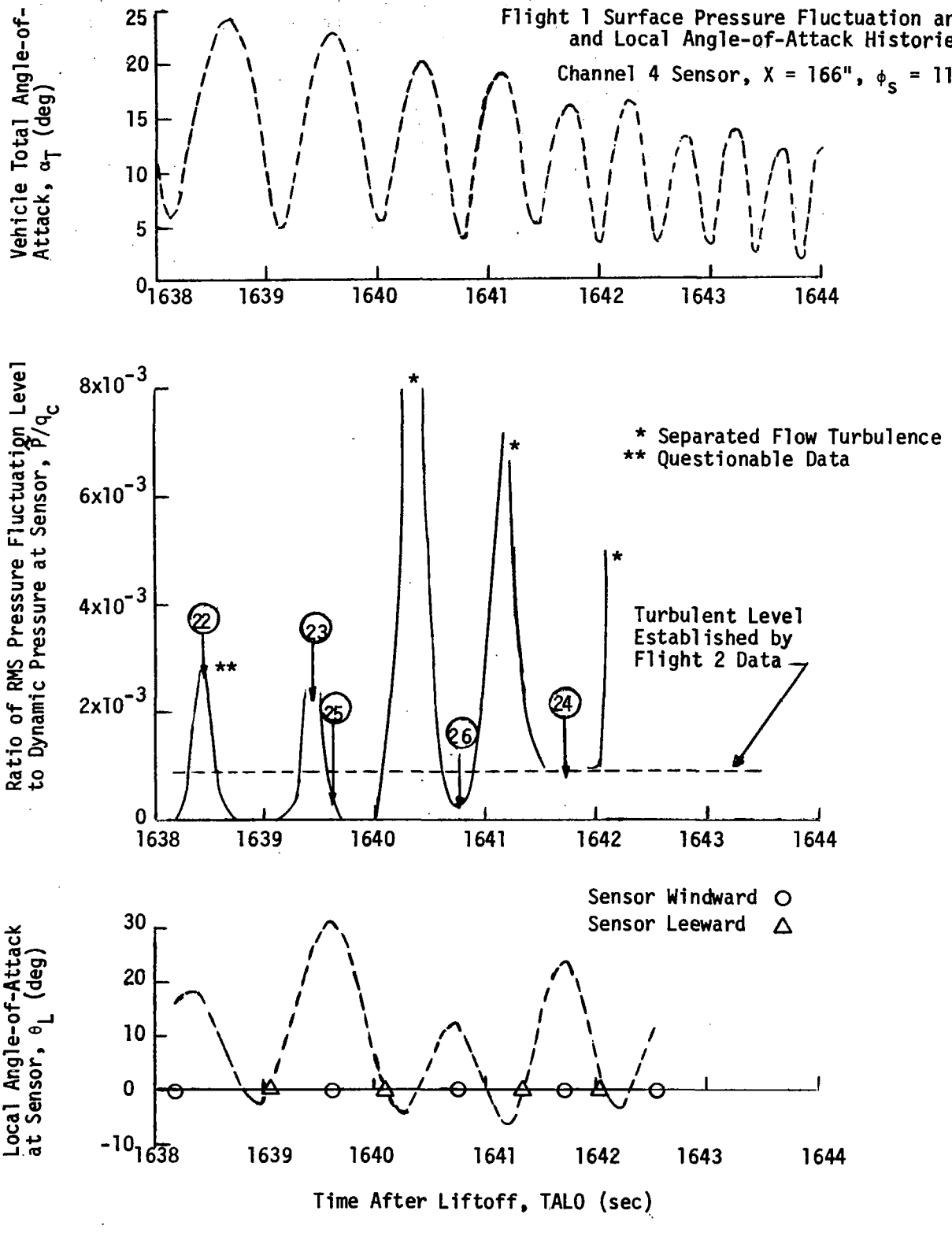

Figure 29

Flight 1 Surface Pressure Fluctuation and Total and Local Angle-of-Attack Histories

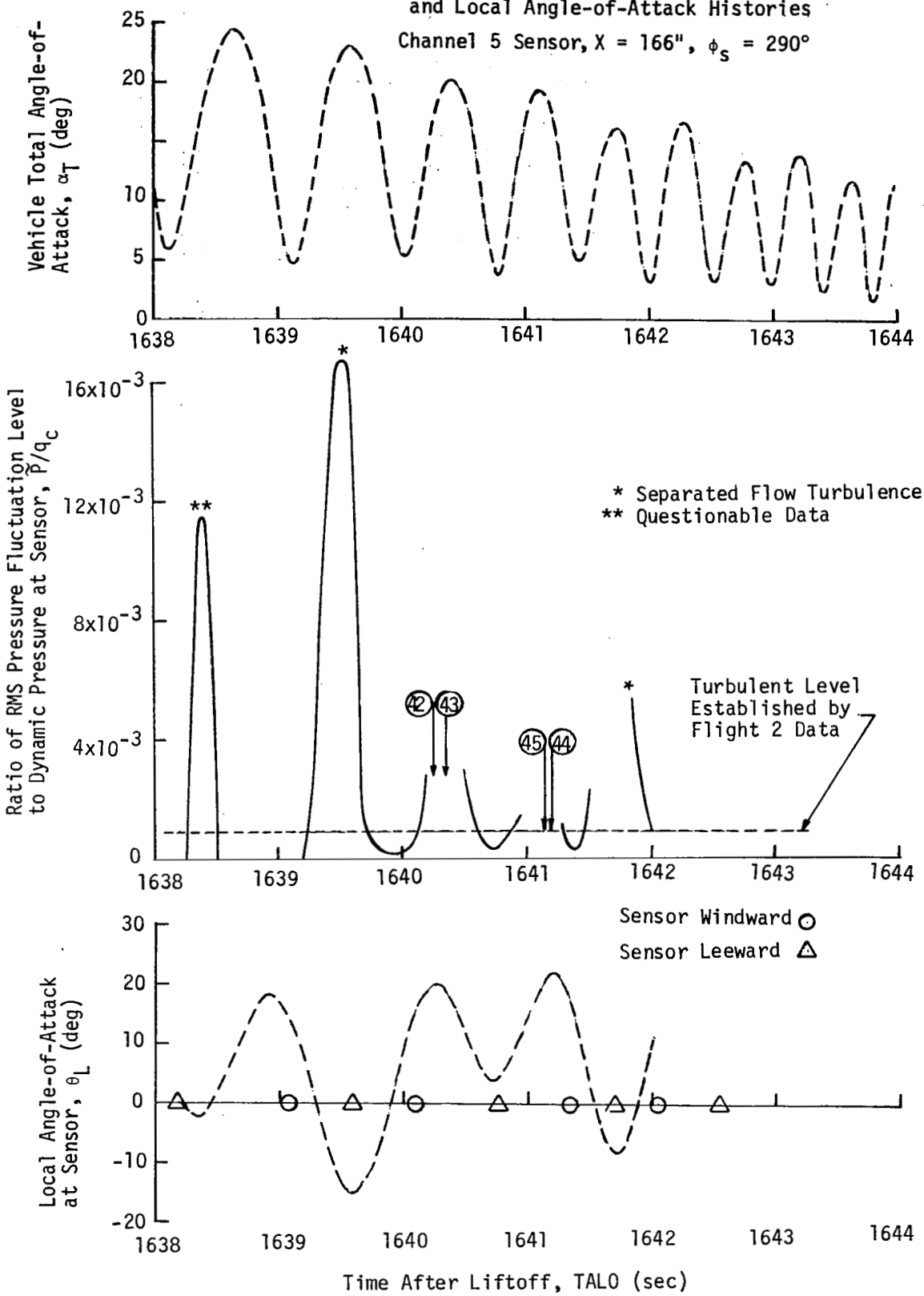

Figure 30. Comparison of Sound Pressure Level Data From Flights 1 and 2

Channel 3 Sensor, X = 88", ϕ_S = 101°

** Questionable Data

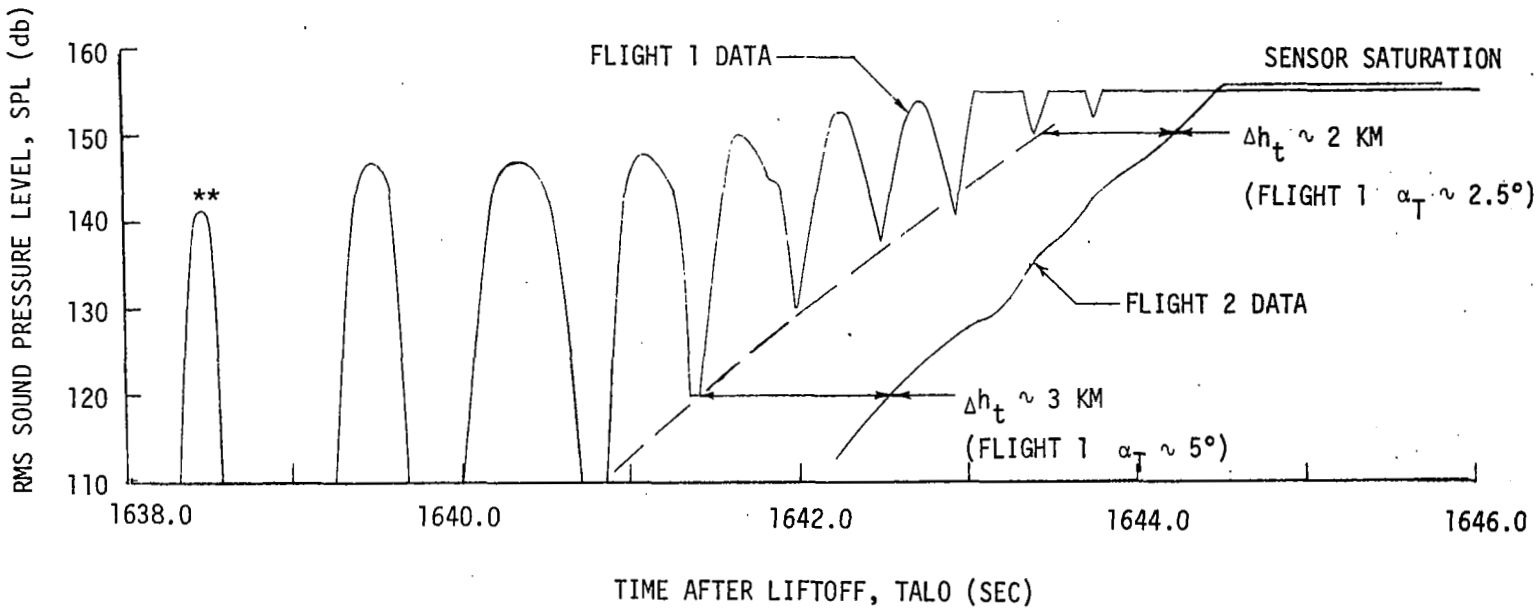

Figure 31. Flight 1 Base Pressure and Total Angle-of-Attack Variation With Altitude

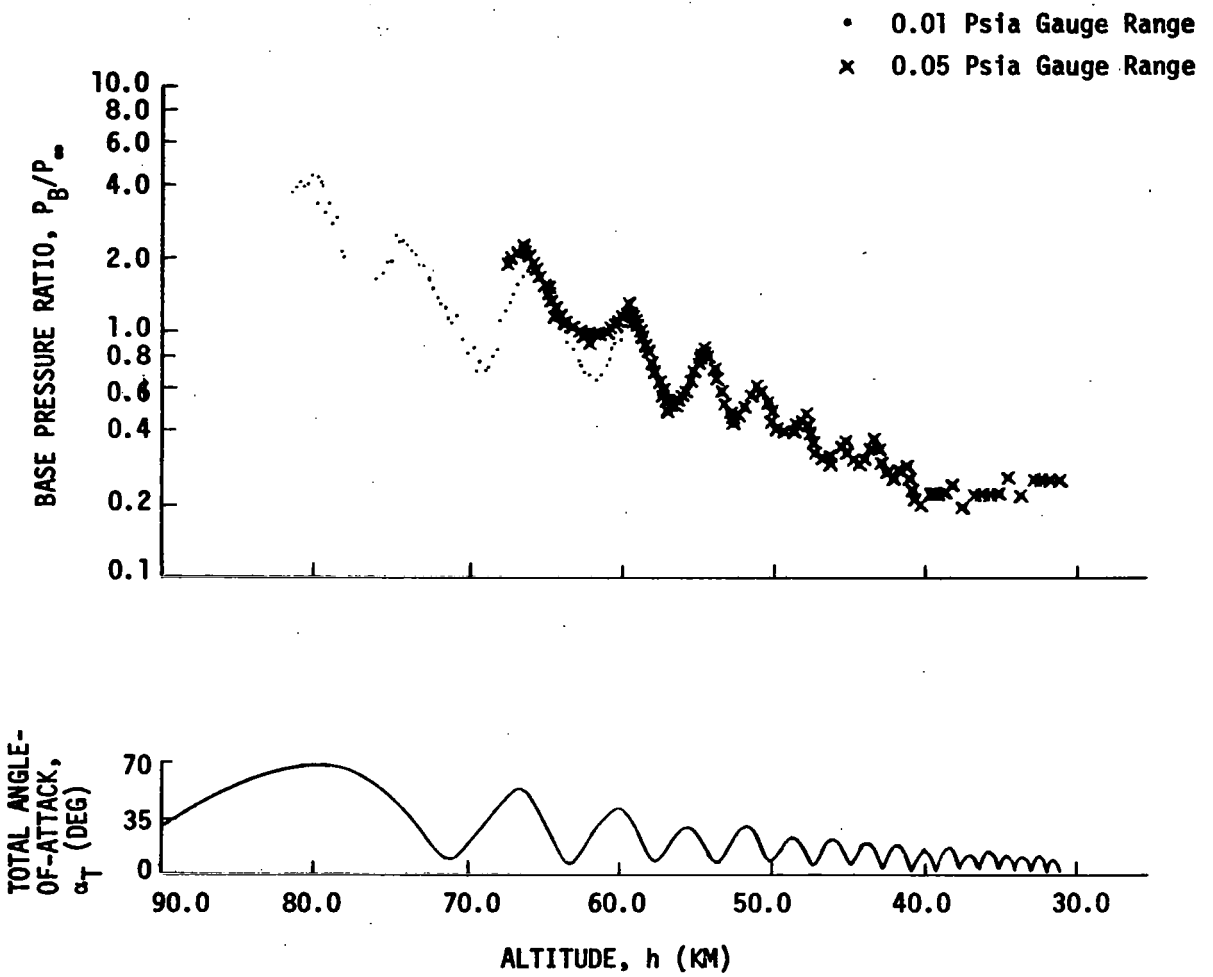

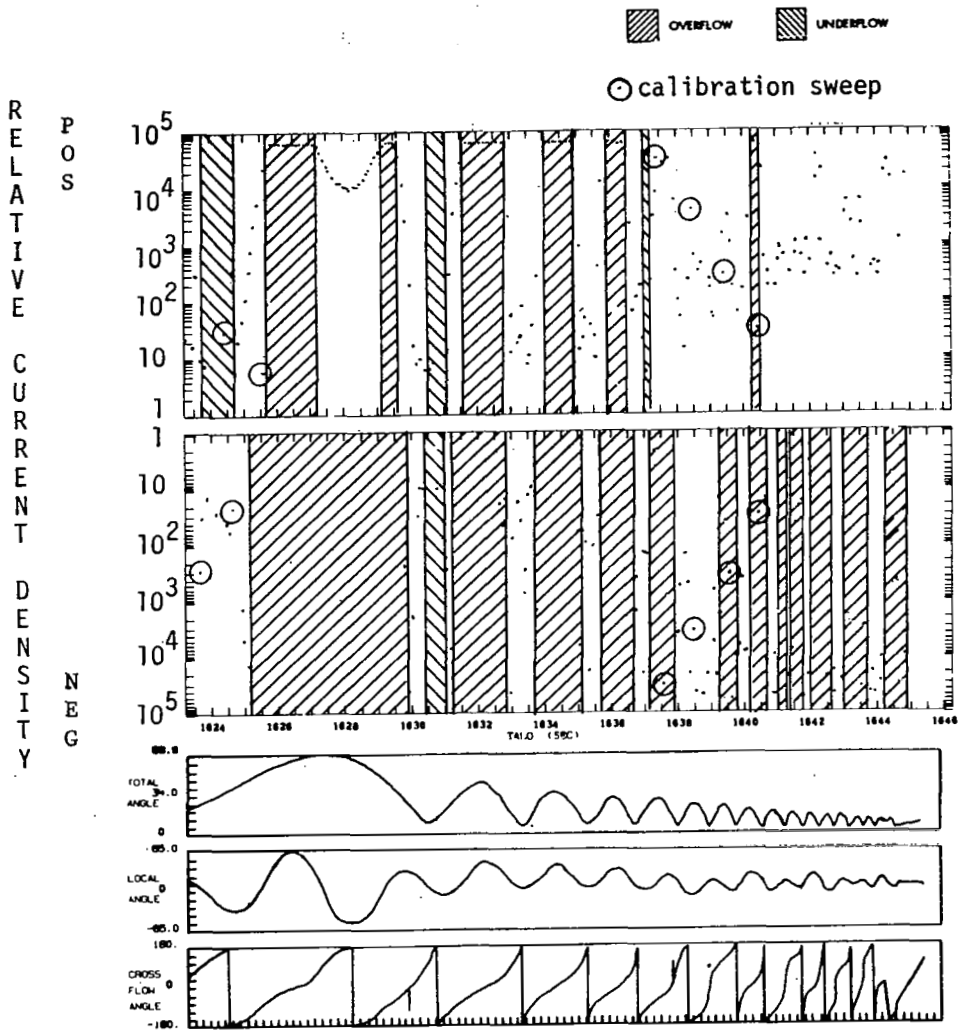

Figure 32. Example of Electrostatic Probe Saturation Current Density History, Probe on ϕ_S = 0°, Flight 1

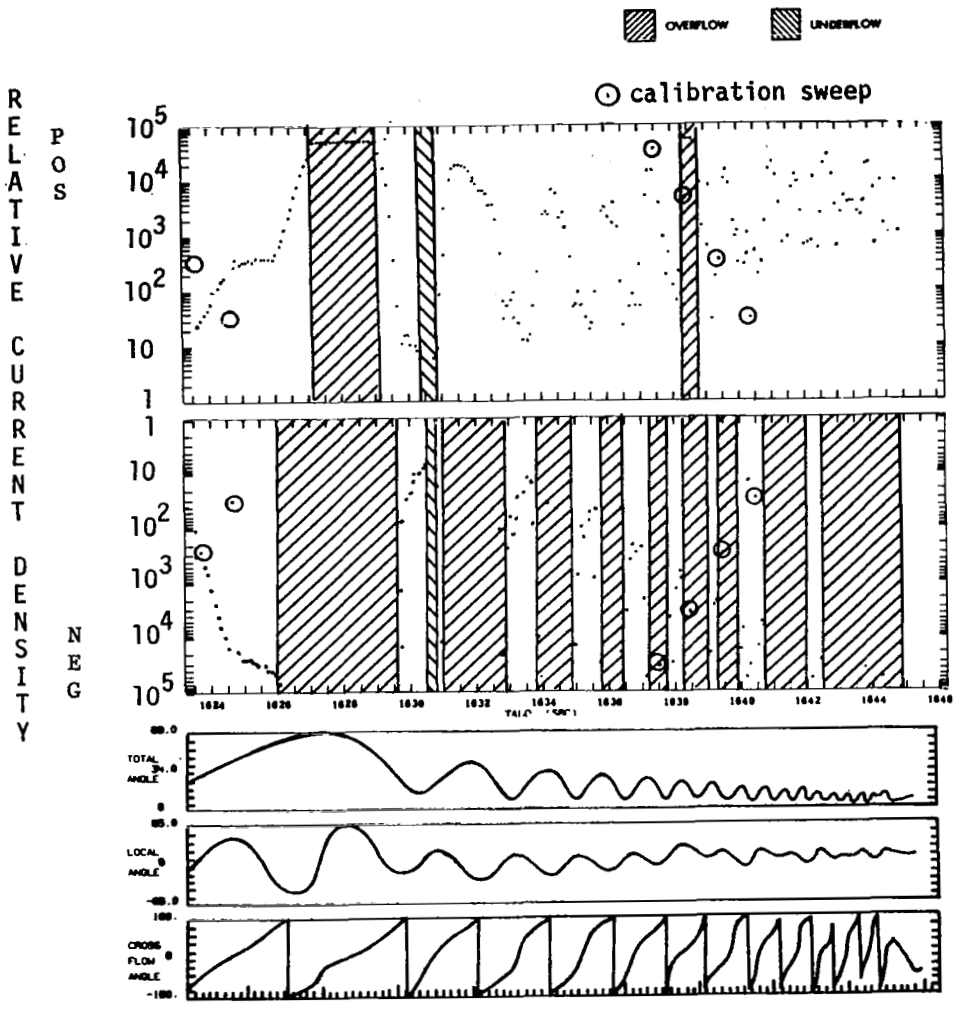

Figure 33. Example of Electrostatic Probe Saturation Current Density History, Probe on ϕ_s = 180°, Flight 1

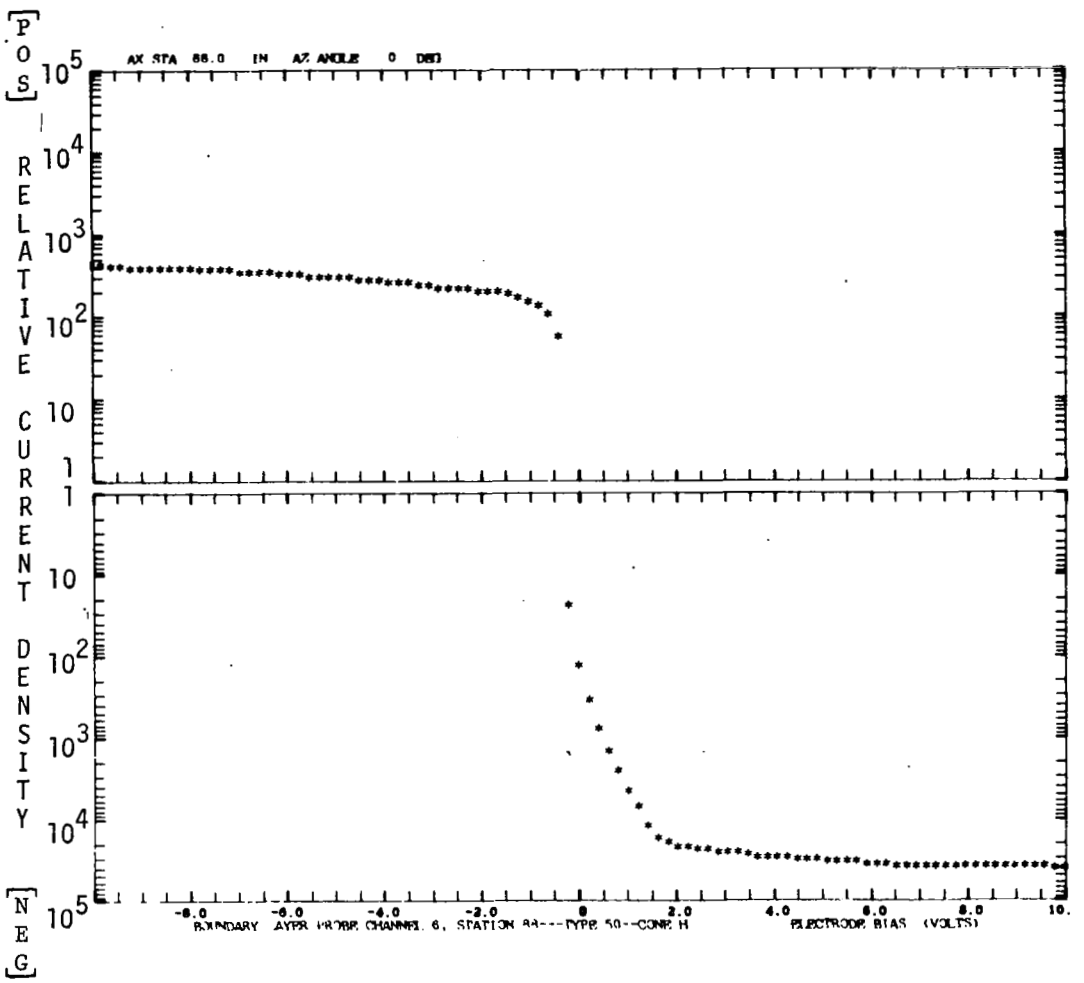

Figure 34. Example of Electrostatic Probe Current-Voltage Characteristic Measured under Laminar Flow Conditions--Flight 1

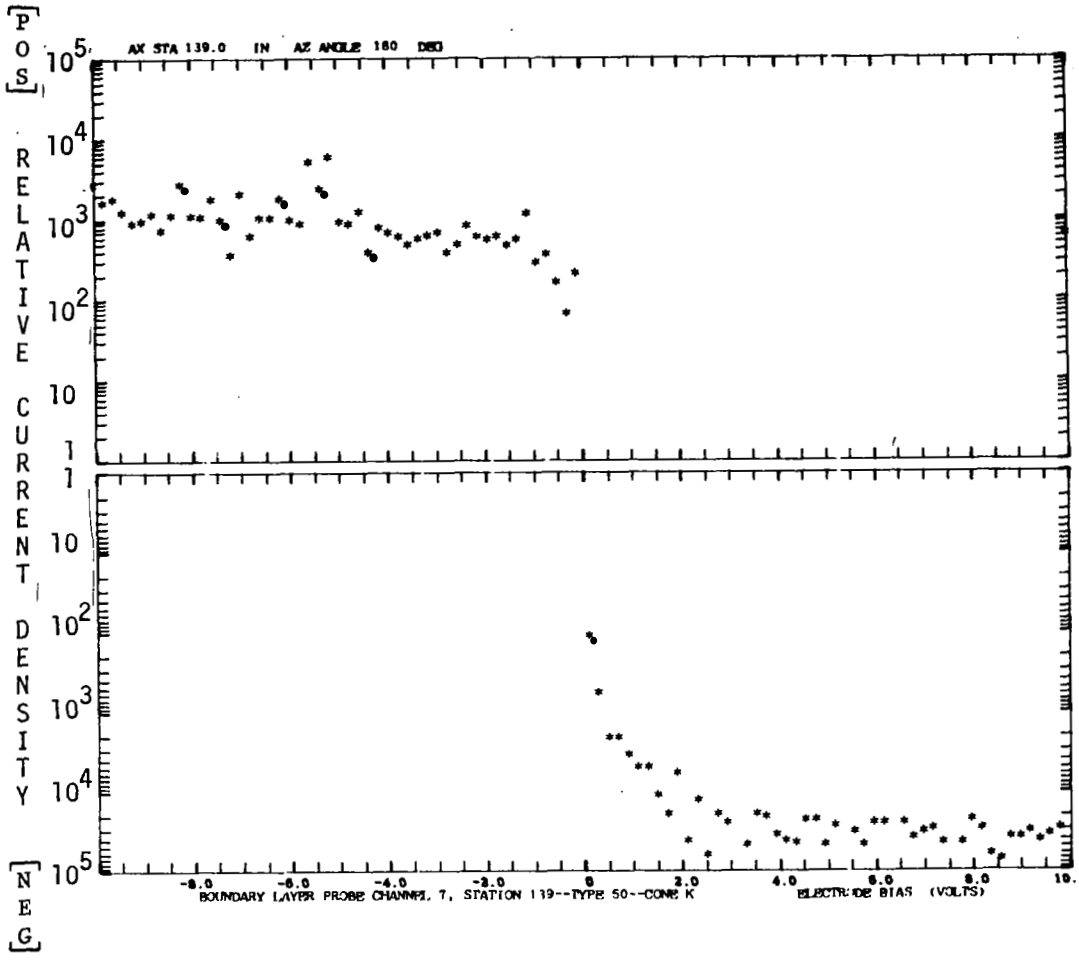

Figure 35. Example of Electrostatic Probe Current-Voltage Characteristic Measured under Turbulent Flow Conditions--Flight 1

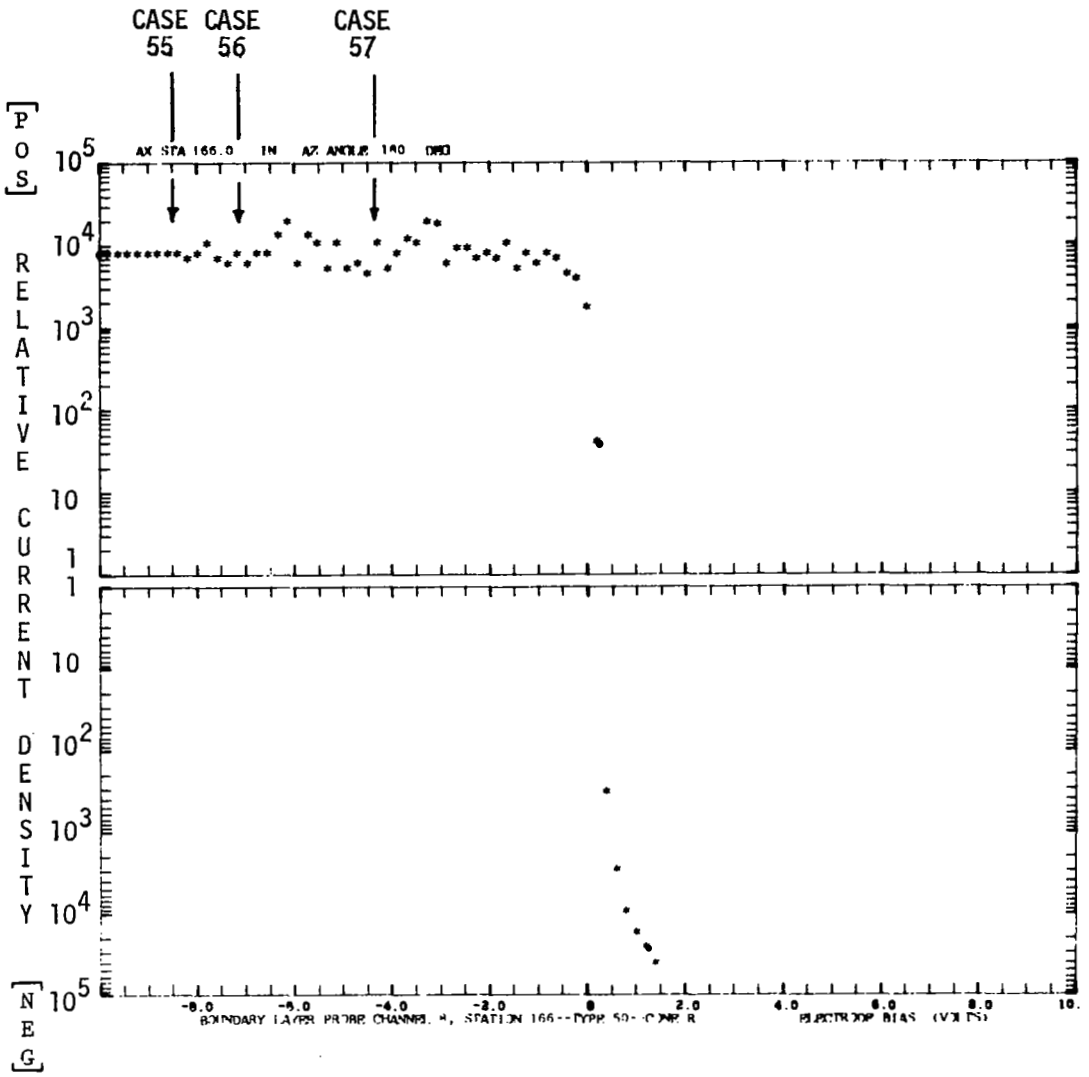

Figure 36. Example of Onset of Fluctuations in Electrostatic Probe Current-Voltage Characteristic --Flight 1

Figure 37. Flight 1 Boundary Layer Transition Altitudes Based on Thermocouple Data

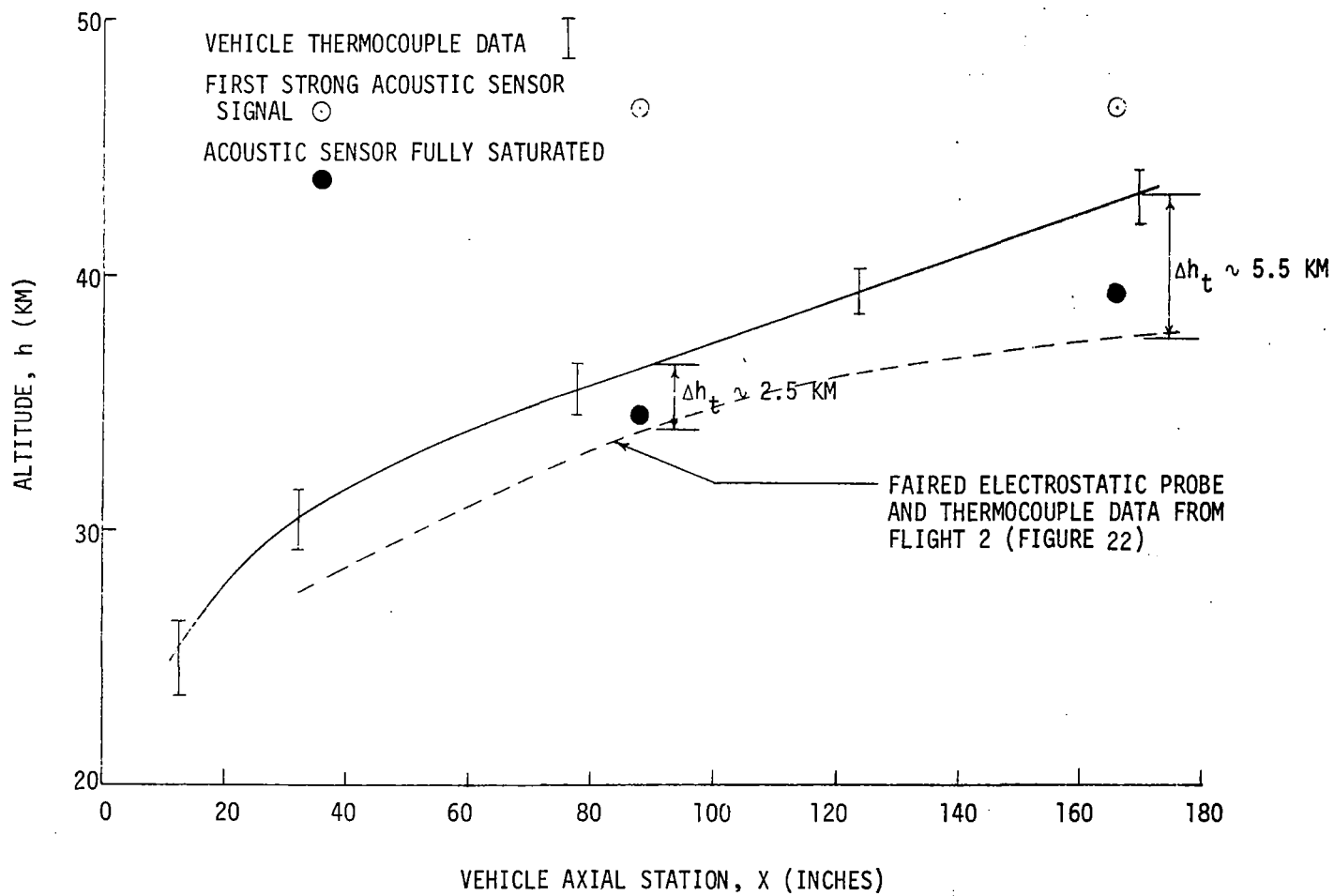

Figure 38. Variation of Boundary Layer Displacement Thickness on A Cone at Zero Angle-of-Attack

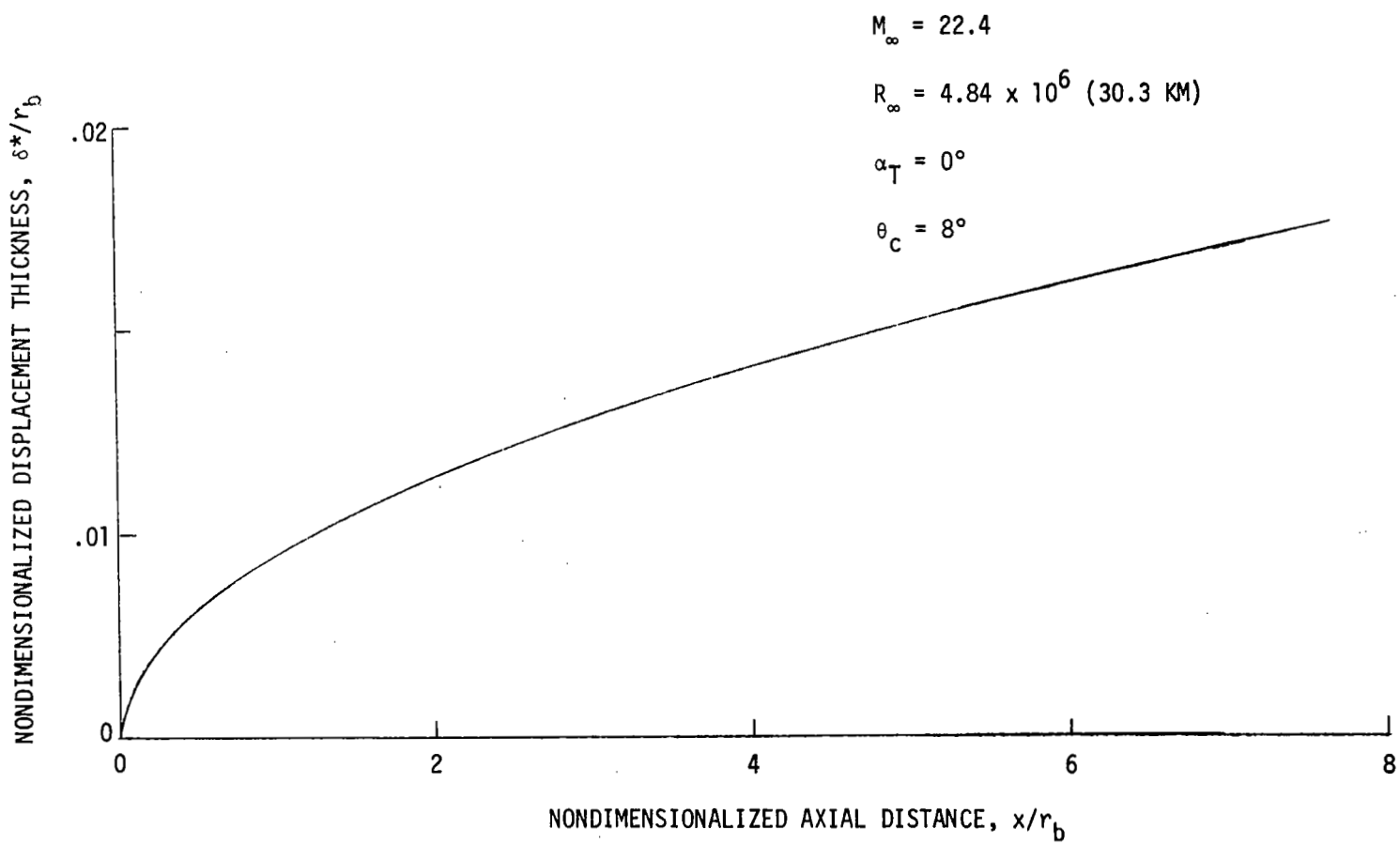

Figure 39. Inviscid Surface Streamlines for a Total Angle-of-Attack of 12 Degrees

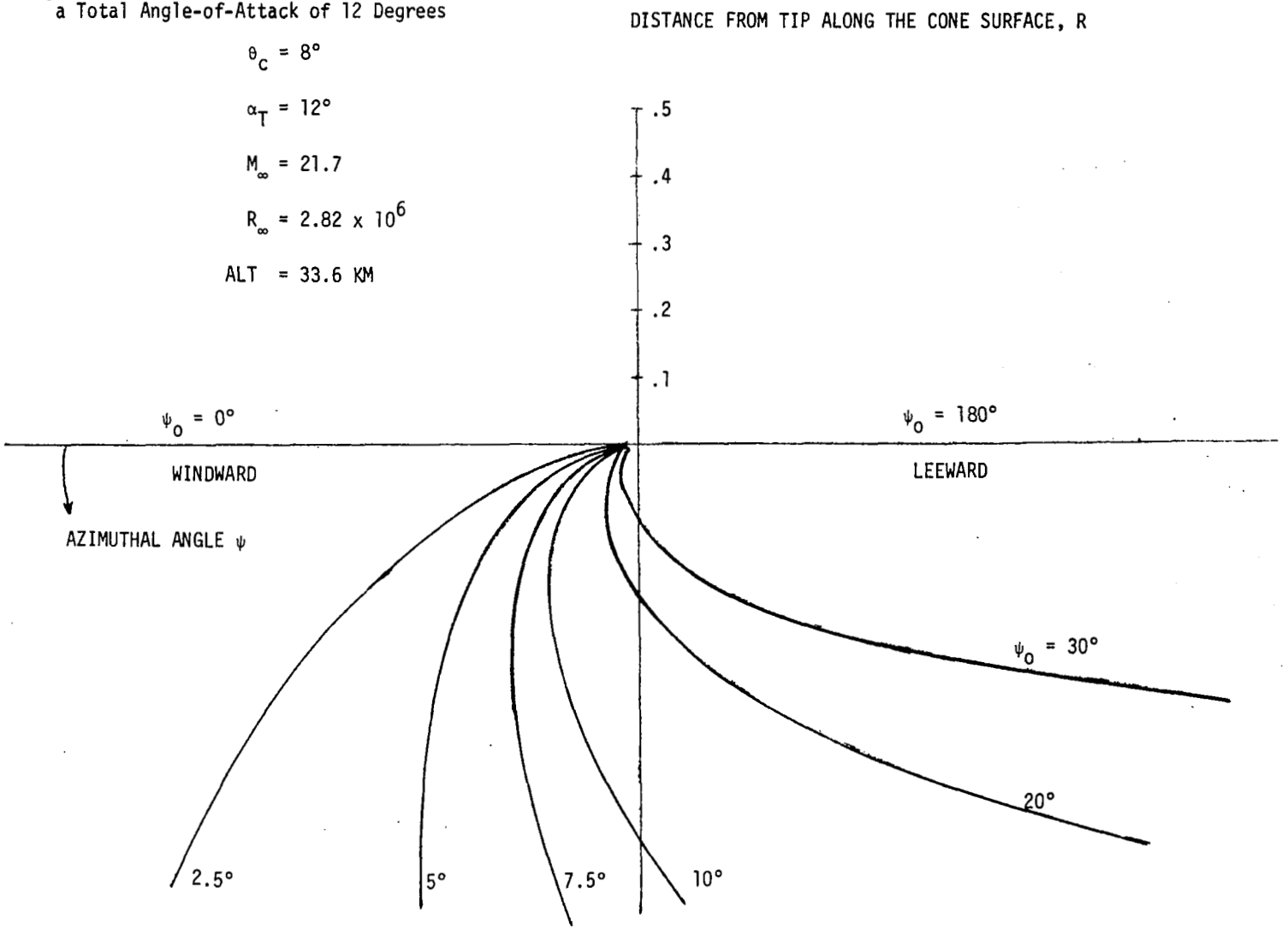

Figure 40. Inviscid Streamlines for a Total Angle-of-Attack of 28 Degrees

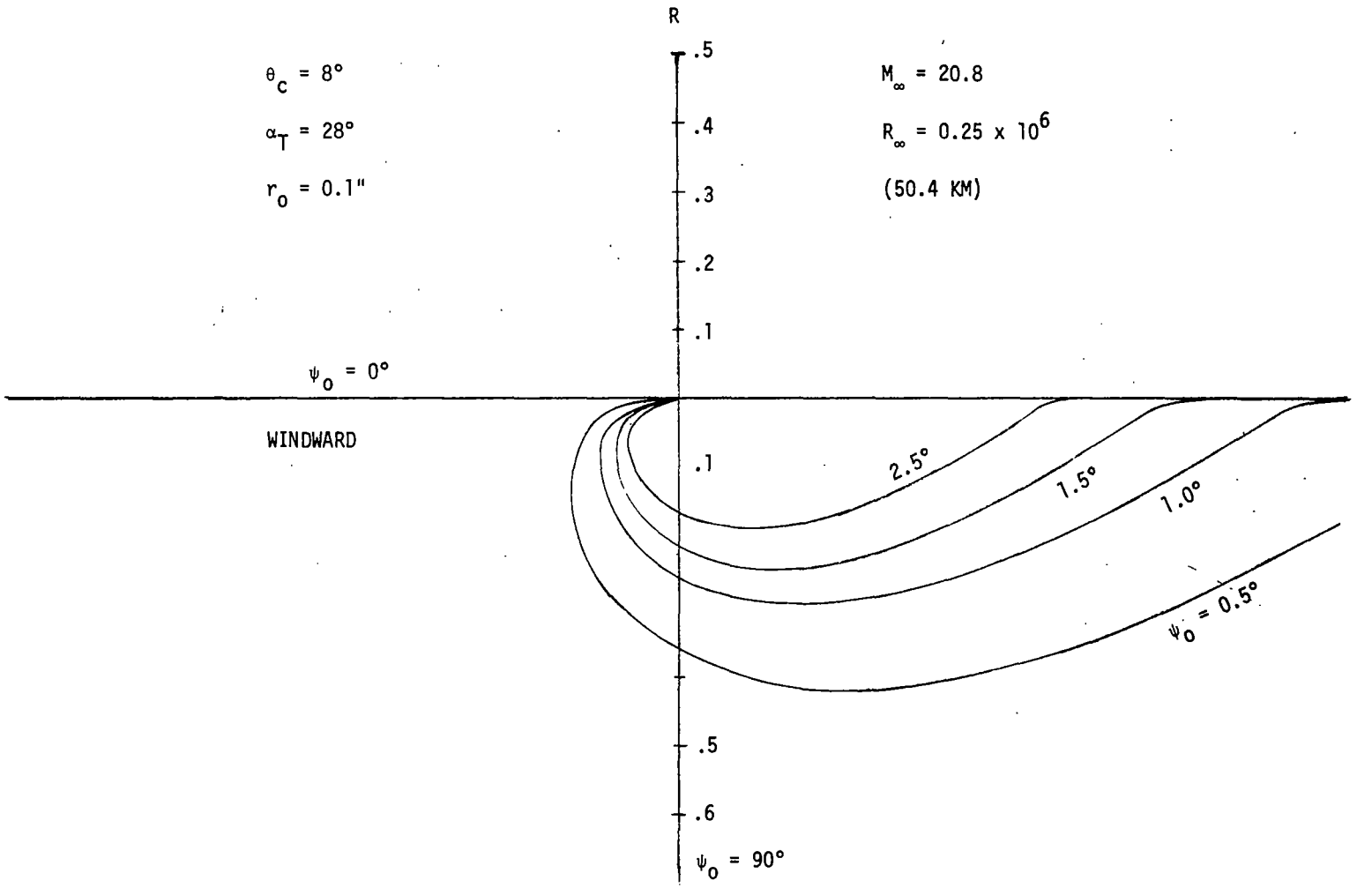

Figure 41. Variation of Pressure Coefficient Along Inviscid Streamlines

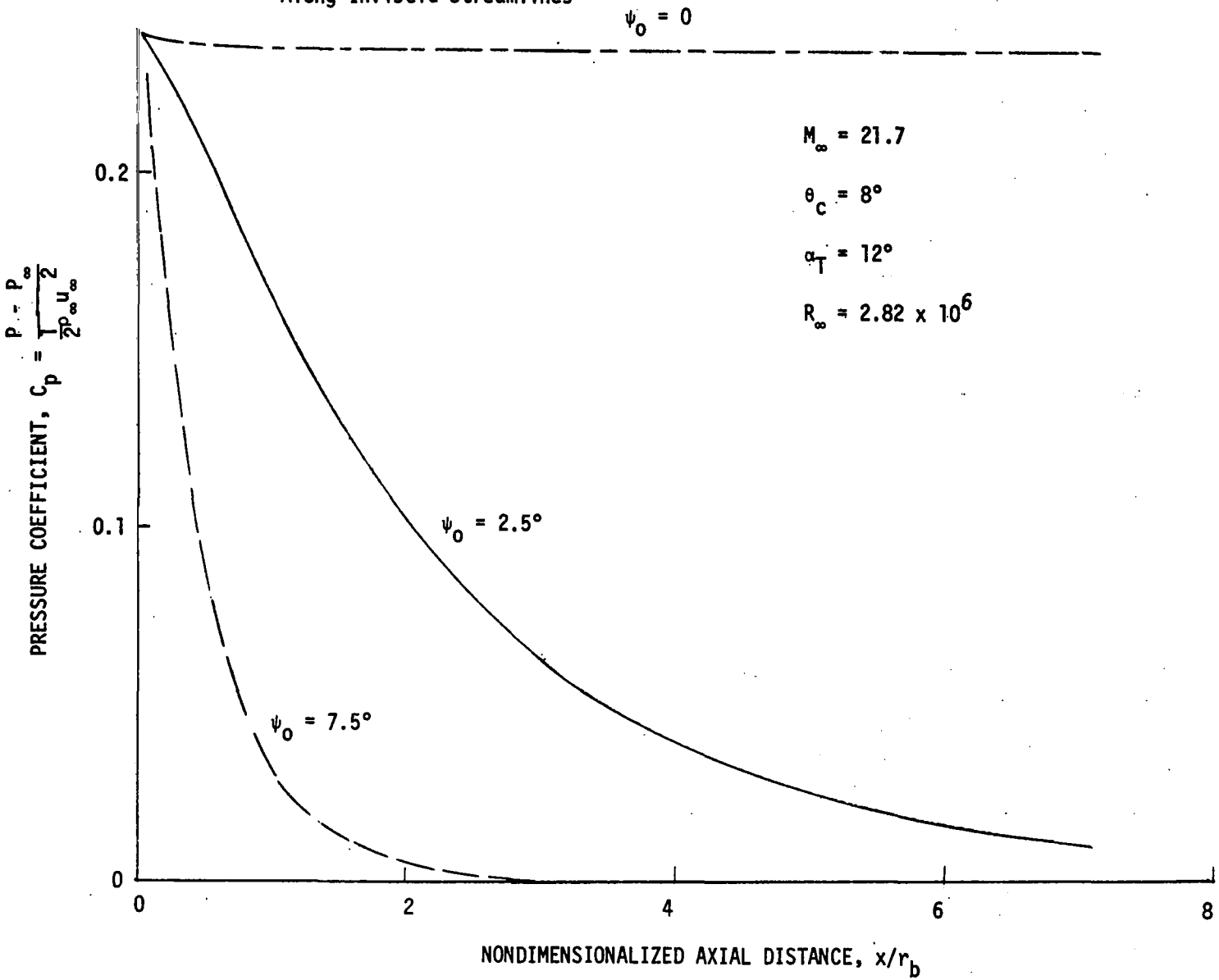

Figure 42. Variation of Displacement Thickness Along An Inviscid Streamline

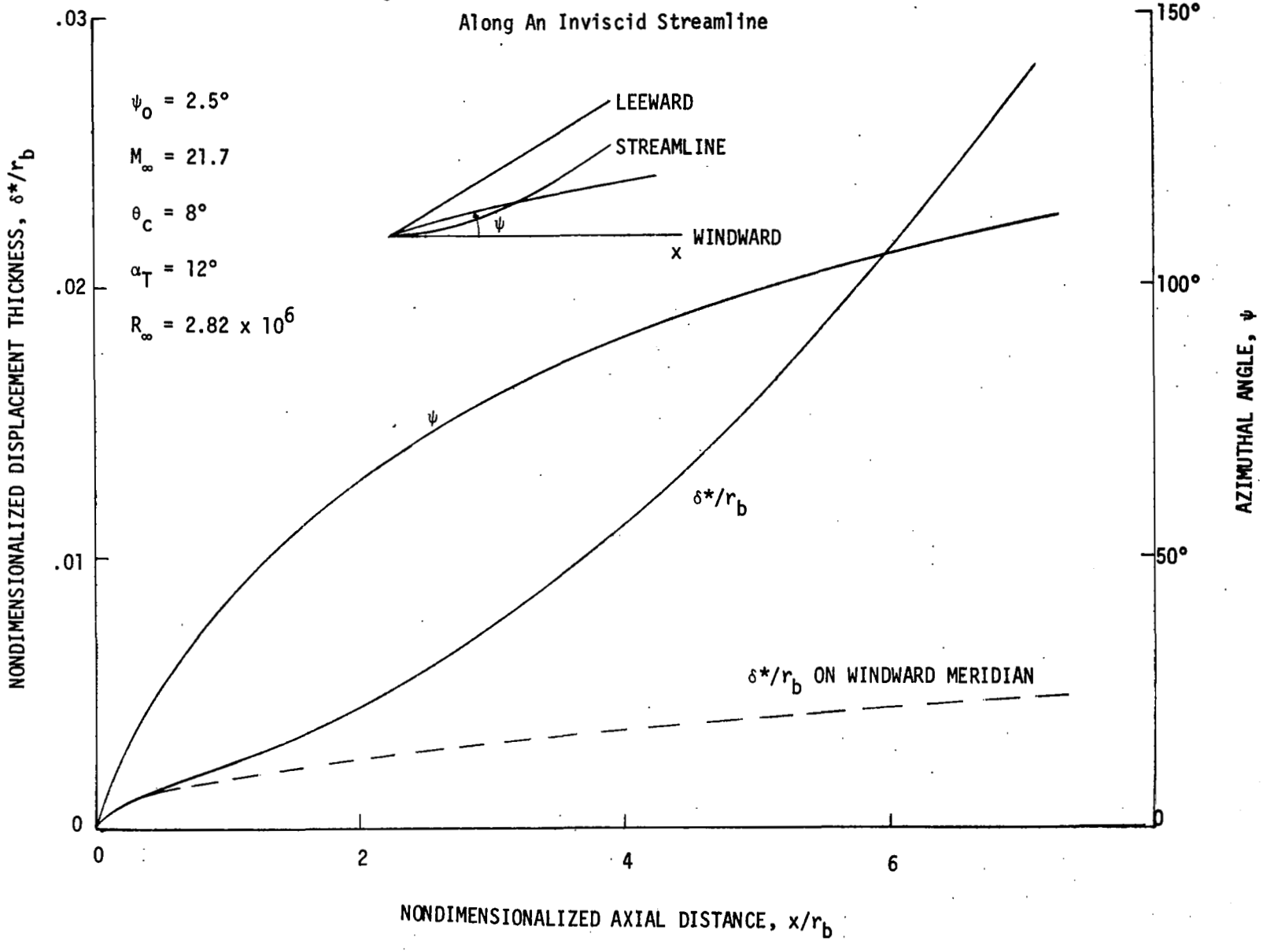

Figure 43. Local Mach Number As A Function of Azimuthal Angle

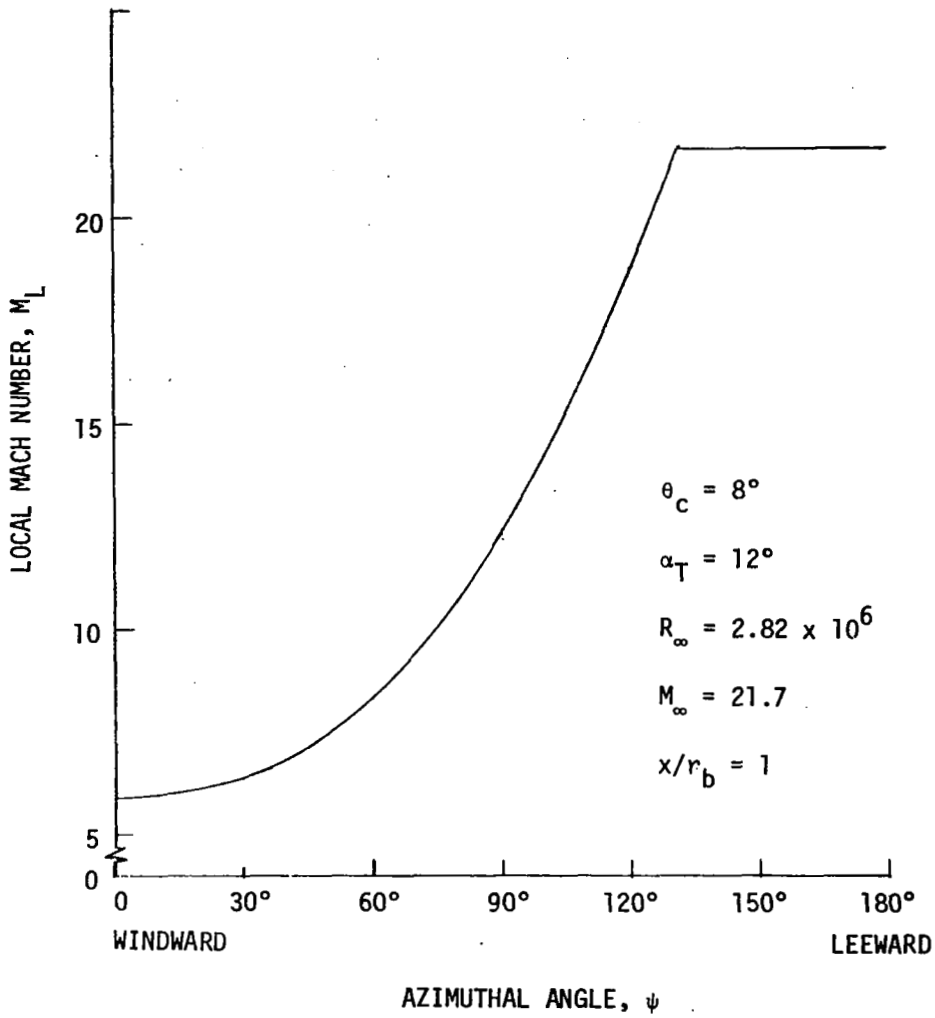

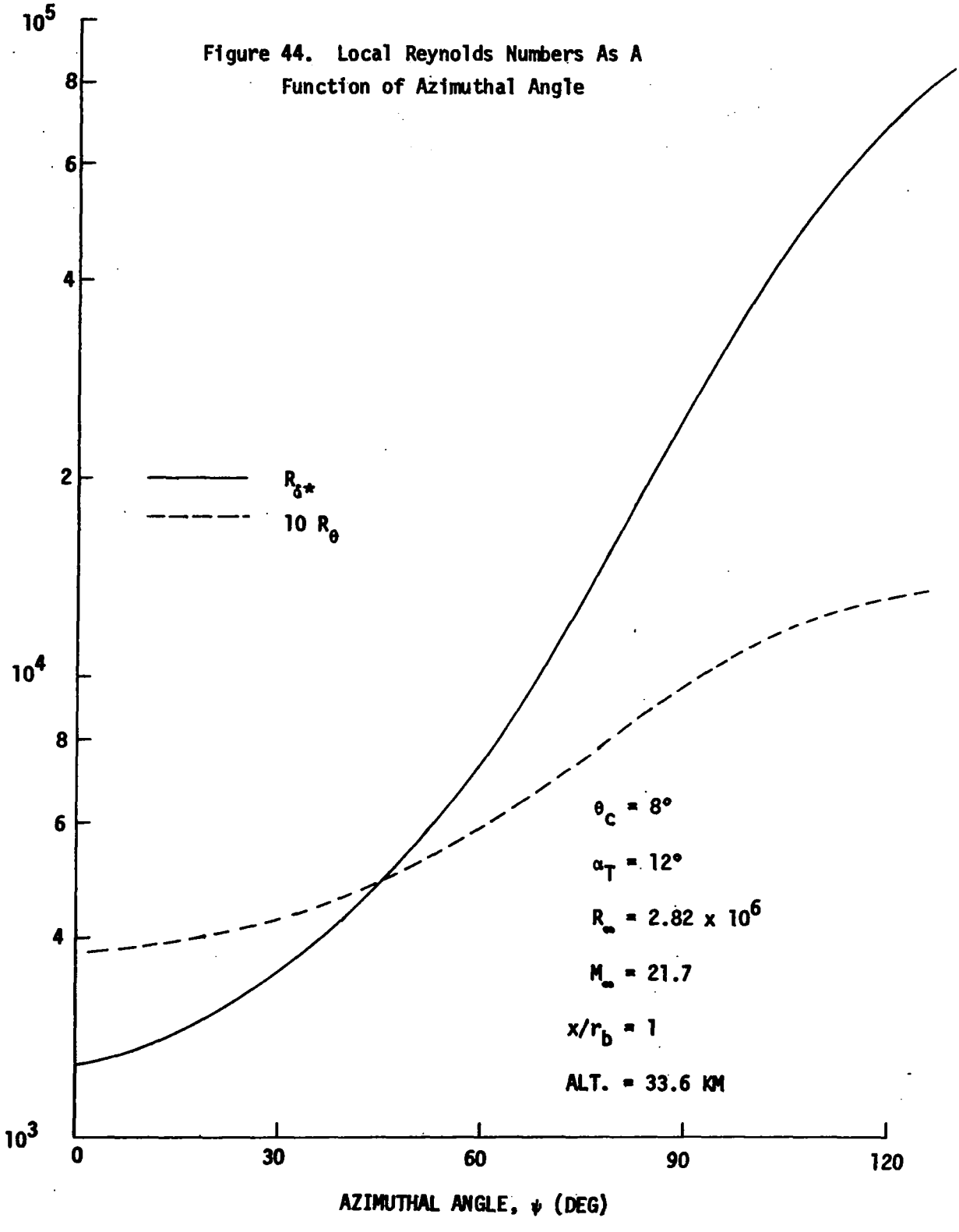

Figure 44. Local Reynolds Numbers As A Function of Azimuthal Angle

Figure 45. Variation of Local Flow Conditions and Corresponding Relation to Presumed Transition Correlations

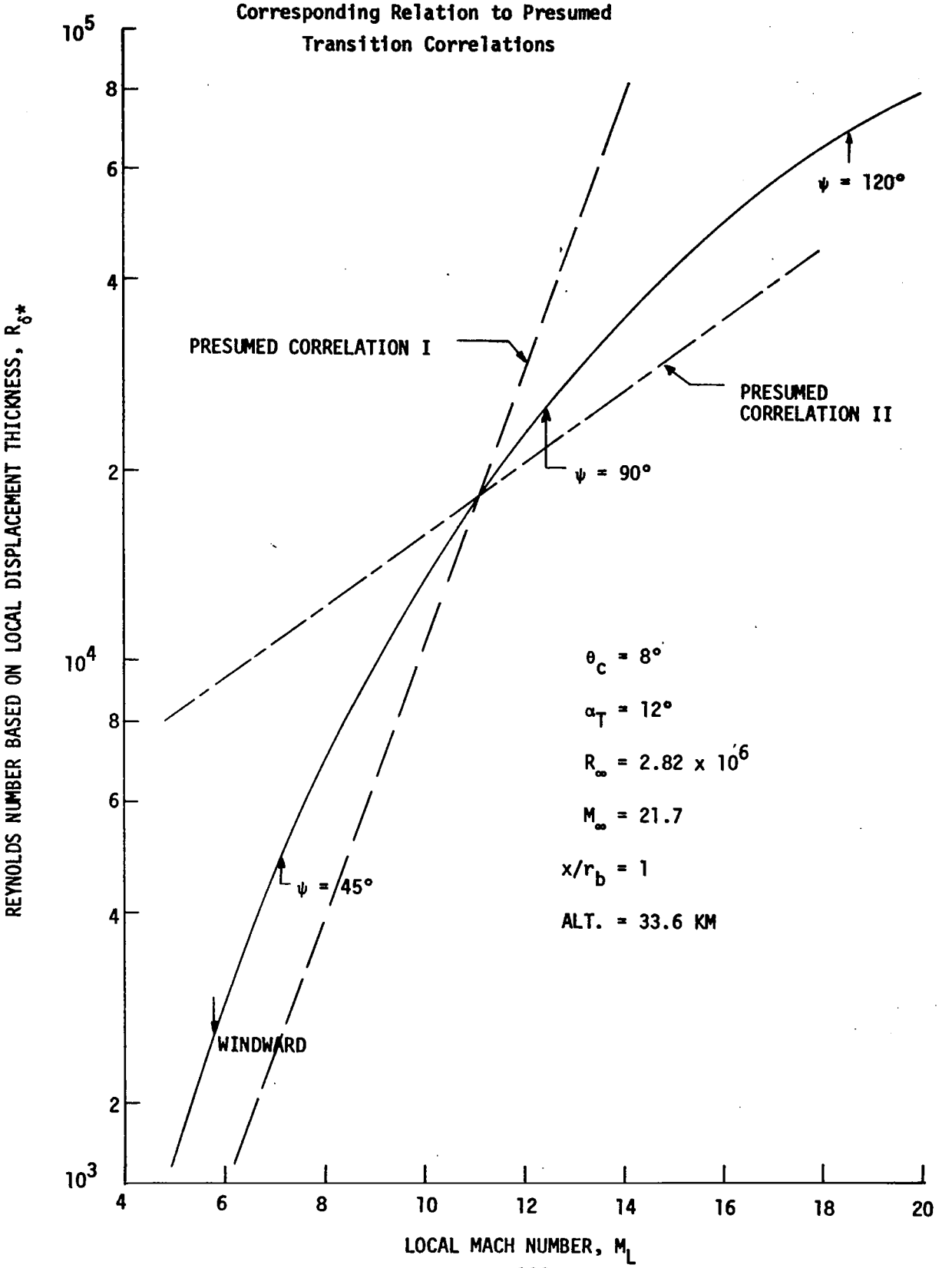

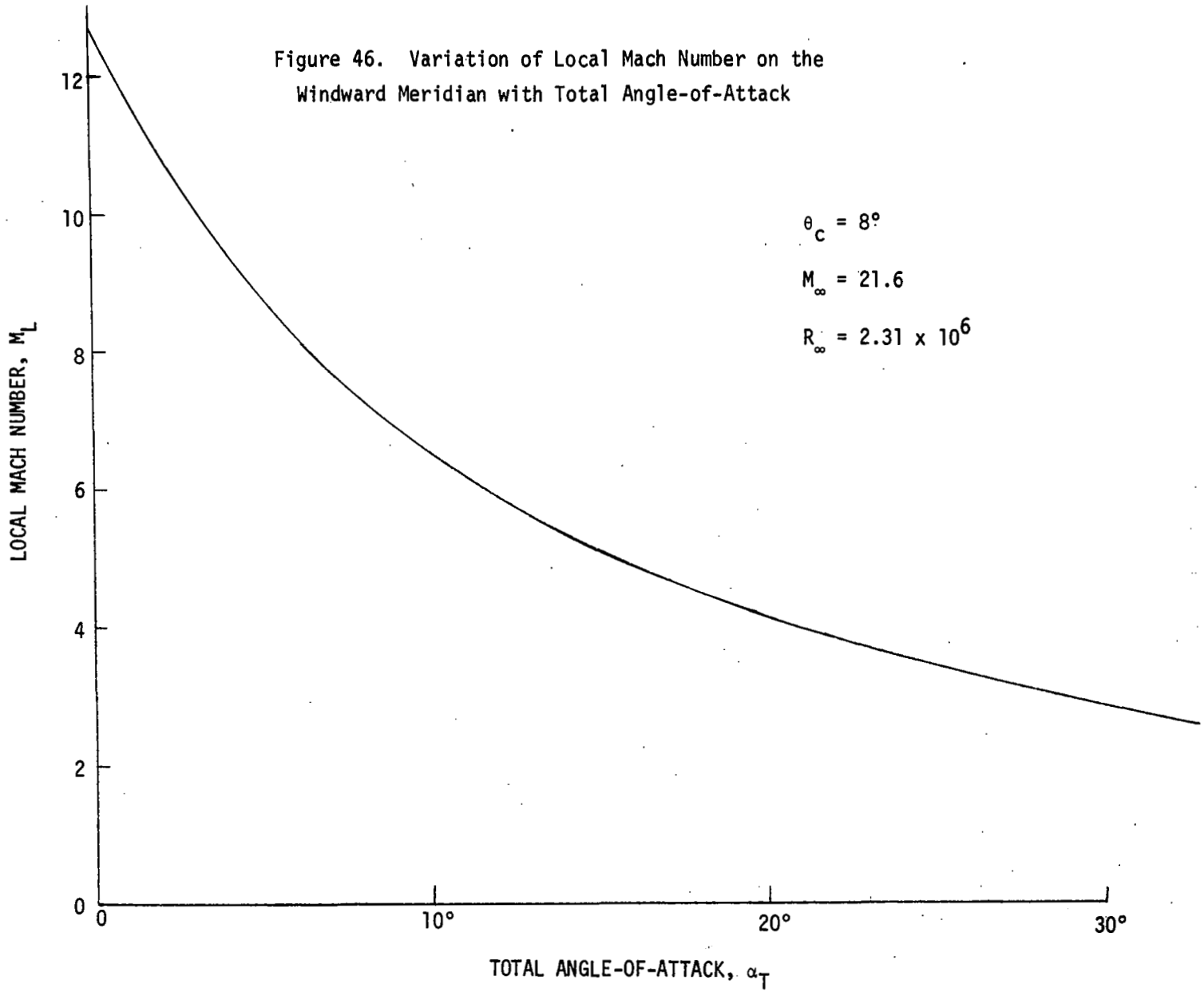

Figure 46. Variation of Local Mach Number on the Windward Meridian with Total Angle-of-Attack

Figure 47. Variation of Local Reynolds Number on the Windward Meridian with Total Angle-of-Attack

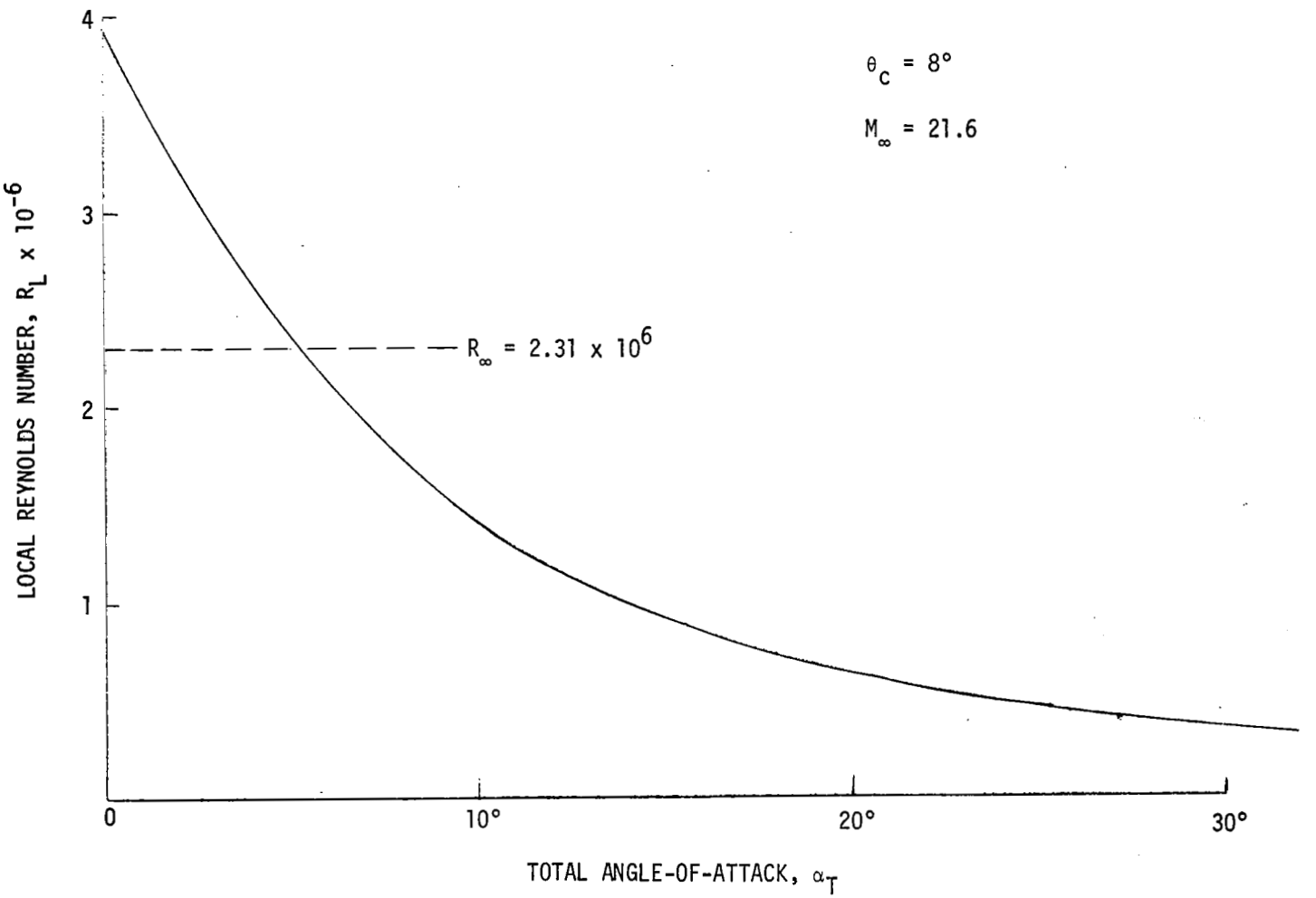

Figure 48. Correlation of Acoustic Sensor Transition Data with R_X Versus M_L

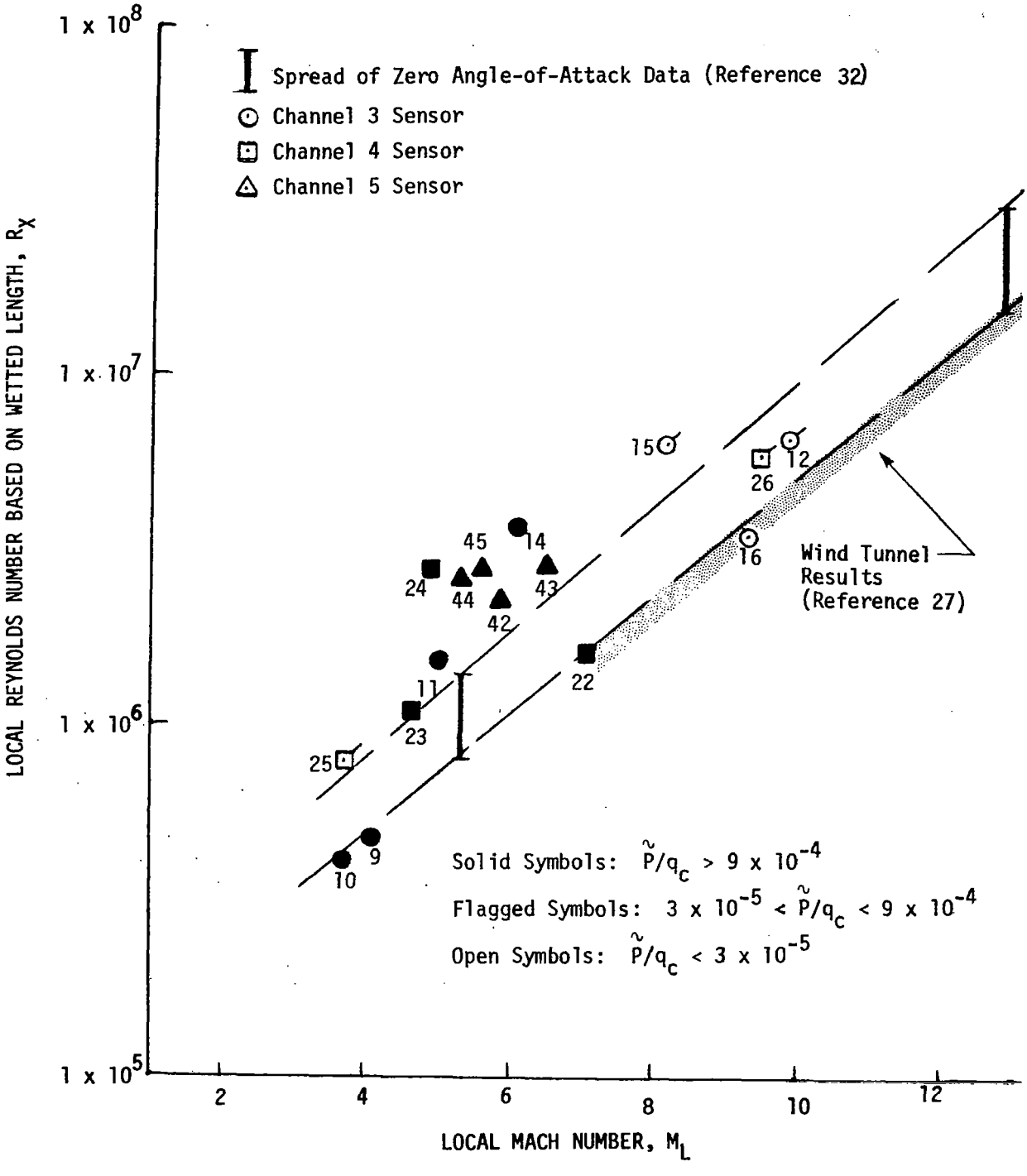

Figure 49. Correlation of Acoustic Sensor Transition Data With R_θ Versus M_L

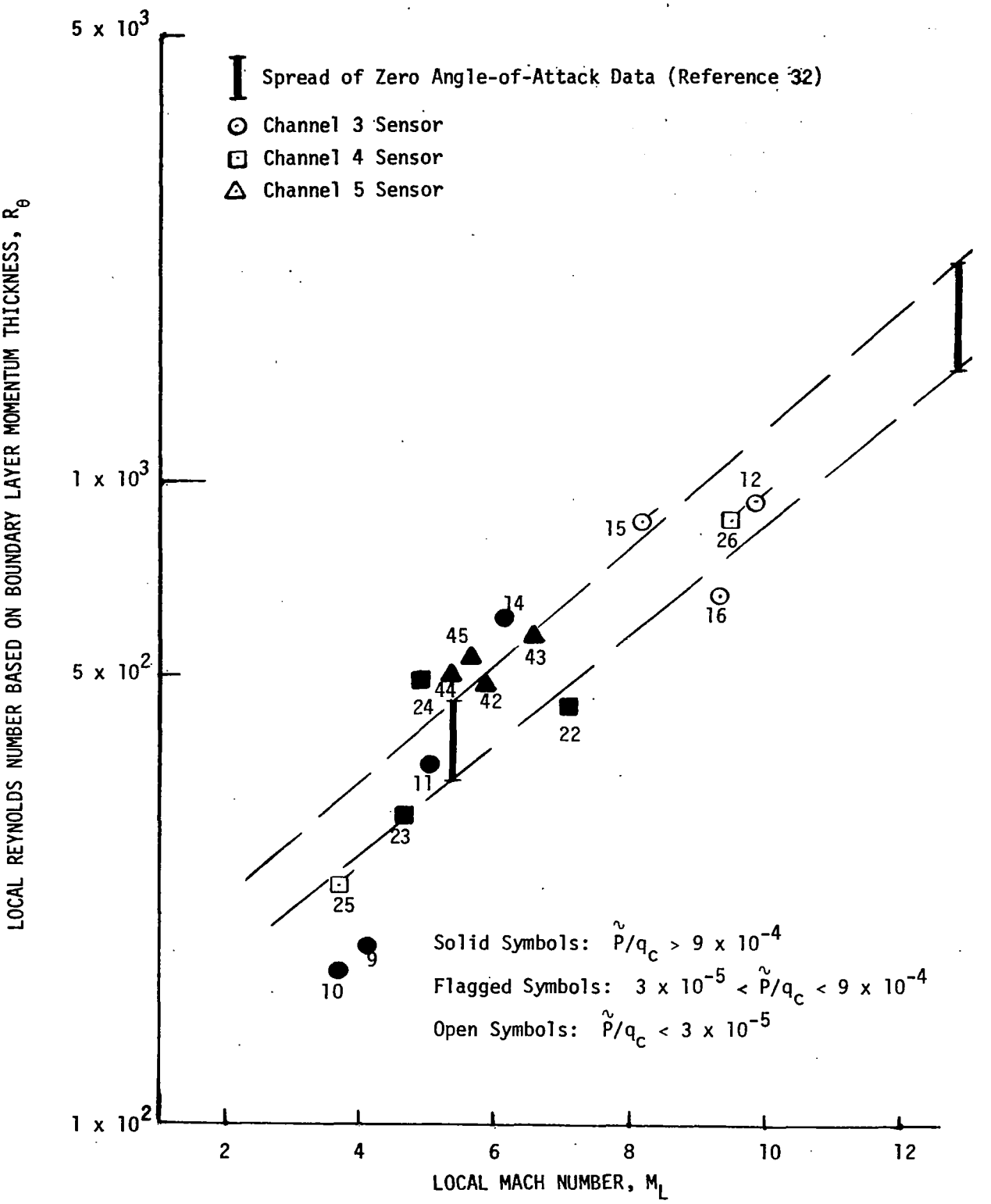

Figure 50. Correlation of Acoustic Sensor Transition Data With R_{δ^*} Versus M_L

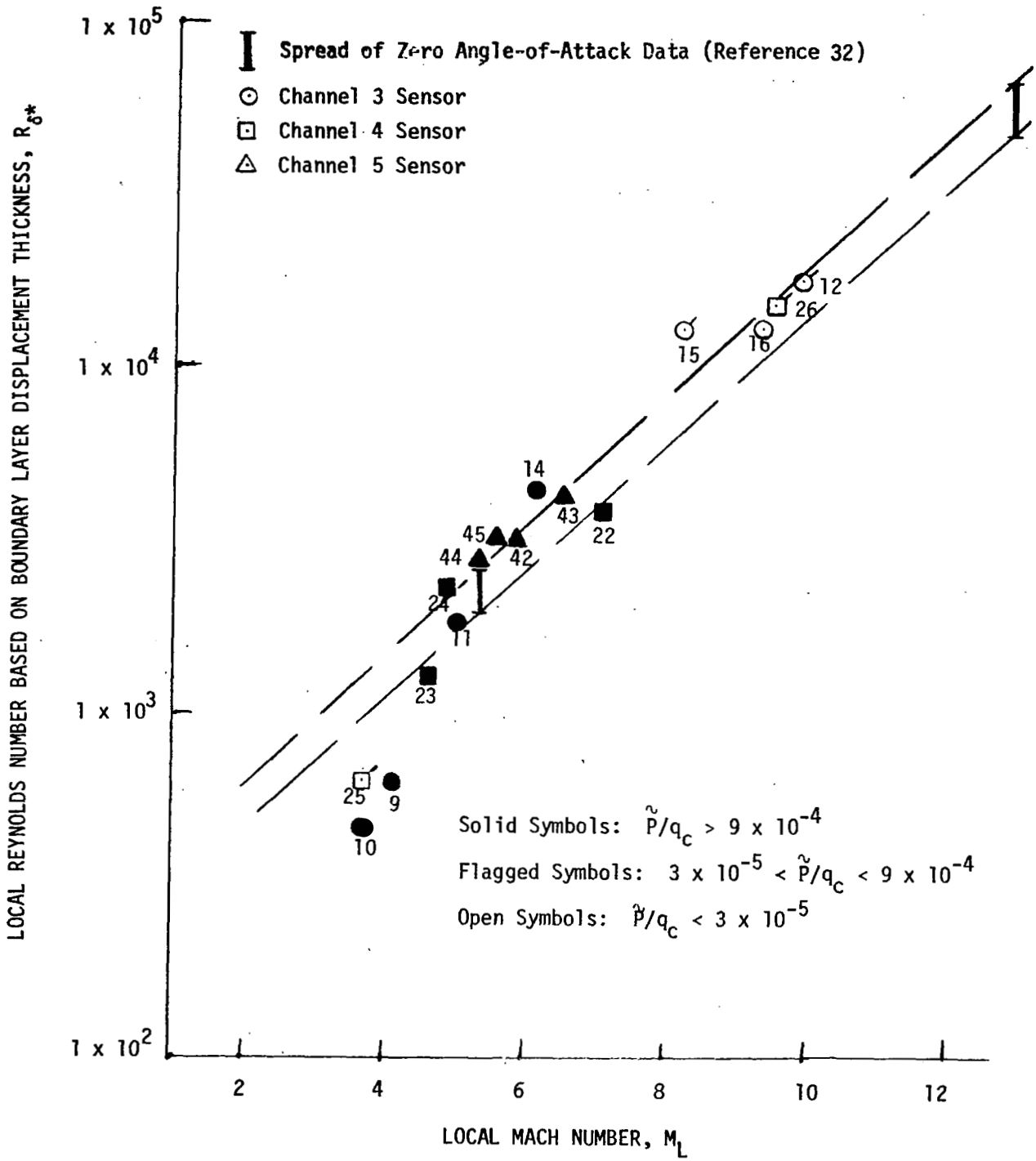

Figure 51. Correlation of Electrostatic Probe Transition Data with R_δ^* Versus M_L

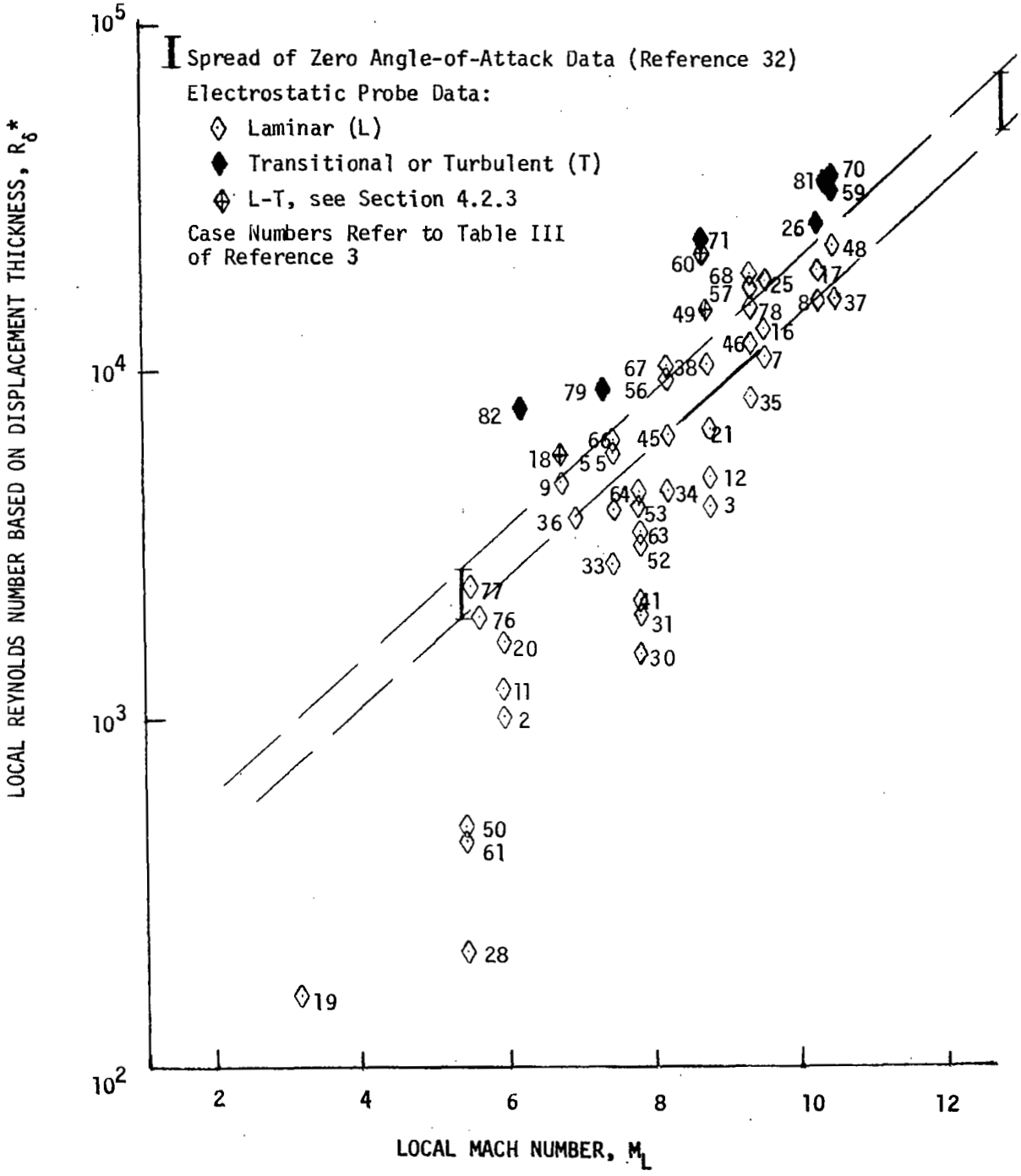

Figure 52. Correlation of Acoustic Sensor and Electrostatic Probe Transition Data with R_δ^* Versus M_L

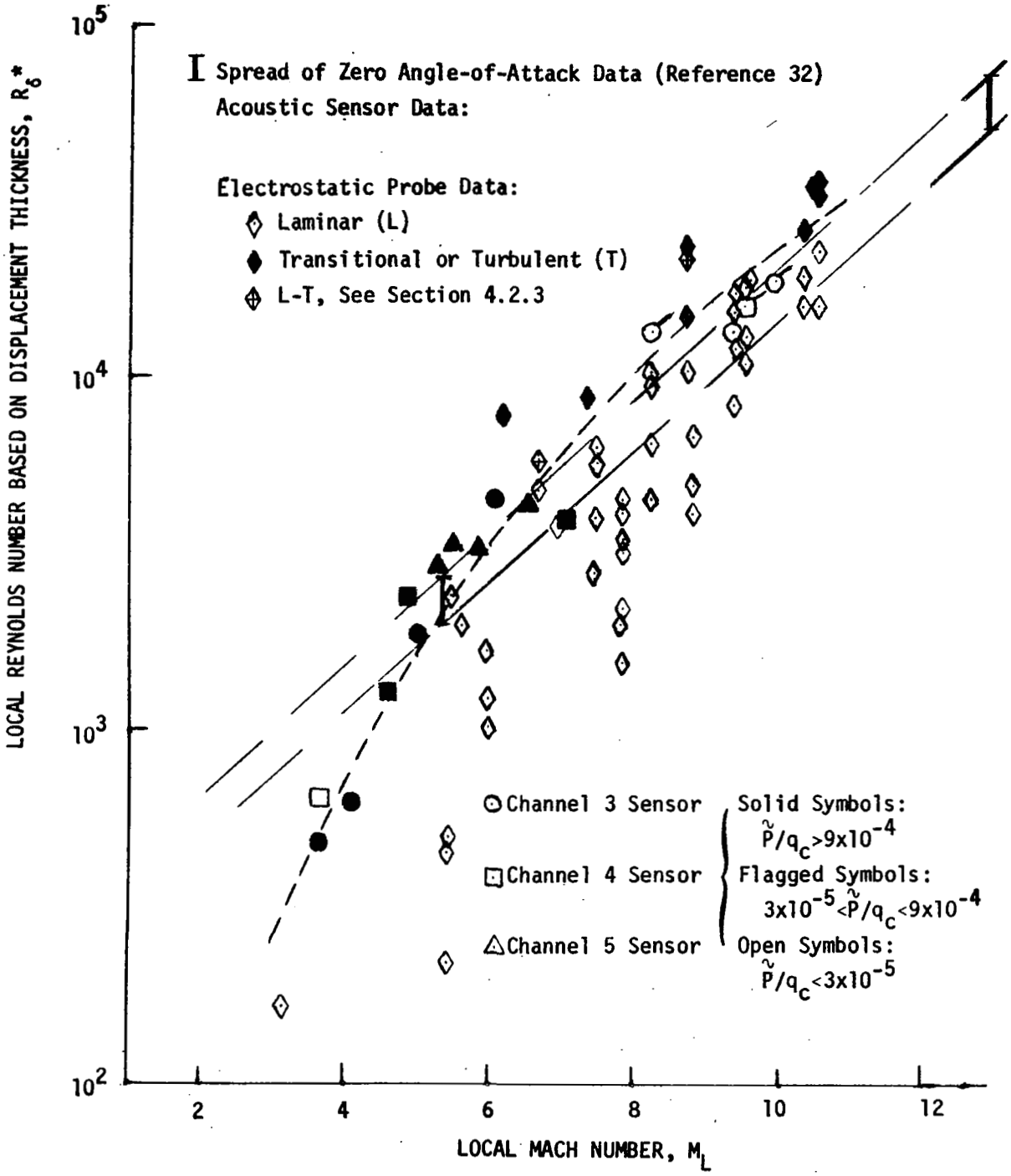

APPENDIX A

FLIGHT 2 THERMOCOUPLE TEMPERATURE HISTORY DATA

Temperature histories of the eight thermocouples on the Flight 2 vehicle are tabulated in this appendix. The temperature data in degrees Fahrenheit are presented as a function of time after liftoff, TALO in seconds. Trajectory support data including the time, altitude, vehicle centerline angle-of-attack, and freestream Mach number, velocity, density, temperature and pressure are presented in Tables I and II of the addendum to this report, Reference 3.

Table AI

Flight 2 Thermocouple Data

Thermocouple No. 145, X = 31.87", ϕ_S = 225°

TALO (SEC)	TEMP (°F)	TALO (SEC)	TEMP (°F)	TALO (SEC)	TEMP (°F)	TALO (SEC)	TEMP (°F)
1608.0	51.71	1611.8	93.59	1614.6	59.10	1617.4	68.96
1609.0	51.71	1611.9	54.17	1614.7	59.10	1617.5	68.96
1609.2	51.71	1612.0	54.17	1614.8	59.10	1617.6	68.96
1609.3	54.17	1612.1	54.17	1614.9	59.10	1617.7	71.42
1609.4	54.17	1612.2	54.17	1615.0	61.57	1617.8	71.42
1609.5	54.17	1612.3	56.64	1615.1	61.57	1617.9	71.42
1609.6	54.17	1612.4	56.64	1615.2	61.57	1618.0	71.42
1609.7	54.17	1612.5	56.64	1615.3	61.57	1618.1	71.42
1609.8	54.17	1612.6	56.64	1615.4	61.57	1618.2	71.42
1609.9	54.17	1612.7	56.64	1615.5	61.57	1618.3	71.42
1610.0	54.17	1612.8	56.64	1615.6	61.57	1618.4	73.88
1610.1	54.17	1612.9	56.64	1615.7	61.57	1618.5	73.88
1610.2	54.17	1613.0	56.64	1615.8	64.03	1618.6	73.88
1610.3	54.17	1613.1	56.64	1615.9	64.03	1618.7	73.88
1610.4	54.17	1613.2	56.64	1616.0	64.03	1618.8	76.35
1610.5	54.17	1613.3	56.64	1616.1	64.03	1618.9	78.81
1610.6	54.17	1613.4	56.64	1616.2	64.03	1619.0	78.81
1610.7	54.17	1613.5	56.64	1616.3	66.49	1619.1	78.81
1610.8	54.17	1613.6	56.64	1616.4	66.49	1619.2	78.81
1610.9	54.17	1613.7	56.64	1616.5	66.49	1619.3	78.81
1611.0	54.17	1613.8	56.64	1616.6	66.49	1619.4	81.28
1611.1	54.17	1613.9	56.64	1616.7	66.49	1619.5	81.28
1611.2	54.17	1614.0	59.10	1616.8	66.49	1619.6	83.74
1611.3	54.17	1614.1	59.10	1616.9	66.49	1619.7	83.74
1611.4	54.17	1614.2	59.10	1617.0	66.49	1619.8	83.74
1611.5	93.59	1614.3	59.10	1617.1	68.96	1619.9	83.74
1611.6	54.17	1614.4	59.10	1617.2	68.96	1620.0	83.74
1611.7	54.17	1614.5	59.10	1617.3	68.96	1620.1	88.67

Table AI (Continued)
Flight 2 Thermocouple Data
Thermocouple No. 145

TALO (SEC)	TEMP (°F)	TALO (SEC)	TEMP (°F)	TALO (SEC)	TEMP (°F)	TALO (SEC)	TEMP (°F)
1620.2	88.67	1623.0	115.40	1625.8	156.32	1628.6	233.33
1620.3	86.20	1623.1	115.40	1625.9	161.13	1628.7	238.15
1620.4	86.20	1623.2	117.81	1626.0	161.13	1628.8	238.15
1620.5	88.67	1623.3	117.81	1626.1	165.95	1628.9	242.96
1620.6	91.13	1623.4	117.81	1626.2	165.95	1629.0	245.37
1620.7	91.13	1623.5	120.22	1626.3	170.76	1629.1	250.18
1620.8	91.13	1623.6	122.62	1626.4	173.17	1629.2	250.18
1620.9	93.59	1623.7	120.22	1626.5	175.57	1629.3	252.59
1621.0	93.59	1623.8	125.03	1626.6	175.57	1629.4	257.40
1621.1	93.59	1623.9	125.03	1626.7	177.98	1629.5	259.81
1621.2	93.59	1624.0	125.03	1626.8	182.79	1629.6	262.21
1621.3	93.59	1624.1	125.03	1626.9	182.79	1629.7	267.03
1621.4	96.06	1624.2	127.44	1627.0	187.61	1629.8	271.84
1621.5	96.06	1624.3	127.44	1627.1	192.42	1629.9	274.25
1621.6	98.52	1624.4	129.84	1627.2	192.42	1630.0	279.06
1621.7	100.96	1624.5	132.25	1627.3	194.83	1630.1	283.88
1621.8	100.96	1624.6	134.66	1627.4	194.83	1630.2	288.69
1621.9	103.37	1624.7	139.47	1627.5	199.64	1630.3	291.10
1622.0	105.78	1624.8	137.06	1627.6	202.05	1630.4	298.31
1622.1	105.78	1624.9	141.88	1627.7	206.86	1630.5	300.74
1622.2	105.78	1625.0	141.88	1627.8	209.27	1630.6	308.10
1622.3	105.78	1625.1	144.28	1627.9	214.08	1630.7	310.55
1622.4	108.18	1625.2	144.28	1628.0	214.08	1630.8	315.46
1622.5	110.59	1625.3	149.10	1628.1	218.89	1630.9	317.91
1622.6	110.59	1625.4	151.50	1628.2	221.30	1631.0	325.28
1622.7	113.00	1625.5	153.91	1628.3	223.71	1631.1	327.73
1622.8	115.40	1625.6	156.32	1628.4	226.11	1631.2	332.64
1622.9	113.00	1625.7	156.32	1628.5	230.93	1631.3	337.55

Table AI (Continued)
Flight 2 Thermocouple Data
Thermocouple No. 145

TALO (SEC)	TEMP (°F)	TALO (SEC)	TEMP (°F)
1631.4	342.45	1634.2	633.17
1631.5	349.82	1634.3	647.49
1631.6	354.72	1634.4	661.81
1631.7	359.63	1634.5	685.68
1631.8	366.99	1634.6	702.34
1631.9	374.36	1634.7	723.36
1632.0	379.26	1634.8	753.74
1632.1	384.17	1634.9	765.42
1632.2	389.08	1635.0	786.45
1632.3	396.44	1635.1	812.15
1632.4	408.71	1635.2	868.22
1632.5	416.07	1635.3	905.57
1632.6	423.44		
1632.7	430.80		
1632.8	440.61		
1632.9	452.88		
1633.0	465.15		
1633.1	484.79		
1633.2	494.60		
1633.3	506.68		
1633.4	521.00		
1633.5	532.94		
1633.6	544.87		
1633.7	559.19		
1633.8	571.12		
1633.9	585.44		
1634.0	602.15		
1634.1	616.47		

Table AI (Continued)

Flight 2 Thermocouple Data

Thermocouple No. 146, X = 77.45", ϕ_S = 225°

TALO (SEC)	TEMP (°F)	TALO (SEC)	TEMP (°F)	TALO (SEC)	TEMP (°F)	TALO (SEC)	TEMP (°F)
1608.0	68.96	1611.7	71.42	1614.5	73.88	1617.3	83.74
1609.0	68.81	1611.8	71.42	1614.6	76.34	1617.4	83.73
1609.1	108.18	1611.9	71.42	1614.7	76.35	1617.5	86.19
1609.2	69.10	1612.0	71.42	1614.8	76.35	1617.6	86.20
1609.3	68.96	1612.1	71.42	1614.9	76.35	1617.7	86.20
1609.4	68.96	1612.2	71.42	1615.0	76.35	1617.8	86.20
1609.5	68.96	1612.3	71.42	1615.1	76.35	1617.9	86.19
1609.6	68.96	1612.4	71.42	1615.2	76.35	1618.0	88.66
1609.7	68.96	1612.5	71.42	1615.3	76.35	1618.1	88.67
1609.8	68.96	1612.6	71.42	1615.4	76.35	1618.2	88.67
1609.9	68.96	1612.7	71.42	1615.5	76.34	1618.3	88.67
1610.0	68.96	1612.8	71.42	1615.6	78.80	1618.4	88.67
1610.1	68.96	1612.9	71.42	1615.7	78.81	1618.5	88.67
1610.2	68.96	1613.0	71.42	1615.8	78.81	1618.6	88.67
1610.3	68.96	1613.1	71.41	1615.9	78.81	1618.7	88.66
1610.4	68.95	1613.2	73.88	1616.0	78.81	1618.8	91.12
1610.5	71.42	1613.3	73.88	1616.1	78.81	1618.9	91.13
1610.6	68.96	1613.4	73.88	1616.2	78.81	1619.0	91.12
1610.7	71.41	1613.5	73.88	1616.3	78.81	1619.1	93.59
1610.8	71.42	1613.6	73.88	1616.4	78.81	1619.2	93.59
1610.9	71.42	1613.7	73.88	1616.5	78.80	1619.3	93.59
1611.0	71.42	1613.8	73.88	1616.6	81.27	1619.4	93.59
1611.1	71.42	1613.9	73.88	1616.7	81.28	1619.5	96.05
1611.2	71.42	1614.0	73.88	1616.8	81.28	1619.6	96.06
1611.3	71.42	1614.1	73.88	1616.9	81.28	1619.7	96.06
1611.4	71.42	1614.2	73.88	1617.0	81.27	1619.8	96.06
1611.5	71.42	1614.3	73.88	1617.1	83.73	1619.9	96.05
1611.6	71.42	1614.4	73.88	1617.2	83.74	1620.0	98.51

Table AI (Continued)

Flight 2 Thermocouple Data

Thermocouple No. 146

TALO (SEC)	TEMP (°F)	TALO (SEC)	TEMP (°F)	TALO (SEC)	TEMP (°F)	TALO (SEC)	TEMP (°F)
1620.1	98.52	1622.9	120.22	1625.7	156.31	1628.5	206.85
1620.2	98.52	1623.0	120.22	1625.8	158.71	1628.6	209.24
1620.3	98.52	1623.1	120.22	1625.9	161.12	1628.7	214.05
1620.4	98.52	1623.2	120.20	1626.0	161.12	1628.8	216.47
1620.5	98.52	1623.3	125.02	1626.1	163.53	1628.9	218.88
1620.6	98.51	1623.4	122.61	1626.2	163.54	1629.0	221.28
1620.7	100.95	1623.5	127.42	1626.3	163.53	1629.1	223.69
1620.8	100.95	1623.6	127.43	1626.4	165.94	1629.2	226.10
1620.9	103.36	1623.7	129.84	1626.5	165.95	1629.3	226.09
1621.0	103.36	1623.8	129.84	1626.6	165.94	1629.4	233.30
1621.1	105.77	1623.9	129.84	1626.7	168.33	1629.5	235.72
1621.2	105.78	1624.0	129.84	1626.8	170.75	1629.6	238.13
1621.3	105.78	1624.1	132.22	1626.9	170.74	1629.7	240.54
1621.4	105.77	1624.2	137.05	1627.0	175.55	1629.8	242.94
1621.5	108.17	1624.3	137.06	1627.1	175.56	1629.9	245.36
1621.6	110.58	1624.4	139.46	1627.2	177.97	1630.0	245.34
1621.7	110.59	1624.5	139.46	1627.3	177.97	1630.1	252.55
1621.8	110.56	1624.6	141.87	1627.4	180.36	1630.2	254.99
1621.9	117.80	1624.7	141.87	1627.5	185.17	1630.3	254.97
1622.0	113.01	1624.8	144.28	1627.6	187.60	1630.4	262.18
1622.1	112.99	1624.9	144.28	1627.7	187.59	1630.5	264.59
1622.2	115.39	1625.0	146.67	1627.8	192.40	1630.6	271.81
1622.3	115.40	1625.1	149.09	1627.9	192.41	1630.7	274.22
1622.4	115.40	1625.2	149.09	1628.0	194.81	1630.8	277.88
1622.5	115.39	1625.3	151.50	1628.1	197.21	1630.9	599.68
1622.6	120.20	1625.4	151.50	1628.2	202.02	1631.0	297.00
1622.7	120.22	1625.5	153.89	1628.3	204.44	1631.1	303.12
1622.8	120.22	1625.6	156.31	1628.4	206.85	1631.2	315.34

Table AI (Continued)

Flight 2 Thermocouple Data

Thermocouple No. 146

TALO (SEC)	TEMP (°F)	TALO (SEC)	TEMP (°F)
1631.3	334.92	1634.1	1140.08
1631.4	361.90	1634.2	1182.34
1631.5	386.43	1634.3	1219.90
1631.6	415.86	1634.4	1259.78
1631.7	445.30	1634.5	1306.80
1631.8	474.71	1634.6	1354.47
1631.9	515.98	1634.7	1404.51
1632.0	542.25	1634.8	1456.97
1632.1	580.44	1634.9	1502.32
1632.2	604.36	1635.0	1558.49
1632.3	628.25	1635.1	1619.57
1632.4	644.96	1635.2	1687.99
1632.5	668.78	1635.3	1760.83
1632.6	697.41		
1632.7	723.20		
1632.8	741.89		
1632.9	767.58		
1633.0	790.93		
1633.1	818.95		
1633.2	846.98		
1633.3	877.36		
1633.4	905.36		
1633.5	933.20		
1633.6	963.34		
1633.7	995.81		
1633.8	1030.59		
1633.9	1067.72		
1634.0	1102.55		

Table AI (continued)

Flight 2 Thermocouple Data

Thermocouple No. 147, X = 123.53", ϕ_S = 225°

TALO (SEC)	TEMP (°F)	TALO (SEC)	TEMP (°F)	TALO (SEC)	TEMP (°F)	TALO (SEC)	TEMP (°F)
1608.0	55.96	1613.1	58.96	1615.9	63.45	1618.7	70.94
1609.0	55.96	1613.2	58.96	1616.0	63.45	1618.8	70.94
1610.0	55.96	1613.3	58.96	1616.1	63.45	1618.9	70.93
1610.6	55.95	1613.4	58.96	1616.2	63.45	1619.0	72.42
1610.7	57.45	1613.5	58.96	1616.3	63.45	1619.1	72.42
1610.8	57.46	1613.6	58.96	1616.4	63.45	1619.2	73.93
1610.9	57.46	1613.7	58.96	1616.5	63.44	1619.3	73.93
1611.0	57.46	1613.8	58.96	1616.6	64.94	1619.4	75.43
1611.1	57.46	1613.9	58.96	1616.7	64.95	1619.5	75.44
1611.2	57.46	1614.0	58.95	1616.8	64.95	1619.6	75.44
1611.3	57.46	1614.1	60.45	1616.9	64.94	1619.7	75.43
1611.4	57.46	1614.2	60.46	1617.0	66.44	1619.8	76.92
1611.5	57.46	1614.3	60.46	1617.1	66.45	1619.9	76.93
1611.6	57.46	1614.4	60.46	1617.2	66.45	1620.0	76.93
1611.7	57.46	1614.5	60.46	1617.3	66.45	1620.1	76.92
1611.8	57.46	1614.6	60.46	1617.4	66.44	1620.2	78.42
1611.9	57.46	1614.7	60.46	1617.5	67.94	1620.3	78.43
1612.0	57.46	1614.8	60.46	1617.6	67.95	1620.4	78.43
1612.1	57.46	1614.9	60.46	1617.7	67.95	1620.5	78.42
1612.2	57.46	1615.0	60.46	1617.8	67.95	1620.6	79.92
1612.3	57.46	1615.1	60.46	1617.9	67.94	1620.7	79.93
1612.4	57.46	1615.2	60.45	1618.0	69.43	1620.8	79.92
1612.5	57.46	1615.3	61.94	1618.1	69.44	1620.9	81.42
1612.6	57.45	1615.4	61.96	1618.2	69.44	1621.0	81.42
1612.7	58.95	1615.5	61.96	1618.3	69.44	1621.1	82.91
1612.8	58.96	1615.6	61.95	1618.4	69.44	1621.2	82.91
1612.9	58.96	1615.7	63.44	1618.5	69.43	1621.3	84.41
1613.0	58.96	1615.8	63.45	1618.6	70.93	1621.4	84.41

Table AI (Continued)
Flight 2 Thermocouple Data
Thermocouple No. 147

TALO (SEC)	TEMP (°F)	TALO (SEC)	TEMP (°F)	TALO (SEC)	TEMP (°F)	TALO (SEC)	TEMP (°F)
1621.5	85.90	1624.3	106.37	1627.1	135.54	1629.9	191.05
1621.6	87.41	1624.4	107.76	1627.2	136.92	1630.0	196.60
1621.7	87.42	1624.5	109.16	1627.3	138.31	1630.1	200.72
1621.8	87.41	1624.6	109.16	1627.4	139.69	1630.2	204.57
1621.9	88.91	1624.7	110.54	1627.5	142.47	1630.3	216.13
1622.0	88.92	1624.8	111.93	1627.6	143.87	1630.4	242.07
1622.1	88.91	1624.9	111.93	1627.7	145.26	1630.5	268.15
1622.2	90.40	1625.0	113.31	1627.8	146.65	1630.6	289.04
1622.3	90.40	1625.1	114.70	1627.9	148.04	1630.7	306.93
1622.4	91.90	1625.2	116.09	1628.0	149.41	1630.8	323.02
1622.5	91.90	1625.3	117.48	1628.1	152.19	1630.9	340.36
1622.6	93.40	1625.4	118.88	1628.2	153.59	1631.0	355.25
1622.7	93.41	1625.5	118.88	1628.3	154.97	1631.1	367.64
1622.8	93.41	1625.6	120.26	1628.4	157.75	1631.2	380.02
1622.9	93.40	1625.7	121.66	1628.5	159.15	1631.3	392.38
1623.0	94.90	1625.8	121.66	1628.6	160.52	1631.4	406.94
1623.1	94.90	1625.9	123.04	1628.7	163.29	1631.5	420.06
1623.2	96.39	1626.0	124.42	1628.8	166.08	1631.6	431.95
1623.3	96.39	1626.1	125.81	1628.9	167.47	1631.7	446.21
1623.4	97.88	1626.2	127.21	1629.0	170.25	1631.8	461.66
1623.5	99.39	1626.3	127.22	1629.1	171.64	1631.9	479.52
1623.6	99.39	1626.4	127.22	1629.2	174.41	1632.0	495.03
1623.7	100.81	1626.5	127.22	1629.3	175.80	1632.1	507.93
1623.8	102.21	1626.6	127.21	1629.4	178.57	1632.2	524.17
1623.9	102.22	1626.7	128.59	1629.5	181.35	1632.3	541.61
1624.0	102.21	1626.8	129.97	1629.6	184.14	1632.4	557.88
1624.1	103.59	1626.9	132.75	1629.7	185.52	1632.5	576.45
1624.2	104.98	1627.0	134.15	1629.8	188.29	1632.6	598.52

Table AI (Continued)
Flight 2 Thermocouple Data
Thermocouple No. 147

TALO (SEC)	TEMP (°F)
1632.7	620.15
1632.8	640.60
1632.9	662.18
1633.0	684.91
1633.1	705.29
1633.2	731.13
1633.3	760.40
1633.4	787.46
1633.5	812.11
1633.6	841.09
1633.7	870.10
1633.8	900.20
1633.9	933.59
1634.0	965.90
1634.1	998.17
1634.2	1033.70
1634.3	1069.25
1634.4	1105.89
1634.5	1148.27
1634.6	1189.66
1634.7	1219.78
1634.8	1220.00
1634.9	1220.00
1635.0	1220.00
1635.1	1220.00
1635.2	1220.00
1635.3	1220.00

Table AI (Continued)

Flight 2 Thermocouple Data

Thermocouple No. 148, X = 169.62", ϕ_S = 225°

TALO (SEC)	TEMP (°F)	TALO (SEC)	TEMP (°F)	TALO (SEC)	TEMP (°F)	TALO (SEC)	TEMP (°F)
1608.0	32.00	1615.4	32.00	1618.2	36.49	1621.0	48.46
1609.0	32.00	1615.5	32.00	1618.3	36.48	1621.1	48.48
1610.0	32.00	1615.6	32.00	1618.4	37.96	1621.2	48.48
1611.0	32.00	1615.7	32.00	1618.5	39.47	1621.3	48.46
1612.0	32.00	1615.8	32.00	1618.6	39.49	1621.4	49.96
1613.0	32.00	1615.9	32.00	1618.7	39.49	1621.5	49.96
1613.2	32.00	1616.0	32.00	1618.8	39.51	1621.6	51.44
1613.3	31.98	1616.1	31.98	1618.9	37.99	1621.7	52.97
1613.4	33.50	1616.2	33.48	1619.0	39.49	1621.8	51.49
1613.5	32.02	1616.3	33.50	1619.1	37.98	1621.9	51.18
1613.6	32.00	1616.4	33.51	1619.2	40.94	1622.0	78.40
1613.7	32.00	1616.5	32.00	1619.3	42.47	1622.1	53.26
1613.8	32.00	1616.6	33.48	1619.4	42.48	1622.2	52.97
1613.9	32.00	1616.7	33.50	1619.5	42.48	1622.3	52.95
1614.0	32.00	1616.8	33.48	1619.6	42.48	1622.4	54.45
1614.1	32.00	1616.9	34.98	1619.7	42.47	1622.5	54.45
1614.2	32.00	1617.0	35.00	1619.8	43.98	1622.6	55.95
1614.3	32.00	1617.1	35.00	1619.9	42.50	1622.7	55.95
1614.4	32.00	1617.2	34.98	1620.0	42.47	1622.8	57.46
1614.5	32.00	1617.3	36.49	1620.1	43.97	1622.9	55.97
1614.6	32.00	1617.4	35.01	1620.2	43.98	1623.0	57.45
1614.7	32.00	1617.5	34.98	1620.3	43.97	1623.1	57.46
1614.8	32.00	1617.6	36.46	1620.4	45.46	1623.2	57.45
1614.9	32.00	1617.7	37.99	1620.5	45.48	1623.3	58.91
1615.0	32.00	1617.8	36.51	1620.6	45.48	1623.4	61.92
1615.1	32.00	1617.9	36.49	1620.7	45.46	1623.5	61.96
1615.2	32.00	1618.0	36.49	1620.8	46.96	1623.6	61.96
1615.3	32.00	1618.1	36.49	1620.9	46.96	1623.7	61.94

Table AI (Continued)
Flight 2 Thermocouple Data
Thermocouple No. 148

TALO (SEC)	TEMP (°F)	TALO (SEC)	TEMP (°F)	TALO (SEC)	TEMP (°F)	TALO (SEC)	TEMP (°F)
1623.8	63.44	1626.6	87.40	1629.4	134.02	1632.2	468.71
1623.9	63.45	1626.7	87.92	1629.5	143.72	1632.3	483.02
1624.0	63.42	1626.8	179.92	1629.6	149.31	1632.4	497.25
1624.1	66.42	1626.9	92.89	1629.7	156.13	1632.5	517.02
1624.2	66.43	1627.0	93.38	1629.8	172.69	1632.6	535.63
1624.3	67.91	1627.1	94.89	1629.9	189.37	1632.7	555.39
1624.4	69.43	1627.2	94.89	1630.0	204.39	1632.8	574.00
1624.5	69.43	1627.3	96.36	1630.1	216.16	1632.9	593.75
1624.6	70.93	1627.4	99.35	1630.2	226.59	1633.0	613.21
1624.7	70.94	1627.5	100.80	1630.3	236.98	1633.1	632.49
1624.8	70.91	1627.6	102.21	1630.4	250.00	1633.2	655.17
1624.9	73.89	1627.7	102.21	1630.5	260.46	1633.3	679.03
1625.0	75.42	1627.8	103.60	1630.6	269.56	1633.4	701.76
1625.1	75.44	1627.9	103.60	1630.7	281.25	1633.5	724.27
1625.2	75.42	1628.0	104.94	1630.8	292.97	1633.6	747.90
1625.3	76.90	1628.1	109.12	1630.9	304.45	1633.7	771.52
1625.4	78.40	1628.2	109.14	1631.0	315.61	1633.8	798.50
1625.5	79.91	1628.3	111.90	1631.1	325.54	1633.9	826.43
1625.6	79.93	1628.4	113.32	1631.2	334.18	1634.0	851.00
1625.7	79.90	1628.5	113.32	1631.3	346.51	1634.1	877.75
1625.8	82.89	1628.6	114.68	1631.4	358.90	1634.2	905.60
1625.9	82.91	1628.7	117.45	1631.5	370.05	1634.3	935.65
1626.0	84.41	1628.8	118.86	1631.6	381.16	1634.4	964.58
1626.1	84.41	1628.9	120.22	1631.7	394.73	1634.5	996.86
1626.2	85.90	1629.0	124.40	1631.8	410.38	1634.6	1026.85
1626.3	85.92	1629.1	124.42	1631.9	424.70	1634.7	1061.25
1626.4	85.90	1629.2	127.16	1632.0	437.79	1634.8	1094.62
1626.5	87.40	1629.3	129.92	1632.1	452.04	1634.9	1125.80

Table AI (Continued)

Flight 2 Thermocouple Data

Thermocouple No. 148

TALO (SEC)	TEMP (°F)
1635.0	1163.69
1635.1	1200.73
1635.2	1219.79
1635.3	1220.00

Table AI (Continued)

Flight 2 Thermocouple Data

Thermocouple No. 149, X = 31.87", ϕ_S = 315°

TALO (SEC)	TEMP (°F)	TALO (SEC)	TEMP (°F)	TALO (SEC)	TEMP (°F)	TALO (SEC)	TEMP (°F)
1608.0	49.25	1611.3	51.71	1614.1	56.60	1616.9	64.03
1608.6	49.25	1611.4	51.71	1614.2	56.64	1617.0	66.46
1608.7	49.21	1611.5	51.71	1614.3	56.64	1617.1	66.49
1608.8	51.71	1611.6	51.71	1614.4	56.64	1617.2	66.49
1608.9	49.28	1611.7	51.71	1614.5	56.64	1617.3	66.49
1609.0	49.21	1611.8	51.71	1614.6	56.08	1617.4	66.46
1609.1	51.71	1611.9	51.71	1614.7	96.02	1617.5	68.92
1609.2	49.28	1612.0	51.71	1614.8	57.23	1617.6	68.96
1609.3	49.21	1612.1	51.71	1614.9	56.64	1617.7	68.92
1609.4	51.67	1612.2	51.68	1615.0	56.60	1617.8	71.38
1609.5	51.71	1612.3	54.14	1615.1	59.06	1617.9	71.42
1609.6	51.71	1612.4	54.17	1615.2	59.10	1618.0	71.42
1609.7	51.71	1612.5	54.17	1615.3	59.10	1618.1	71.39
1609.8	51.71	1612.6	54.17	1615.4	59.10	1618.2	73.85
1609.9	51.71	1612.7	54.17	1615.5	59.10	1618.3	73.88
1610.0	51.71	1612.8	54.17	1615.6	59.07	1618.4	73.88
1610.1	51.71	1612.9	54.17	1615.7	61.53	1618.5	73.88
1610.2	51.71	1613.0	54.17	1615.8	61.57	1618.6	73.88
1610.3	51.71	1613.1	54.17	1615.9	61.57	1618.7	73.88
1610.4	51.71	1613.2	54.17	1616.0	61.53	1618.8	73.85
1610.5	51.71	1613.3	54.17	1616.1	63.99	1618.9	76.31
1610.6	51.71	1613.4	54.17	1616.2	64.03	1619.0	76.35
1610.7	51.71	1613.5	54.17	1616.3	64.03	1619.1	76.31
1610.8	51.71	1613.6	54.17	1616.4	64.03	1619.2	78.74
1610.9	51.71	1613.7	54.17	1616.5	63.99	1619.3	81.24
1611.0	51.71	1613.8	54.17	1616.6	66.46	1619.4	81.28
1611.1	51.71	1613.9	54.17	1616.7	66.49	1619.5	81.28
1611.2	51.71	1614.0	54.14	1616.8	66.53	1619.6	81.28

Table AI (Continued)
Flight 2 Thermocouple Data
Thermocouple No. 149

TALO (SEC)	TEMP (°F)	TALO (SEC)	TEMP (°F)	TALO (SEC)	TEMP (°F)	TALO (SEC)	TEMP (°F)
1619.7	81.28	1622.5	108.11	1625.3	151.43	1628.1	209.16
1619.8	81.28	1622.6	110.55	1625.4	153.88	1628.2	214.01
1619.9	81.24	1622.7	110.59	1625.5	153.91	1628.3	214.05
1620.0	83.70	1622.8	110.59	1625.6	153.91	1628.4	216.35
1620.1	83.70	1622.9	110.59	1625.7	153.88	1628.5	223.60
1620.2	86.17	1623.0	110.55	1625.8	156.21	1628.6	223.67
1620.3	86.20	1623.1	112.96	1625.9	161.02	1628.7	225.97
1620.4	86.17	1623.2	113.00	1626.0	163.50	1628.8	233.22
1620.5	88.63	1623.3	112.96	1626.1	163.50	1628.9	233.27
1620.6	88.67	1623.4	115.30	1626.2	165.87	1629.0	238.01
1620.7	88.63	1623.5	120.14	1626.3	168.28	1629.1	242.89
1620.8	91.09	1623.6	120.18	1626.4	170.72	1629.2	242.89
1620.9	91.13	1623.7	122.59	1626.5	170.72	1629.3	247.60
1621.0	91.13	1623.8	122.59	1626.6	173.09	1629.4	254.85
1621.1	91.10	1623.9	124.99	1626.7	175.50	1629.5	257.36
1621.2	93.52	1624.0	125.03	1626.8	177.91	1629.6	257.33
1621.3	96.02	1624.1	124.96	1626.9	180.35	1629.7	262.11
1621.4	96.02	1624.2	129.74	1627.0	180.35	1629.8	264.52
1621.5	98.48	1624.3	132.18	1627.1	182.72	1629.9	269.29
1621.6	98.52	1624.4	134.62	1627.2	185.13	1630.0	274.14
1621.7	98.49	1624.5	134.62	1627.3	187.50	1630.1	276.58
1621.8	100.93	1624.6	137.03	1627.4	192.35	1630.2	278.96
1621.9	100.93	1624.7	137.03	1627.5	192.39	1630.3	283.73
1622.0	103.30	1624.8	139.40	1627.6	194.72	1630.4	288.55
1622.1	105.77	1624.9	141.81	1627.7	199.57	1630.5	293.36
1622.2	103.41	1625.0	144.21	1627.8	199.61	1630.6	298.17
1622.3	103.33	1625.1	146.62	1627.9	201.94	1630.7	303.05
1622.4	105.71	1625.2	149.03	1628.0	206.75	1630.8	307.95

Table AI (Continued)
Flight 2 Thermocouple Data
Thermocouple No. 149

TALO (SEC)	TEMP (°F)	TALO (SEC)	TEMP (°F)
1630.9	312.86	1633.7	544.48
1631.0	317.77	1633.8	556.42
1631.1	322.71	1633.9	570.74
1631.2	325.17	1634.0	582.60
1631.3	330.01	1634.1	601.66
1631.4	337.40	1634.2	616.12
1631.5	339.93	1634.3	625.60
1631.6	342.28	1634.4	644.58
1631.7	352.05	1634.5	661.39
1631.8	357.03	1634.6	673.19
1631.9	361.91	1634.7	699.44
1632.0	369.23	1634.8	711.14
1632.1	376.63	1634.9	736.73
1632.2	381.57	1635.0	755.69
1632.3	386.45	1635.1	762.75
1632.4	393.77	1635.2	778.99
1632.5	401.10	1635.3	793.01
1632.6	410.84		
1632.7	423.15		
1632.8	430.51		
1632.9	442.74		
1633.0	452.60		
1633.1	462.38		
1633.2	474.61		
1633.3	486.88		
1633.4	499.12		
1633.5	513.39		
1633.6	530.09		

Table AI (Continued)
Flight 2 Thermocouple Data
Thermocouple No. 150, X = 77.45", ϕ_S = 315°

TALO (SEC)	TEMP (°F)	TALO (SEC)	TEMP (°F)	TALO (SEC)	TEMP (°F)	TALO (SEC)	TEMP (°F)
1608.0	68.96	1611.6	71.42	1614.4	76.35	1617.2	83.74
1608.9	68.96	1611.7	71.42	1614.5	76.35	1617.3	81.28
1609.0	68.91	1611.8	71.42	1614.6	76.35	1617.4	83.69
1609.1	71.37	1611.9	71.42	1614.7	76.35	1617.5	83.74
1609.2	71.42	1612.0	71.42	1614.8	76.35	1617.6	83.74
1609.3	71.42	1612.1	71.42	1614.9	76.35	1617.7	83.74
1609.4	71.42	1612.2	71.42	1615.0	76.35	1617.8	83.70
1609.5	71.42	1612.3	71.42	1615.1	76.35	1617.9	86.16
1609.6	71.42	1612.4	73.84	1615.2	76.30	1618.0	86.20
1609.7	71.42	1612.5	73.88	1615.3	78.76	1618.1	86.16
1609.8	71.42	1612.6	73.88	1615.4	78.81	1618.2	88.66
1609.9	71.42	1612.7	73.88	1615.5	78.81	1618.3	86.21
1610.0	71.42	1612.8	73.88	1615.6	78.81	1618.4	88.58
1610.1	71.42	1612.9	73.88	1615.7	78.81	1618.5	91.13
1610.2	71.42	1613.0	73.88	1615.8	78.81	1618.6	88.67
1610.3	71.42	1613.1	73.88	1615.9	78.81	1618.7	91.13
1610.4	71.42	1613.2	73.88	1616.0	78.81	1618.8	88.71
1610.5	71.42	1613.3	73.88	1616.1	78.81	1618.9	88.62
1610.6	71.42	1613.4	73.88	1616.2	78.81	1619.0	91.08
1610.7	71.42	1613.5	73.88	1616.3	78.81	1619.1	91.13
1610.8	71.42	1613.6	73.88	1616.4	81.23	1619.2	91.13
1610.9	71.42	1613.7	73.88	1616.5	81.23	1619.3	91.09
1611.0	71.42	1613.8	73.88	1616.6	81.23	1619.4	93.55
1611.1	71.42	1613.9	73.88	1616.7	81.23	1619.5	93.59
1611.2	71.42	1614.0	73.84	1616.8	81.23	1619.6	93.55
1611.3	71.42	1614.1	76.30	1616.9	81.23	1619.7	96.01
1611.4	71.42	1614.2	76.35	1617.0	81.23	1619.8	96.06
1611.5	71.42	1614.3	76.35	1617.1	81.23	1619.9	96.01

Table AI (Continued)
Flight 2 Thermocouple Data
Thermocouple No. 150

TALO (SEC)	TEMP (°F)	TALO (SEC)	TEMP (°F)	TALO (SEC)	TEMP (°F)	TALO (SEC)	TEMP (°F)
1620.0	98.47	1622.8	122.62	1625.6	156.27	1628.4	213.99
1620.1	98.52	1622.9	122.58	1625.7	156.28	1628.5	213.99
1620.2	98.52	1623.0	124.98	1625.8	158.64	1628.6	218.76
1620.3	98.52	1623.1	125.03	1625.9	161.04	1628.7	221.25
1620.4	98.48	1623.2	125.03	1626.0	163.49	1628.8	221.22
1620.5	100.92	1623.3	124.99	1626.1	163.54	1628.9	226.02
1620.6	100.96	1623.4	127.39	1626.2	163.50	1629.0	226.07
1620.7	100.92	1623.5	127.39	1626.3	165.86	1629.1	228.39
1620.8	103.32	1623.6	129.80	1626.4	168.26	1629.2	233.24
1620.9	103.37	1623.7	129.80	1626.5	170.67	1629.3	233.29
1621.0	103.37	1623.8	132.21	1626.6	173.08	1629.4	235.65
1621.1	103.37	1623.9	132.25	1626.7	175.48	1629.5	238.02
1621.2	103.33	1624.0	132.21	1626.8	177.85	1629.6	242.87
1621.3	105.73	1624.1	134.61	1626.9	182.70	1629.7	242.88
1621.4	105.78	1624.2	134.66	1627.0	182.79	1629.8	247.64
1621.5	105.73	1624.3	134.66	1627.1	182.75	1629.9	250.05
1621.6	108.14	1624.4	134.62	1627.2	185.11	1630.0	254.86
1621.7	108.14	1624.5	136.98	1627.3	187.56	1630.1	257.31
1621.8	110.54	1624.6	139.38	1627.4	187.52	1630.2	259.63
1621.9	110.55	1624.7	141.79	1627.5	192.33	1630.3	266.89
1622.0	112.91	1624.8	144.28	1627.6	192.38	1630.4	266.94
1622.1	115.36	1624.9	141.84	1627.7	194.70	1630.5	271.62
1622.2	115.36	1625.0	146.60	1627.8	199.55	1630.6	278.88
1622.3	117.76	1625.1	146.69	1627.9	199.60	1630.7	281.42
1622.4	117.77	1625.2	146.61	1628.0	201.96	1630.8	281.34
1622.5	120.17	1625.3	151.41	1628.1	204.32	1630.9	288.42
1622.6	120.17	1625.4	151.46	1628.2	209.17	1631.0	295.69
1622.7	122.58	1625.5	153.82	1628.3	209.18	1631.1	300.51

Table AI (Continued)

Flight 2 Thermocouple Data

Thermocouple No. 150

TALO (SEC)	TEMP (°F)	TALO (SEC)	TEMP (°F)
1631.2	307.66	1634.0	1122.57
1631.3	324.47	1634.1	1160.04
1631.4	351.19	1634.2	1202.29
1631.5	382.53	1634.3	1239.90
1631.6	441.30	1634.4	1279.58
1631.7	478.66	1634.5	1329.20
1631.8	508.05	1634.6	1376.87
1631.9	534.44	1634.7	1426.80
1632.0	556.06	1634.8	1481.61
1632.1	575.20	1634.9	1532.51
1632.2	594.12	1635.0	1588.56
1632.3	622.62	1635.1	1649.45
1632.4	648.92	1635.2	
1632.5	675.17		
1632.6	701.43		
1632.7	724.84		
1632.8	748.25		
1632.9	769.16		
1633.0	799.31		
1633.1	832.10		
1633.2	857.90		
1633.3	885.81		
1633.4	918.34		
1633.5	948.55		
1633.6	978.59		
1633.7	1015.66		
1633.8	1048.15		
1633.9	1085.18		

Table AI (Continued)

Flight 2 Thermocouple Data

Thermocouple No. 151, X = 123.53", ϕ_S = 315°

TALO (SEC)	TEMP (°F)	TALO (SEC)	TEMP (°F)	TALO (SEC)	TEMP (°F)	TALO (SEC)	TEMP (°F)
1608.0	61.57	1611.6	64.03	1614.4	66.44	1617.2	71.37
1608.9	61.51	1611.7	64.03	1614.5	68.90	1617.3	73.83
1609.0	63.97	1611.8	64.03	1614.6	68.96	1617.4	73.88
1609.1	64.08	1611.9	64.03	1614.7	68.96	1617.5	73.88
1609.2	61.57	1612.0	64.03	1614.8	68.96	1617.6	73.88
1609.3	63.97	1612.1	64.03	1614.9	68.96	1617.7	73.88
1609.4	64.03	1612.2	64.03	1615.0	68.96	1617.8	73.83
1609.5	64.03	1612.3	64.03	1615.1	68.96	1617.9	76.29
1609.6	64.03	1612.4	64.03	1615.2	68.96	1618.0	76.35
1609.7	64.03	1612.5	64.03	1615.3	68.96	1618.1	76.35
1609.8	64.03	1612.6	64.03	1615.4	68.96	1618.2	76.35
1609.9	64.03	1612.7	64.03	1615.5	68.96	1618.3	76.35
1610.0	64.03	1612.8	64.03	1615.6	68.96	1618.4	76.35
1610.1	64.03	1612.9	63.98	1615.7	68.96	1618.5	76.30
1610.2	64.03	1613.0	66.44	1615.8	68.96	1618.6	78.76
1610.3	64.03	1613.1	66.49	1615.9	68.96	1618.7	78.81
1610.4	64.03	1613.2	66.49	1616.0	68.96	1618.8	78.81
1610.5	64.03	1613.3	66.49	1616.1	68.90	1618.9	78.81
1610.6	64.03	1613.4	66.49	1616.2	71.36	1619.0	78.81
1610.7	64.03	1613.5	66.49	1616.3	71.42	1619.1	78.81
1610.8	64.03	1613.6	66.49	1616.4	71.42	1619.2	78.81
1610.9	64.03	1613.7	66.49	1616.5	71.42	1619.3	78.76
1611.0	64.03	1613.8	66.49	1616.6	71.42	1619.4	81.22
1611.1	64.03	1613.9	66.49	1616.7	71.42	1619.5	81.28
1611.2	64.03	1614.0	66.49	1616.8	71.42	1619.6	81.22
1611.3	64.03	1614.1	66.49	1616.9	71.42	1619.7	83.68
1611.4	64.03	1614.2	66.49	1617.0	71.42	1619.8	83.74
1611.5	64.03	1614.3	66.49	1617.1	71.42	1619.9	83.74

Table AI (Continued)

Flight 2 Thermocouple Data

Thermocouple No. 151

TALO (SEC)	TEMP (°F)	TALO (SEC)	TEMP (°F)	TALO (SEC)	TEMP (°F)	TALO (SEC)	TEMP (°F)
1620.0	83.74	1622.8	100.91	1625.6	127.39	1628.4	187.50
1620.1	83.69	1622.9	103.31	1625.7	129.74	1628.5	189.96
1620.2	86.15	1623.0	103.37	1625.8	132.09	1628.6	189.96
1620.3	86.20	1623.1	103.37	1625.9	137.05	1628.7	192.31
1620.4	86.20	1623.2	103.32	1626.0	132.31	1628.8	194.72
1620.5	86.20	1623.3	105.72	1626.1	134.55	1628.9	197.13
1620.6	86.15	1623.4	105.78	1626.2	136.86	1629.0	199.58
1620.7	88.61	1623.5	105.73	1626.3	144.02	1629.1	199.59
1620.8	88.67	1623.6	108.13	1626.4	148.89	1629.2	201.94
1620.9	88.67	1623.7	108.18	1626.5	153.70	1629.3	204.40
1621.0	88.67	1623.8	108.13	1626.6	158.51	1629.4	204.35
1621.1	88.67	1623.9	110.53	1626.7	163.33	1629.5	209.10
1621.2	88.67	1624.0	110.59	1626.8	168.14	1629.6	211.62
1621.3	88.61	1624.1	110.59	1626.9	173.00	1629.7	211.62
1621.4	91.07	1624.2	110.54	1627.0	175.57	1629.8	213.97
1621.5	91.13	1624.3	112.94	1627.1	173.22	1629.9	216.33
1621.6	91.08	1624.4	112.95	1627.2	173.17	1630.0	220.99
1621.7	93.54	1624.5	115.35	1627.3	173.17	1630.1	230.50
1621.8	93.54	1624.6	115.35	1627.4	173.17	1630.2	240.18
1621.9	96.00	1624.7	117.76	1627.5	173.11	1630.3	247.20
1622.0	96.06	1624.8	117.76	1627.6	175.52	1630.4	266.13
1622.1	96.06	1624.9	120.16	1627.7	175.52	1630.5	287.78
1622.2	96.01	1625.0	120.22	1627.8	177.92	1630.6	307.29
1622.3	98.47	1625.1	120.17	1627.9	177.93	1630.7	324.57
1622.4	98.52	1625.2	122.52	1628.0	180.28	1630.8	339.35
1622.5	98.47	1625.3	124.98	1628.1	182.69	1630.9	354.08
1622.6	100.91	1625.4	124.98	1628.2	185.14	1631.0	368.85
1622.7	100.96	1625.5	127.38	1628.3	185.15	1631.1	381.18

Table AI (Continued)
Flight 2 Thermocouple Data
Thermocouple No. 151

TALO (SEC)	TEMP (°F)	TALO (SEC)	TEMP (°F)
1631.2	393.29	1634.0	1043.15
1631.3	412.86	1634.1	1080.26
1631.4	427.70	1634.2	1117.55
1631.5	442.42	1634.3	1157.40
1631.6	457.14	1634.4	1197.21
1631.7	471.82	1634.5	1241.65
1631.8	488.99	1634.6	1288.48
1631.9	503.61	1634.7	1338.32
1632.0	519.92	1634.8	1388.28
1632.1	553.25	1634.9	1442.90
1632.2	572.62	1635.0	1502.53
1632.3	594.04	1635.1	1561.13
1632.4	615.57		
1632.5	634.62		
1632.6	658.48		
1632.7	677.73		
1632.8	694.40		
1632.9	715.28		
1633.0	743.21		
1633.1	768.96		
1633.2	794.61		
1633.3	822.65		
1633.4	848.35		
1633.5	876.24		
1633.6	908.78		
1633.7	941.26		
1633.8	973.74		
1633.9	1006.13		

Table AI (Continued)

Flight 2 Thermocouple Data

Thermocouple No. 152, X = 169.62", ϕ_S = 315°

TALO (SEC)	TEMP (°F)	TALO (SEC)	TEMP (°F)	TALO (SEC)	TEMP (°F)	TALO (SEC)	TEMP (°F)
1608.0	32.00	1618.0	36.93	1620.8	49.18	1623.6	63.97
1609.0	32.00	1618.1	36.87	1620.9	49.25	1623.7	66.43
1610.0	32.00	1618.2	39.32	1621.0	49.25	1623.8	66.49
1611.0	32.00	1618.3	39.39	1621.1	49.25	1623.9	66.49
1612.0	32.00	1618.4	39.39	1621.2	49.25	1624.0	66.43
1613.0	32.00	1618.5	39.39	1621.3	49.25	1624.1	68.89
1614.0	32.00	1618.6	39.39	1621.4	49.19	1624.2	68.96
1615.0	32.00	1618.7	39.39	1621.5	51.64	1624.3	68.96
1616.0	32.00	1618.8	39.39	1621.6	51.71	1624.4	68.90
1616.1	31.94	1618.9	39.39	1621.7	51.65	1624.5	71.41
1616.2	34.40	1619.0	39.39	1621.8	54.11	1624.6	68.96
1616.3	34.46	1619.1	39.33	1621.9	54.11	1624.7	71.35
1616.4	34.46	1619.2	41.79	1622.0	56.57	1624.8	71.42
1616.5	34.46	1619.3	41.86	1622.1	56.64	1624.9	71.36
1616.6	34.46	1619.4	41.86	1622.2	56.64	1625.0	73.82
1616.7	34.46	1619.5	41.86	1622.3	56.58	1625.1	73.76
1616.8	34.46	1619.6	41.80	1622.4	59.03	1625.2	78.68
1616.9	34.46	1619.7	44.25	1622.5	59.10	1625.3	78.75
1617.0	34.46	1619.8	44.32	1622.6	59.10	1625.4	81.27
1617.1	34.46	1619.9	44.32	1622.7	59.04	1625.5	78.82
1617.2	34.46	1620.0	44.32	1622.8	61.50	1625.6	81.21
1617.3	34.46	1620.1	44.32	1622.9	61.57	1625.7	81.22
1617.4	34.40	1620.2	44.26	1623.0	61.57	1625.8	83.67
1617.5	36.86	1620.3	46.72	1623.1	61.57	1625.9	83.68
1617.6	36.93	1620.4	46.78	1623.2	61.57	1626.0	86.08
1617.7	36.93	1620.5	46.78	1623.3	61.51	1626.1	88.48
1617.8	36.93	1620.6	46.78	1623.4	63.96	1626.2	93.34
1617.9	36.93	1620.7	46.72	1623.5	64.03	1626.3	98.27